MICROSTRCTURAL EVOLUTION AND MECHANICAL PROPERTIES OF HIGH STRENGTH MAGNEISUM ALLOYS FABRICATED BY DEFORMATION PROCESSING

by

Bilal Mansoor

A dissertation submitted in partial fulfillment
of the requirements for the degree of
Doctor of Philosophy
(Materials Science and Engineering)
in The University of Michigan
2010

Doctoral Committee:

Professor Amit K. Ghosh, Co-Chair
Emeritus Professor William F. Hosford Jr., Co-Chair
Professor Jwo Pan
Professor Richard E. Robertson

To my parents Mansoor Ahmed and Shahnaz Mansoor,
my parents-in-law Mansoor Shafi and Nuzhat Mansoor,
my wife Maham Bilal,
and my son Armaghan Bilal.
with admiration, gratitude and love.

TABLE OF CONTENTS

LIST OF TABLES

LIST OF FIGURES

FIGURE

CHAPTER 1

MICROSTRUCTURAL EVOLUTION AND WARM FORMABILITY IN TWIN-ROLL CAST AZ31 MAGNESIUM PROCESSED BY BIAXIAL CORRUGATED PRESSING AND ROLLING

Abstract

Severe plastic deformation was imparted to twin-roll cast AZ31C Mg plate by Alternate Biaxial Reverse Corrugated (ABRC) [1] pressing and rolling. The microstructural evolution and superplastic forming capability of processed material is reported here. The initial bimodal grain structure of this alloy with 12.8 μm average grain size was progressively subdivided by corrugated pressing in the temperature range of 300^{o}C to 250^{o}C, followed by hot rolling at 350^{o}C to achieve a nearly uniform ultra-fine microstructure of 1.1 μm average size at a true strain of $\varepsilon = 6.6$. Uniaxial tensile tests revealed that at 350^{o}C for a strain rate of 2×10^{-4} s^{-1} processed material exhibits superior tensile elongation of 325% with a superplastic m-value equal to 0.55. In the selected temperature range the peak m-value increases with increasing deformation temperature and a sigmoidal relationship is observed between $\log \sigma$ and $\log \dot{\varepsilon}$. Superplastic forming capability of processed material was demonstrated at 300^{o}C for a strain rate of $\sim 2 \times 10^{-3}$ s^{-1}.

1.1 Introduction

Magnesium alloys are constantly gaining importance as lightweight structural materials for automotive applications [2, 3]. Sheet components of Mg alloys are especially attractive due to their low density, high specific stiffness and strength and also the recycling ability [4, 5]. Additionally magnesium exhibits heat conduction and electro-magnetic interference shielding, which makes it more attractive than polymeric materials to electronics industry for use in a variety of portable devices [6]. However, Mg is not amenable to satisfactory room temperature forming due to its hexagonal close-packed crystal structure and limited number of independent slip systems [7, 8]. Deep drawing at elevated temperature is currently used for fabricating sheet parts while a majority of Mg products are fabricated in smaller and thicker geometries by die casting process [2, 3, 12]. The lower formability of Mg alloys can be overcome by warm forming (stretch) processes. However, at elevated temperatures (> 300^{o}C) oxidation problems complicate manufacturing process [9-11]. Thus an important current objective is fabrication of Mg alloy sheets capable of rapid forming (> $10^{-3}s^{-1}$) at warm temperatures (200-300^{o}C).

Nanocrystalline and ultra-fine grain (UFG) microstructures (10-1000 nm) characterized by a large volume fraction of grain boundaries exhibit unique mechanical properties as compared to their coarse-grain counterparts [13-17]. Small quantities of such structures have been synthesized by techniques such as electrodeposition, vapor deposition, rapid solidification, powder metallurgy etc [18-23]. Thermomechanical metal working techniques involving severe plastic deformation hold greater promise in production of bulk materials. They include equal channel angular pressing [24], high pressure torsion [25], accumulative roll bonding [26], reciprocating extrusion [27],

alternate biaxial reverse corrugation process [1, 28, 29], and friction stirring [30]. The ABRC process is a modified form of a Multi-step Corrugating/coining and Flattening/straightening process developed by Ghosh and Huang in 1999 [31]. A lateral constraint was introduced in the original MCF process to enhance strain concentration in work-peace without crack formation. ABRC process was previously applied to hot rolled AZ31B Mg to produce ultra-fine grained sheet [1, 28]. In a related study on Mg alloys with porosity i.e. thixomolded alloys, it was shown that porosity reduction is critical prior to application of ABRC process [30]. Corrugated pressing and flattening may be employed to produce bulk quantities of ultra-fine grain Mg sheets suitable for warm forming (Figure.1) [32].

Superplasticity has been reported in several coarse-grain magnesium alloys at high temperatures and low strain rates in extruded or rolled condition [33-37]. Many recent investigations have shown that at low temperatures, high tensile ductility associated with superplasticity occurs in ultra-fine grained Mg processed by different methods such as AZ91, ZK60 and AZ31 Mg [38-39]. In the work reported here, the starting material of interest was twin-roll cast AZ31C Mg plate [40]. Twin-roll strip casting is thought to be a cost-effective process that integrates casting and hot rolling into a single step. It employs faster solidification rates (10^{-2} to 10^{-3} Ks^{-1}) than conventional casting that reduces segregation and refines grain size [41, 42]. Twin-roll cast Mg products (3-5 mm thick) are generally thicker than sheets produced by wrought processing from cast Mg alloys. Twin-roll casting typically produces an equiaxed microstructure in Mg alloys with reasonably good mechanical properties and deep drawability [40-44]. However in this study the twin-roll cast AZ31 Mg alloy was found

to possess bimodal microstructure. Hence, an objective was to process this alloy by severe plastic deformation to create uniform fine grain structure, while causing possible changes in the character of grain boundaries to improve its superplastic properties at low forming temperature. A brief comparison is made by comparing results of present study with work of Yang et al. [1, 28] on ABRC processing of wrought AZ31B Mg. The overall objective is to create an ultra-fine grain material from wrought or cast Mg plates to fully explore and establish the potential offered by ABRC deformation processing.

1.2 Experimental

1.2.1 Materials and processing

The AZ31C Mg material investigated in this work was received in the form of 3.3 mm thick twin-roll cast plate from Australian Commonwealth Scientific and Research Organization (CSIRO). The ASTM designation is AZ31C and the alloy nominal composition range is given in Table. 1.

Details of the ABRC processing and an estimation of imparted cumulative strains are described in Ref. [1, 28]. Here, a flat 89 mm x 89 mm metal work-piece with thickness 3.3 mm was machined from the as-received AZ31C plate. It corrugated and pressed isothermally, multiple times between asymmetrically corrugated dies with lateral constraint. The wavy work-piece was rotated through 90° and placed back within the constrained die walls and the next corrugation step was performed. A total of 3 ABRC deformation cycles were performed on the work-piece with 4 corrugation steps performed in each cycle at a straining speed of 0.12 mm/min. The deformation temperature through the multiple steps was progressively lowered from 300^{o}C to 260^{o}C during the ABRC process. The final flattening step was performed at 260^{o}C after the

completion of 3 cycles. Fig. 1(a) schematically explains the corrugation and flattening steps performed during ABRC process. There was no change in the thickness of work-piece after 3 cycles of ABRC at a mid-plane cumulative strain of nearly 5.0. Fig. 1(b) shows the shape of the work-piece after the first four steps of corrugation. At such high levels of plastic strain considerable grain refinement was achieved and a homogeneous ultra-fine structure evolved in the entire work-piece.

After completion of ABRC processing steps a small piece machined from the work-piece was pre-heated in furnace at 350^{o}C for 10 min and then rolled in a single pass of ~ 70% thickness reduction to achieve a final sheet thickness of 1.0 mm. In the work presented here, rolling was carried out at 25 rpm on a 5"x 8" Stanant rolling mill. The ABRC-processed and hot rolled AZ31C Mg will also be called as-processed condition in this text.

1.2.2 Microstructure characterization

The microstructural examination was done on the as-received, as-processed and elevated temperature tensile tested samples of as-processed AZ31C Mg. All the samples were sectioned along a plane containing the normal direction and the rolling direction. Metallographic specimens were cold mounted in self-curing resin, fine ground and mechanically polished. They were later etched with acetic-picral (4.2 g picric acid, 70 ml ethanol, 10 ml acetic acid and 10 ml distilled water) solution. Cross-sectional microstructures of the specimens were examined using optical and scanning electron microscopes. A XL30-FEG SEM was employed to observe very fine microstructure at higher magnifications. The operating voltage was 20-30 kV. The non-uniform grain

structure was characterized by a detailed grain size distribution analysis using an image processing and analysis software ImageJ [1, 28].

1.2.3 Mechanical tests

The low temperature superplastic behavior of the processed material was evaluated by tension tests performed at elevated temperatures. Tensile samples with 6.35 mm long, 3.18 mm wide and 1.0 mm thick gauge sections were cut from the ABRC-processed and hot rolled AZ31 Mg sheet. The specimens were tested at temperatures of 250^{o}C, 300^{o}C, and 350^{o}C in the air at selected constant strain rates of 2 x 10^{-3} s^{-1} and 2 x $10^{-4}s^{-1}$. A constant strain rate crosshead control schedule [45] was used on a graphic interface board (GPIB) enabled computer controlled Instron 4505 machine. This schedule corrects for the effect of material flow from the specimen grip region during constant strain rate test. A clamshell furnace with three independent heating zones was utilized to reach the set temperature in 15-20 minutes before start of the test and than maintain specimen temperature within $\pm 2^{o}$C of the set temperature during the constant strain rate test. Tensile elongations were determined by adding the measured sample lengths between the edge of the sample shoulder and failed edge from two broken parts of sample, the measurements are taken along samples central axis. The true fracture strain was calculated by measuring the initial area of the sample gauge and the area of the fracture region. These tests were performed at constant temperatures at predetermined strain rates and provided the most reliable measure of warm formability. The variations of strain rate sensitivity, $m = (\partial \log \sigma / \partial \log \dot{\varepsilon})$, with strain rate were determined by decremental step-strain rate tensile tests [46]. Details of the decremental step strain-rate schedule and procedure for calculating m-value is described in an earlier report [46].

Using this method, step strain-rate tests were conducted on as-processed AZ31 Mg range of 250 -350^{o}C.

Limited gas pressure forming tests were performed on as processed AZ31 Mg sheet to evaluate biaxial formability. The biaxial forming samples were electro-etched with 0.25 mm diameter circular grids. A 1.0 mm thick sheet blank clamped in a heated 50.4 mm dia circular die was pre-heated at 300^{o}C for 10 minutes. Hemispherical dome was formed by applying gas pressure from one side of the clamped sheet in the die. To evaluate the strain distributions in formed parts, the post-test dome heights and grid size around necked regions and crack were measured by calipers and digital camera photographs using a computer program (ImageJ). These tests only provide a quick evaluation of the dome height and warm forming limit and they do not represent conditions comparable to the tensile tests. The room temperature mechanical properties data are presented in Appendix. A.

1.3 Results

1.3.1 Microstructural evolution during processing

The microstructure of twin-roll cast AZ31C Mg plate is shown Fig. 2. Fig. 2(a) shows the microstructure in near surface region with 100 μm -200 μm size coarse grains that extend into the bulk to a depth of approximately 0.5 mm. On the other hand, Fig. 2(b) shows inhomogeneously distributed bands of fine and coarse grains in the center region of plate section. There was considerable variation in microstructure from one region to another, but bulk of the material had a relatively finer microstructure similar to center region. The inhomogeneity in grain structure was characterized by a detailed grain size distribution analysis as in Ref. [1, 28]. The area of a photograph of as-received AZ31

Mg as shown in Fig 3(a) is divided into regions of coarse grain (Fig. 3(b)) and fine grains (Fig. 4(c)). Fig. 4(c) and (d) show the individual grain size distributions of the coarse and fine grain regions fitted with Gaussian distribution function. The bimodal grain-size distribution is the combination of these two distributions as shown in Fig. 4 (f). The microstructure of twin-roll cast AZ31 has an area fraction 56% for finer grains with a mean grain size of 9.2 μm, mean grain size of coarse grains is 37.5 μm. The average grain size is 12.8 μm.

Microstructure after first ABRC cycle in Fig. 4 shows the progress of grain refinement. In Fig. 4 (a) extensive twinning is seen in coarse grains (indicated by arrows) along with the formation of new grains and sub-grains at twin boundaries. These deformation twins intersect other twins and grain boundaries. Smaller twins are lined up in parallel groups as indicated by highlighter area. Fig. 4 (b) shows that in some regions new fine grains completely replace the original coarse structure; serrated grains boundaries and "necklace" grain structure indicate that new grains start from the grain boundaries of original microstructure. The original grain structure is gradually refined with increasing strain. At deformation temperature of 300^{o}C and true strain of ε =1.87, twinning is observed mainly in coarse grains.

Fig. 5 illustrates the microstructure at strain of 5.0 after the 3 ABRC cycles and final flattening step at 250^{o}C. The microstructure has evolved into a nearly uniform fine-grain structure as compared to the initial bimodal grain structure of the starting material (Fig. 5 (a)). Fig. 5(b) shows that the fine grains are equiaxed and show an increase in area fraction. However no twinning is witnessed in grains smaller than 4 μm. Although significant grain refinement is witnessed at this processing stage but it can be noticed that

the structure still has some coarse grains reminiscent of the initial bimodal that inhomogeneously distributed though out the sample. The microstructure after ABRC processing has mean grain size of 2.5 μm for fine grain with an increase in area fraction to 74% while mean size for coarse grains is 10 μm.

Scanning electron micrographs in Fig. 6 shows the microstructure of ABRC processed AZ31 after hot rolling at 350^{o}C to a true strain of ε =1.62. The grain structure at this stage is homogeneous and the starting bimodal structure has been refined in to very fine and uniform structure. Fig. 6(a) shows the microstructure of ABRC processed, flattened and hot rolled AZ31C; coarse grains in the ABRC structure are sheared to create elongated grains in the rolling direction as shown by the arrows. Fig. 6(b) shows a fine grain homogeneous structure; along with some 3-5 μm coarse grains many sub-micrometer-size grains are visible. The grain size distribution analysis shows a narrower spread and a higher frequency of fine grains. Overall average grain size is 1.1 μm and the fine grain area fraction has now reached 96.4 %.

1.3.2 Elevated temperature tensile tests

Fig. 7 shows typical (σ-ε) flow curves of as-processed Mg alloy subjected to strain rate of 2 x 10^{-3} s^{-1} and 2 x 10^{-4} s^{-1} at selected temperatures of 250^{o}C, 300^{o}C and 350^{o}C. The true stress is calculated under an assumption that specimens undergo uniform deformation. This assumption does not hold after the maximum stress level, also the true stress values after stress peak are very low. Increasing temperature or decreasing strain rate leads to a lower peak stress, a higher tensile elongation and a higher fracture strain (Table. 2). The as-processed AZ31C shows a maximum tensile elongation of 325% at 350^{o}C and a strain rate of 2 x 10^{-4} s^{-1}. Extensive initial strain hardening takes place for

strain rate of 2 x 10^{-3} s^{-1} while a steady strain hardening is seen for strain rate of 2 x 10^{-4} s^{-1} under all test temperatures. At 250^{o}C under both strain rate conditions; after reaching a maximum, strain softening occurs and flow stress continuously decreases until fracture. This is unlike other test conditions where after reaching maximum flow stress the onset of fracture is quite rapid. Fig. 8 shows photos of the as-processed AZ31C tensile specimens before and after the test under the slow strain rate condition. The specimens show some diffuse necking at deformation temperatures higher than 250^{o}C.

1.3.3 Strain rate sensitivity:

Fig. 9 (a) shows the flow stress as a function of strain rate for as-processed AZ31 Mg at 250 ^{o}C, 300 ^{o}C and 350^{o}C deformation temperatures. The processed alloy exhibits a sigmoidal relationship between flow stress and strain rate at all temperatures. In Fig. 9 (b) the value of strain rate sensitivity, m, is shown as a function of strain rate. It rises to 0.55 for ~ 10^{-4} s^{-1} strain rate at 350^{o}C. At 300^{o}C the peak m-value drops to about 0.42 and the strain rate corresponding to peak m-value here is displaced to lower strain rate of ~5 x 10^{-5} s^{-1}. At even lower temperature of 250^{o}C m-value of 0.39 was recorded at ~ 5 x 10^{-4} s^{-1}. At lower temperature of 250^{o}C, m drops to 0.39 at 5 x 10^{-4} s^{-1}strain rate. The value of activation energy (Q) is obtained from the slope of the log plot of strain rate vs. (1/T). In Fig 9 (c) such a log plot for constant stress of 40 MPa is shown. The slope of this plot (= - Q / 2.303R), which corresponds to a value of Q ~ 82.6 kJ/mol.

1.3.4 Microstructural evolution during elevated temperature tensile test

The microstructure of the as-processed AZ31C Mg shows significant changes during warm temperature deformation. The microstructural evolution was examined under both static and dynamic conditions in the grip and gauge sections. Fig. 10 shows

microstructural evolution for sample tensioned at 350^{o}C and 2 x 10^{-4}s^{-1}. Fig. 10(a) shows microstructure for as-processed AZ31 in the un-deformed region. The grain structure in the grip region is much more refined than the gauge region. Changes are seen in the average grain size and area fraction of the fine grains related to straining. During static heating prior to tension test in order to achieve homogenization in temperature, a nearly uniform grain structure of 2.75 μm evolves in the grip region. In the gauge region, the grain structure undergoes coarsening under the imposed strain. Fig. 10(b) shows the microstructure of average grain size 7.1 μm at strain $\varepsilon = 0.5$, significant grain growth is evident at this point in the gauge region. At $\varepsilon = 1.0$, the area fraction of fine grains has increased and the some grain refinement is seen at this increased strain, the average grain size at this stage is 5 μm (Fig. 10(c)). No significant cavitation is seen, and examination reveals that AZ31C shows little < 5% area fraction of cavities that are located near coarse grain boundaries and triple points at $\varepsilon = 1.0$.

Variations in average grain size with testing time and strain at 350^{o}C at strain rate of 2 x 10^{-4} s^{-1} are shown in Fig. 10 (d) and (e) respectively. The data for static annealing are also included for comparison. In Fig. 10(d) after initial grain growth under dynamic conditions, some grain refinement is witnessed at higher strain with the formation of new grains resulting from dynamic recrystallization. In Fig.10 (e), the grain growth with test time is shown; Static annealing data has also been included for comparison.

1.3.5 Superplastic forming

Fig. 11 shows the hemispherical dome of as-processed AZ31C Mg obtained under isothermal forming condition at 300^{o}C. The as-processed AZ31C 1.0 mm thick sheet demanded higher pressure because it formed to a deeper depth. A dome height of 25 mm

was achieved after forming for 3 mins. The average value of biaxial stress was calculated to be 50 MPa by using the membrane equation. A nominal pole strain rate of 2×10^{-3} s^{-1} was obtained by dividing the thickness strain at pole by the total time of test. It is shown that AZ31C alloy showed higher formability during the biaxial stretching with no cracks near the clamping radius. The major and minor strains measured from circle grid analysis and data from tensile tests are plotted in Fig. 11 (b) to give an approximate forming limit at 300^{o}C and strain rate of ~ 2×10^{-3} s^{-1}. Limit strain of 0.62 was measured in both biaxial directions near dome pole (near fracture, as shown in the 11(a).

1.4 Discussion

1.4.1 Microstructural evolution

(a) ABRC Processing and hot rolling

The mechanisms of grain refinement and the extent of microstructural homogeneity in ABRC processed Mg were discussed by Yang in Ref. [1, 20]. The mechanisms involved in evolution of sub-micron size grains by ABRC processing may be divided in three stages with respect to the applied cumulative plastic strain. At low strains ($\varepsilon < 2$), incompatibility stresses develop near grain boundaries due to lack of independent slips systems in the neighboring grains. These incompatibility stresses between adjoining grains activate the non-basal slips systems at temperatures above 200^{o}C; consequently sub-grains form near grain boundaries [47]. The misorientation of these newly formed sub-grains increases as they absorb the non-basal dislocations, which eventually results in boundary migrations and coalescence to create new grains, as shown in Fig. 3 [48]. Twinning plays a significant role in sub-dividing coarse grains that largely remain un-deformed during non-basal cross-slip driven processes. Lattice reorientation

during twinning may promote activation of new slip systems. Dislocations interacting inside twins and near twin boundaries may contribute to the overall grain refinement process [49]. Sub-structures may recover by dislocation-dislocation interaction within twinned areas. Formation of grains and sub-grains is seen near previously twinned recrystallized boundaries as shown in Fig. 3, which may be explained by dislocation-twin boundary interactions. Twinning and non-basal slip processes continuously result in grain refinement with twinning driven process active in coarse grains while compatibility stress driven process active near fine grain boundaries and twinned boundaries. At a cumulative plastic strain of 2, fine grain size of ~ 4 μm size evolved in the material [1, 28].

At medium levels of strain (ε = 2 - 4), twinning deformation subsides due to increase in the required twinning stress. The increased grain-boundary area fraction means the refinement process is mainly driven by the strain concentrations near grain boundaries (cross slip of non-basal dislocations). At this stage it was found beneficial to decrease deformation temperature, as was done in Ref. [1, 28]. At true strain of ε = 5, the ABRC processed structure is equiaxed with an over all average grain size of 2.5 μm (A_f = 74%). This structure is significantly coarser that what Yang et al. found in his work on AZ31B Mg (~1.4 μm average grain size, A_f = 97.2% with distribution of sharp high angle and diffuse sub-grains / grain boundaries). This may be explained by the fact that in present work the deformation temperature at this stage of processing is 250^{o}C which is significantly higher as compared to Yang's work (170^{o}C) on AZ31B Mg. Also the bimodal structure and chemistry of twin-roll cast AZ31C are not similar to wrought AZ31 Mg plate microstructure. Despite this effect, it is remarkable that such highly bimodal initial microstructure was considerably refined.

Strain imparted by hot rolling ($\varepsilon = 1.62$) results in dynamic recovery and some dynamic recrystallization. The previously twinned coarse grains present in ABRC structure are sheared to create pan-cake shaped grains elongated in the rolling direction. Although some grain growth may have taken place during pre-heating at high temperature before rolling but the final structure is equiaxed and uniform with ~1.1μm ultra-fine grain size with 96% area fraction of the finer grains.

(b) Elevated temperature tensile test

Microstructural evolution during uniaxial tension testing indicated extensive grain growth at early stage of deformation. This was followed by twinning in coarse grains at medium strains. This indicated that even in UFG Mg and at high deformation temperature, twinning is needed to accommodate plastic strain. At higher strains, ($\varepsilon > 1.0$) dynamic recrystallization caused some grain refinement and the area fraction of fine grains increased to 67%. A comparison of grain size evolution during dynamic and static conditions revealed that grain growth occurs more rapidly under dynamic conditions. Initially, grain size is very small but with grain growth, stress required to initiate twinning is decreased which results in formation of twins. In final stages of deformation grain refinement due to dynamic recrystallization is followed by cavity nucleation and coalescence that results in fracture.

1.4.2 Formability enhancement

The three well know, characteristic regions of superplasticity were identified by the sigmoidal relationship between flow stress and strain rate, as shown in Fig. 9(a). The low strain-rate region is dominated by diffusional processes primarily located at the grain boundaries, while the high strain rate region III is dominated by thermally assisted glide-

climb processes in the bulk of the material. In the medium strain rate range (region II), superior superplastic response is seen due to beneficial contributions from both processes. The peak m-value for both deformation temperatures was observed in this region, as shown in Fig. 9 (b). The variation of elongation to failure and strain rate is shown in Fig. 12 (b). At 350^{o}C for a 2 x 10^{-4} s^{-1} strain rate, the as-processed AZ31C Mg exhibits highest superplastic elongation to failure of 325%. It was also observed that strain hardening increases with faster strain rate and lower test temperature. It should be noted that m-value here is 0.55 ; this is consistent with the deformation mode dominated by grain boundary sliding [50]. It should also be noted that a drop in peak m-value to 0.5 and a slight shift to lower strain rate of 5 x 10^{-5} s^{-1} was seen in Fig. 9(b). Samples pulled at low temperature of 250 ^{o}C necked down to a point while diffuse necking was observed for higher test temperatures. Grain growth and possibly strain hardening effects the superplastic ability of UFG Mg at 350^{o}C. There processes interfere with strain localization and do allow the specimen to neck down to a point or a chisel edge at this higher test temperature (specimens shown in Fig. 8). The rapid drop in m-value at faster strain rates may also be related to grain growth and strain hardening. These two processes lead to dislocation build up in the samples which indicates that dislocation creep is dominant at higher strain rates [51]. The strain rate versus absolute temperature plot gives the value of activation energy which is substantially lower than lattice self diffusion of pure Mg (135 kJ / mol) [52].

The plot shown in Fig. 12(a) shows the variation of elongation to failure with test temperature. The data from Yang et al. have been included for comparison. It is shown that UFG Mg from both studies show similar elongations at a strain rate of 2 x 10^{-4} s^{-1}. In

case of AZ31B, the highest tensile elongation of 312% was achieved at 250^{o}C for a strain rate of 5 x 10^{-4} s^{-1}. In case of AZ31C a higher tensile elongation of 325% was achieved for a much slower strain rate of 2 x 10^{-4} s^{-1} but at higher temperature of 350^{o}C. Warm formability has a strong dependence on the grain size of this alloy, and UFG size was found to improve it. This preliminary evidence suggests that superplastic behavior can be imparted in twin-roll cast AZ31C Mg by severe plastic deformation. In addition to grain size, strain rate also influences warm forming of UFG Mg. Grain boundary sliding and grain size effect complement each other resulting in high strain rate sensitivity of ~ 0.5. This study also reveals that the initial grain size of the twin-roll cast alloy is rather less important as similar results were reported by Yang et al. for his work on wrought AZ31 Mg.

1.4.3 Superplastic forming time analysis

A plot between forming time and applied strain-rates is presented in Fig. 13. It was generated by combining uniaxial tensile test data and biaxial stretching data for 300^{o}C with appropriate corrections. Two cases are considered for a part of: (i) benign complexity (ε = 0.5; engineering strain = 67%) and (ii) general complexity (ε = 1.0; engineering strain = 172%). This plot is expected to be valid for 300^{o}C and it demonstrates that UFG microstructure can significantly reduce part forming time. A target part requiring ~ 67% strain maybe formed at fast strain rate from UFG material in ~2.5 mins. If formed at slow strain rate, the same part may take up to 40 mins. In the second case, a part with more complex or intricate geometry requiring about 172% forming strain maybe formed at fast strain-rate from UFG Mg in 10 mins. The same part will require about 80 mins at slow forming rate. A coarse-grain material may reach

desired forming strain of 172% when formed at > 350^{o}C and only under slower strain rate conditions. Therefore reduced forming time and low forming temperature for UFG Mg would reduce costs of thermal energy required to heat forming dies and part cleaning required for removal of oxidized surface layers. Thus ABRC processed UFG alloys are likely to provide considerable manufacturing cost advantage by providing fast superplastic forming capability at warm temperatures.

1.5 Conclusions

(1) Mutli-step corrugated die pressing followed by flat die pressing and hot rolling was used to prepare fine grain Mg alloy sheet (avg. grain size of ~1 μm) starting twin-roll cast AZ31C Mg alloy with bimodal grain structure of large average grain size. These results were in agreement with hot rolled AZ31B Mg ABRC processed by Yang [1, 28]. Ultra-fine grain size of 1 μm was produced in AZ31C Mg alloy, despite high finish rolling temperature.

(2) Twinning was found to occur during early stages of deformation processing of AZ31C Mg and contributes grain subdivision, while slip, dynamic recovery and possibly dynamic recrystallization during hot rolling deformation produced a uniform fine-grain structure.

(3) In uniaxial tension test ultra-fine grained alloy exhibited highest tensile elongation of 325% at strain rate of 2 x 10^{-4} s^{-1}. Microstructural evolution during uniaxial tension test indicated extensive grain growth followed by some twinning at early stage of

deformation. At higher strains of > 1.0 dynamic recrystallization resulted in some grain refinement.

(4) Strain-rate sensitivity (m-value) increased with increasing deformation temperatures. The peak m-value of 0.55 was obtained at 350^{o}C for strain rate of 2 x 10^{-4} s^{-1} for UFG AZ31C alloy suggesting that deformation mode was dominated by grain boundary sliding. The measured activation energy was much lower than lattice self diffusion of pure Mg and may indicate the viscous nature of the alloy due to increased grain boundary area fraction.

(5) Superplastic dome forming test done by applying gas pressure indicated that large dome height is possible for UFG AZ31C Mg; similar values were previously observed for AZ31B alloy studied by Yang and Ghosh. This proved that whether the starting alloy is a wrought product or a twin-roll cast product, superplastic forming response is mainly dependent on ultra-fine grain size and not the initial condition.

(6) An approximate analysis based on available data suggests that ABRC process can produce UFG AZ31C alloy capable of considerably reducing manufacturing cost for aero- and auto-parts. This benefit is expected due to faster forming rates at low forming temperatures.

Table 1.1 Nominal composition range of TRC AZ31 Mg (in wt. %)

Composition of CSIRO TRC AZ31C Alloy (in wt. %)						
Al	Mn	Zn	Si	Cu	Ni	Mg
2.89-2.92 %	0.29-0.30	0.91-0.92	0.04 max	<0.01	0.015-0.017	Bal.

Table 1.2 Tensile elongation and fracture strain of as-processed fine grain AZ31C Mg at warm temperatures for selected strain rates.

Test Condition		**Tensile Elongation, %**	**Fracture Strain, ε_f**
Temperature, ^oC	**Strain Rate, s^{-1}**		
250	2×10^{-3}	60	0.44
	2×10^{-4}	160	1.3
300	2×10^{-3}	110	0.75
	2×10^{-4}	230	1.4
350	2×10^{-3}	130	0.9
	2×10^{-4}	325	1.7
25*	5.5×10^{-4}	18.3	0.18

* Room temperature data included for comparison, RT test was a constant CHS test with initial strain rate of 5.5×10^{-4}.

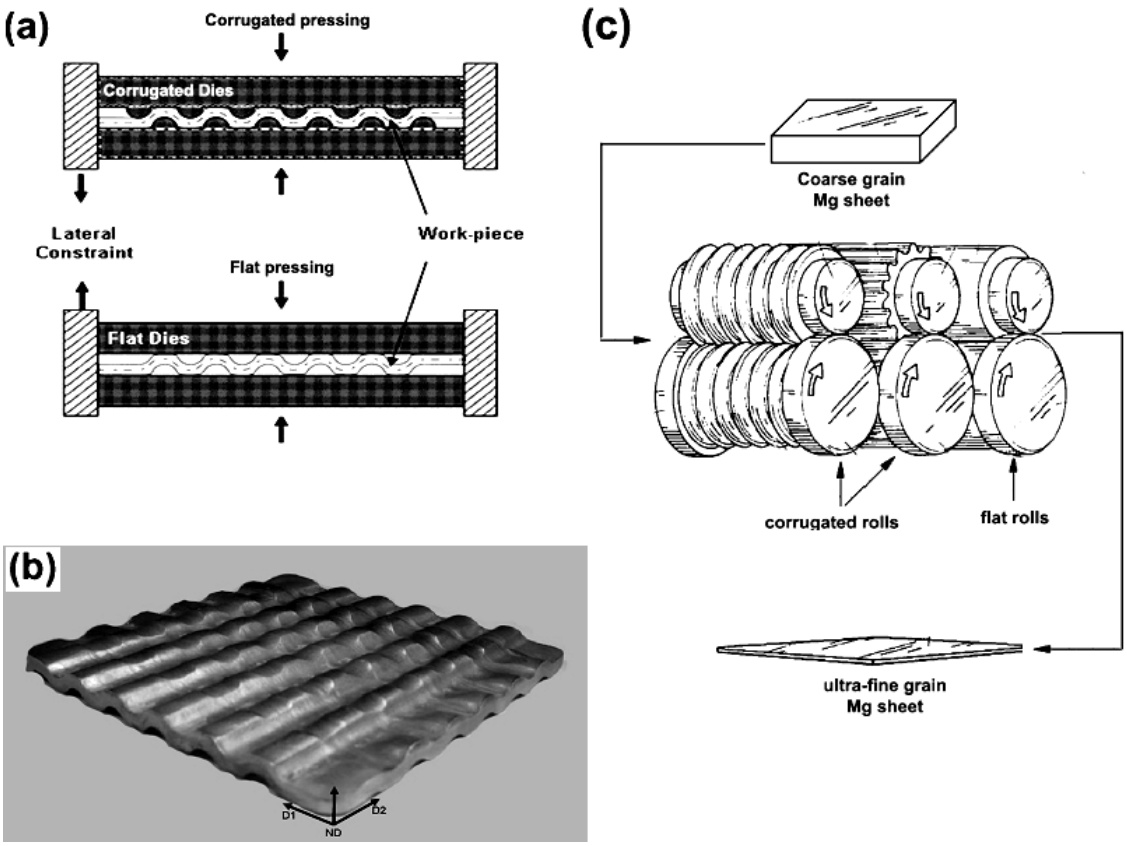

Figure 1.1 The Alternate Biaxial Reverse Corrugated (ABRC) pressing, in which a metal work-piece is pressed between asymmetrically corrugated dies, with successive rotation by 90° [1]. (a) Shows the work-piece under lateral constraint during corrugated and flat pressing steps. (b) Shows a biaxially corrugated work-piece after a cycle of ABRC. (c) Illustration of corrugated and flat rolling strategy for production of large quantities of ultra-fine grain Mg sheets [32].

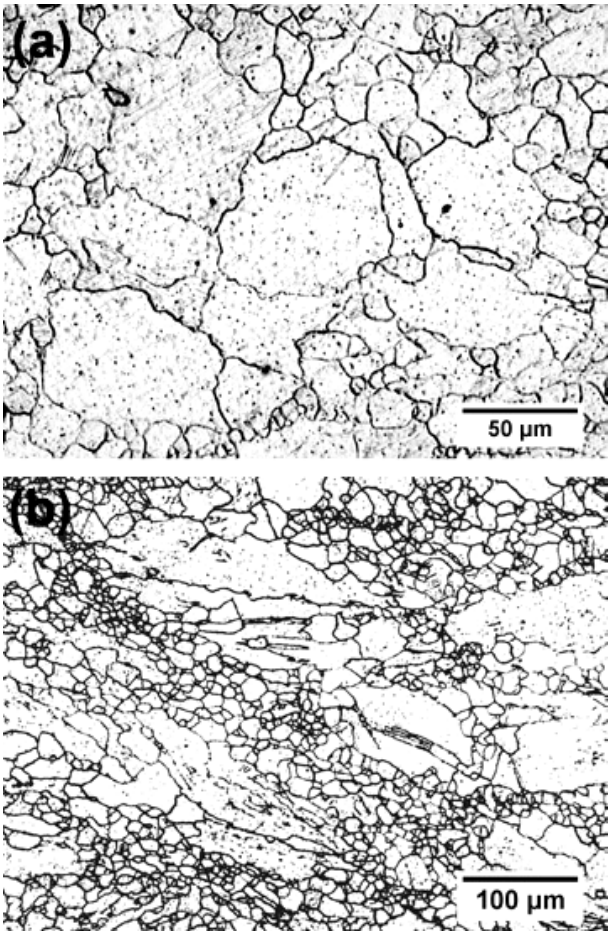

Figure 1.2 Microstructure of as-received twin roll casted AZ31C magnesium: (a) near surface region shows coarse equiaxed structure, (b) center region surface shows the cast sheet has bimodal grain structure with dendritic coarse grains surrounded by inhomogeneously distributed finer grains.

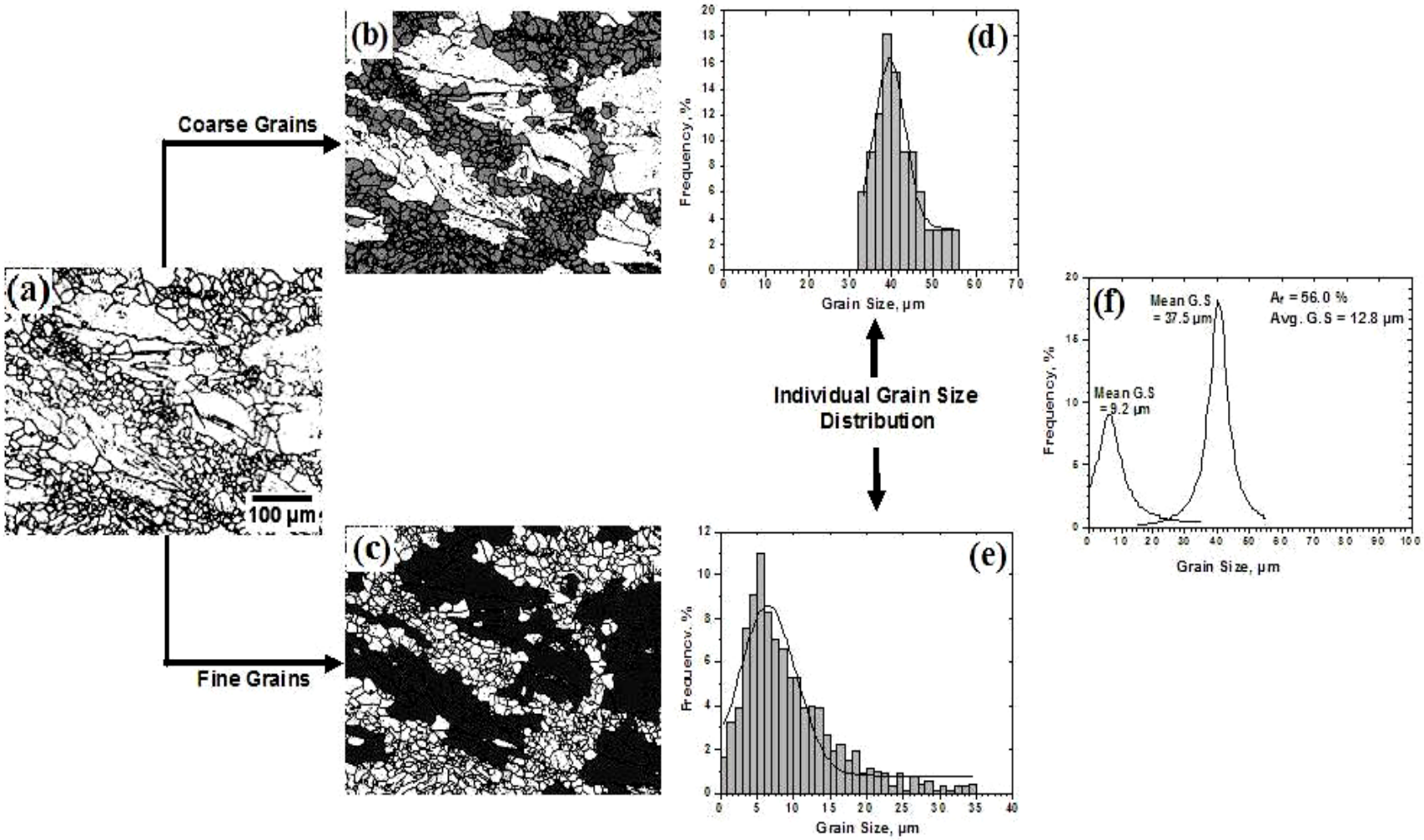

Figure 1.3 The microstructure of as-received AZ31C Mg and the analysis of bimodal grain size distribution.

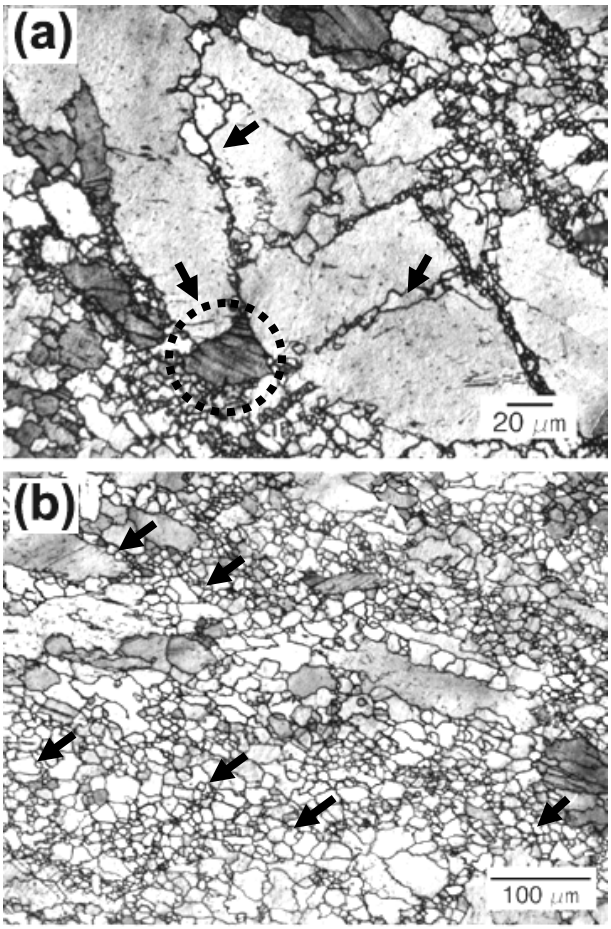

Figure 1.4 Progress of grain refinement during ABRC processing twin roll cast AZ31 Mg alloy after 1st processing cycle at 300^{o}C and strain ε =1.87. (a) Shows extensive twinning in the coarse grains and formation of new grains and sub grains near twin boundaries (arrows). In (b) arrows indicate formation of fine new grains from grain boundaries.

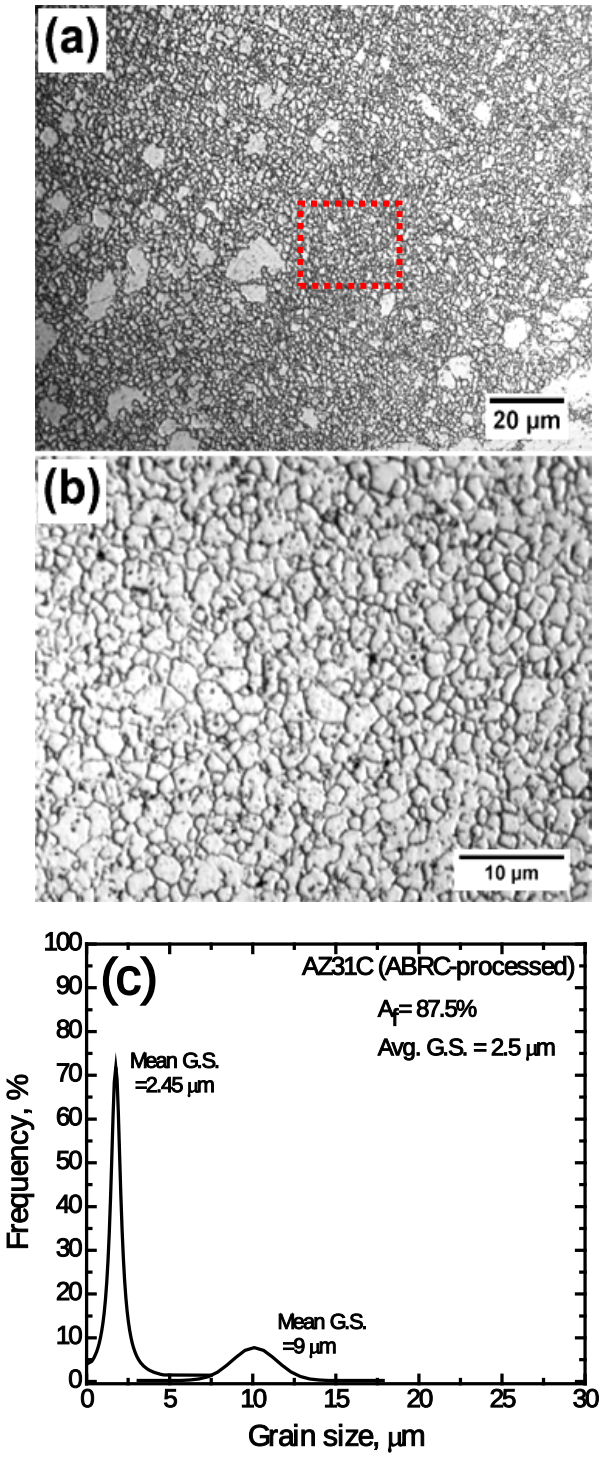

Figure 1.5 (a) & (b) show microstructure of twin roll cast AZ31 after 3 ABRC cycles and final flattening step at 250^{o}C and strain ε =5.0. In (a) mean grain size for coarse grains is 9 µm. (b) Magnified view of selected region shows equiaxed microstructure of fine grains with mean grain size of 2.5 µm and an increased area fraction of 87.5 % occupied by them in the bulk of material as compared to the starting material.

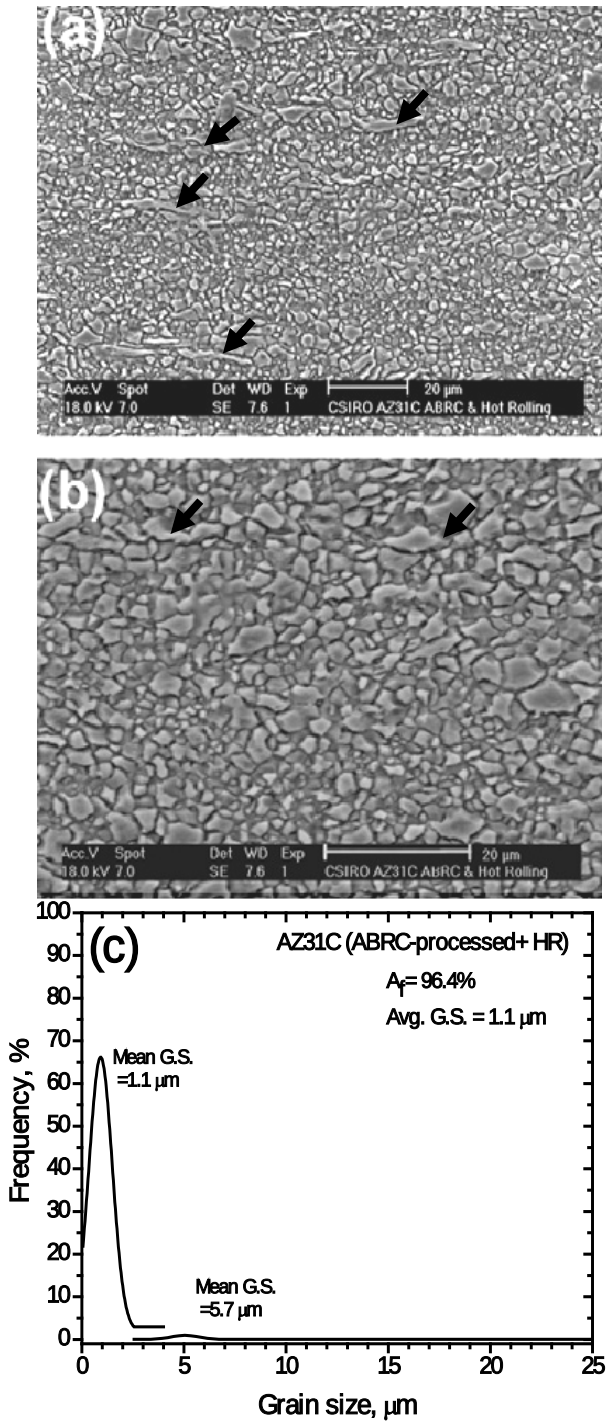

Figure 1.6 SEM image shows microstructure of ABRC-processed AZ31 Mg alloy after hot rolling at 350^{o}C and strain ε =1.62. (a) Shows significant grain refinement in both the fine and coarse grains as compared to the previous condition in Fig 1.5, arrows indicate shearing in some coarse grains, they elongate and align in the rolling direction, (b) shows that the ABRC refined grains have been further refined significantly along the rolling direction, very little twinning is seen and over all grain structure is homogeneous. (c) Analysis of coarse and fine grain size distributions. The average grain size of as-processed Mg is 1.1 µm.

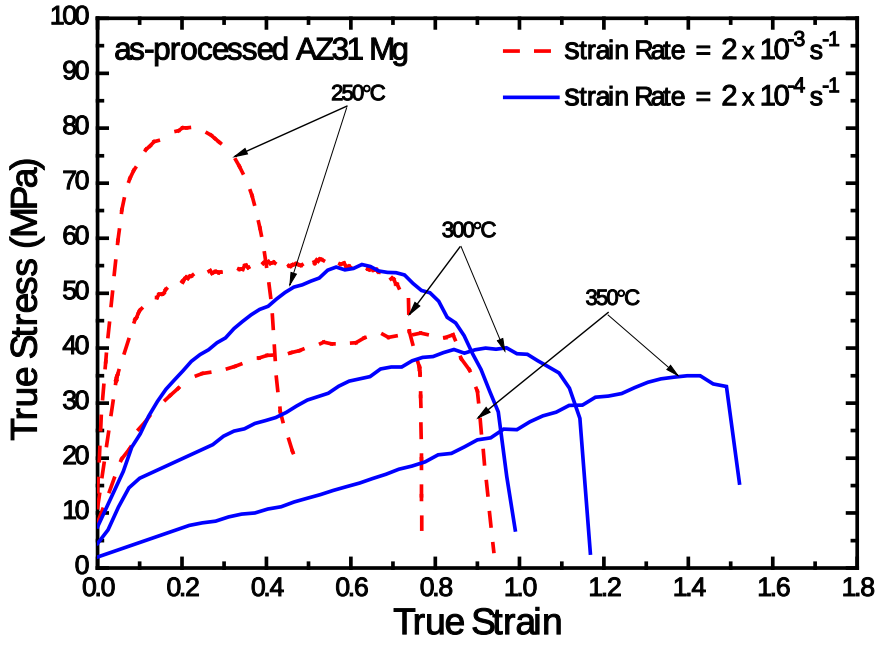

Figure 1.7 Stress versus strain relationship of as-processed AZ31C Mg at elevated temperatures 250°C to 350°C under constant strain rates of 2 x $10^{-3}s^{-1}$ and 2 x $10^{-4}s^{-1}$.

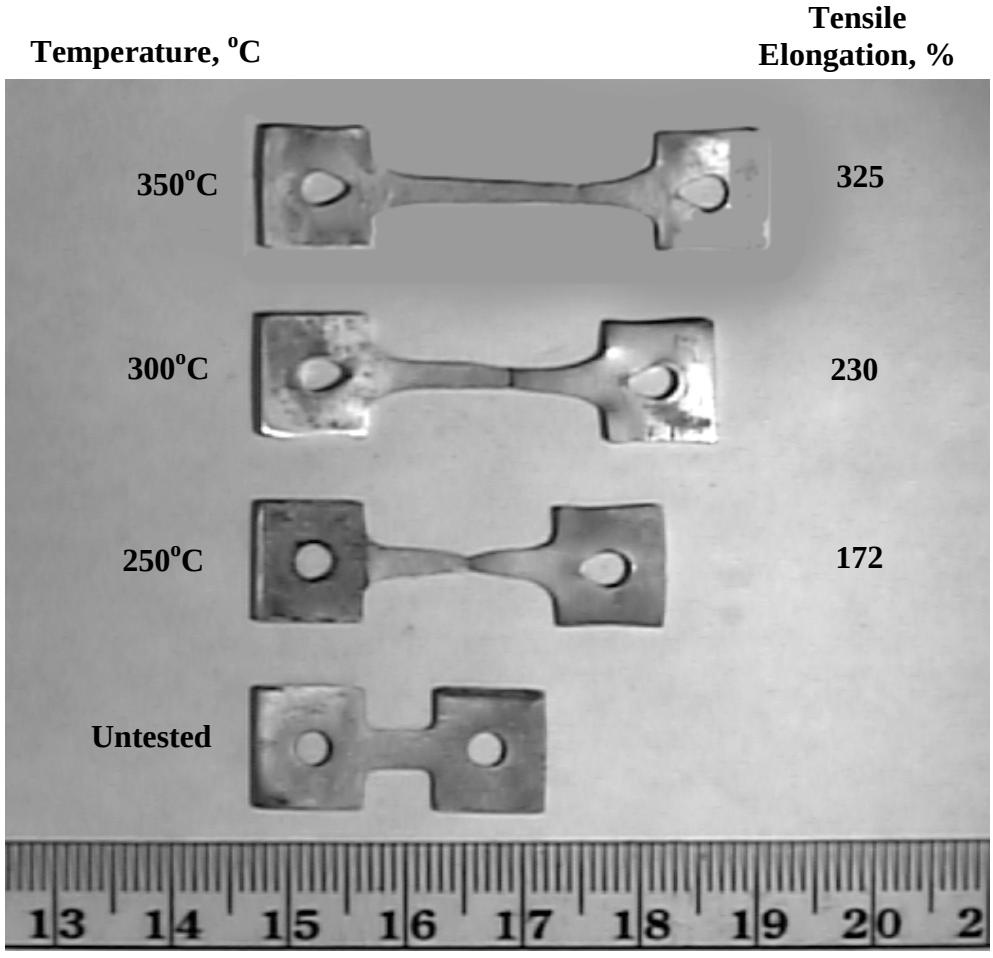

Figure 1.8 Photos of the as-processed Mg elevated temperature tensile specimens before and after the deformation at various temperatures and strain rate of 2 x 10^{-4} s^{-1}.

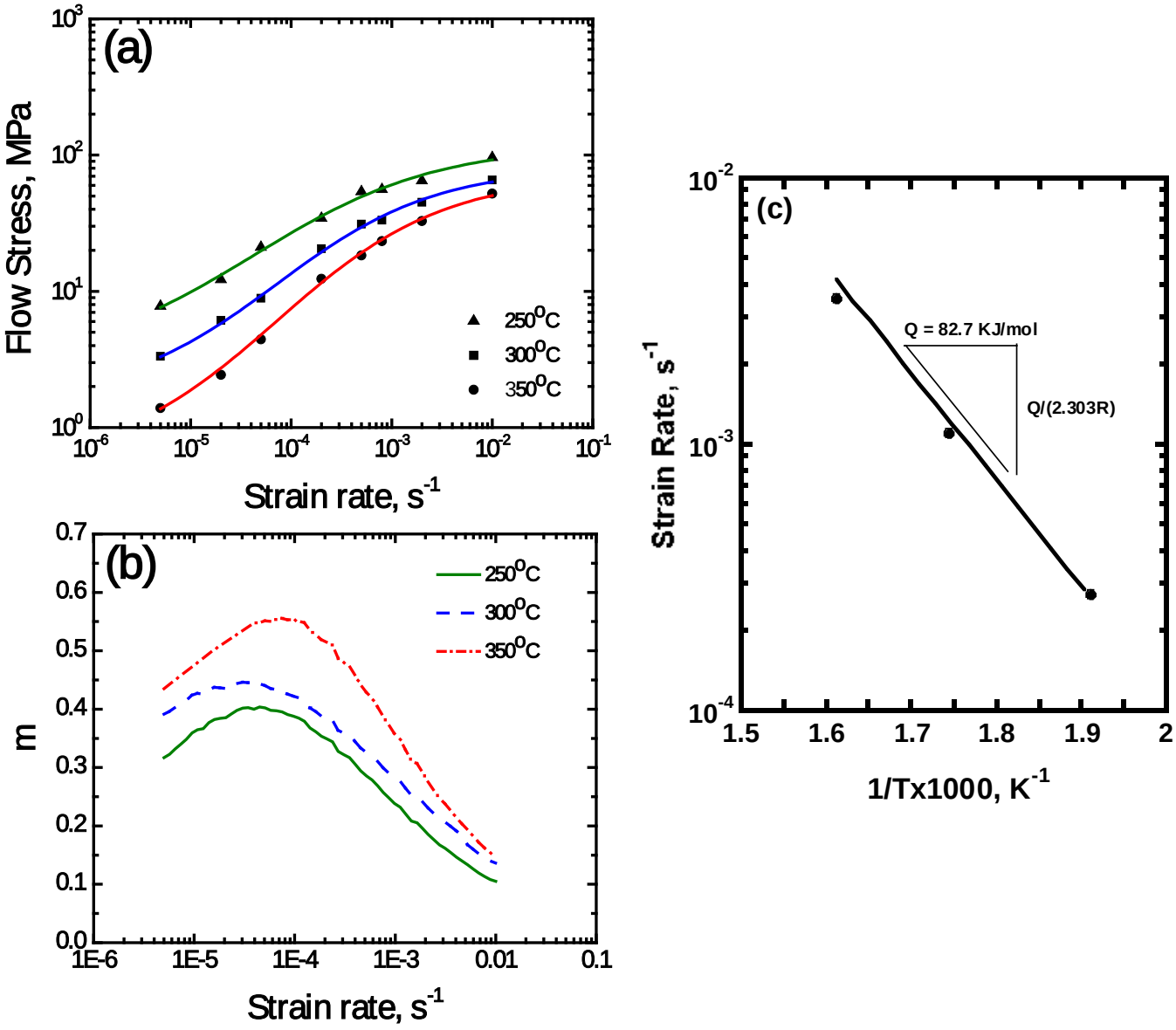

Figure 1.9 (a) Stress versus strain rate relationship of as-processed Mg alloy at selected test temperatures, the value of slope is strain rate sensitivity; m-value (b) Shows the variation of strain rate sensitivity with strain rate at selected test temperatures. (c) Activation energy obtained from log strain rate to log 1/ T plot at constant stress.

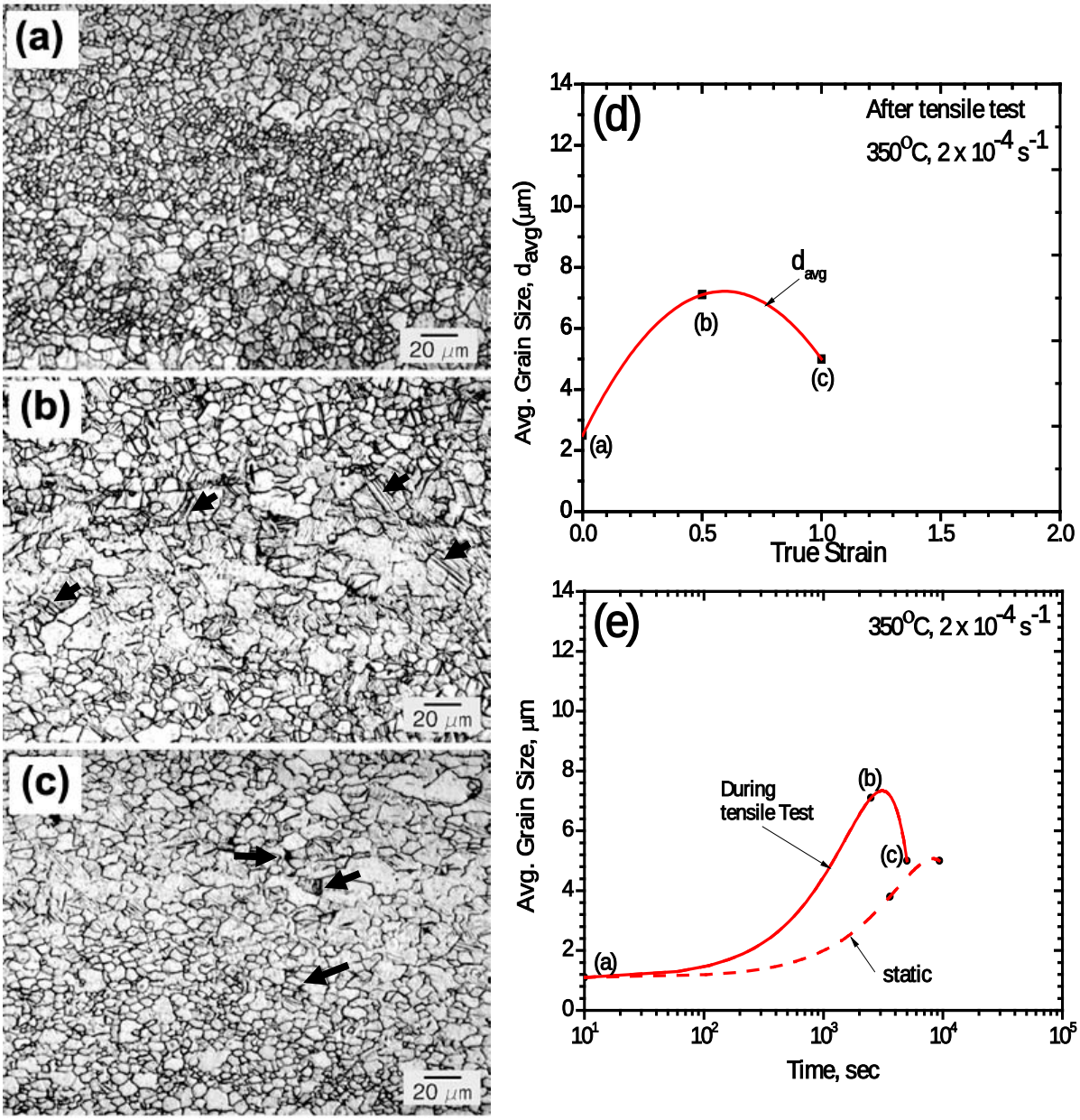

Figure 1.10 Microstructure evolution during elevated temperature tensile test done at 350°C and at a strain rate of 2 x $10^{-4}s^{-1}$. (a) Shows microstructure for as-processed AZ31C in the unreformed region with average grain size 2.75 μm. At ε = 0.5 in (b) some grain growth is seen and average grain size here is 7.1 μm. Also twinning is seen in some coarse grains indicated by arrows. In (c) at ε =1.0, some grain refinement is seen (arrows) and average grain size is 4.5 μm, some cavitation is also seen at coarse grain boundaries (indicated by arrows). Variation of average grain size of as-processed AZ31 Mg after elevated temperature tensile test done at 350°C and a strain rate of 2 x $10^{-4}s^{-1}$ with (a) strain in the sample and the change in area fraction of fine grains. (b) Shows the microstructure with time during elevated temperature test. Data for static annealing are also included.

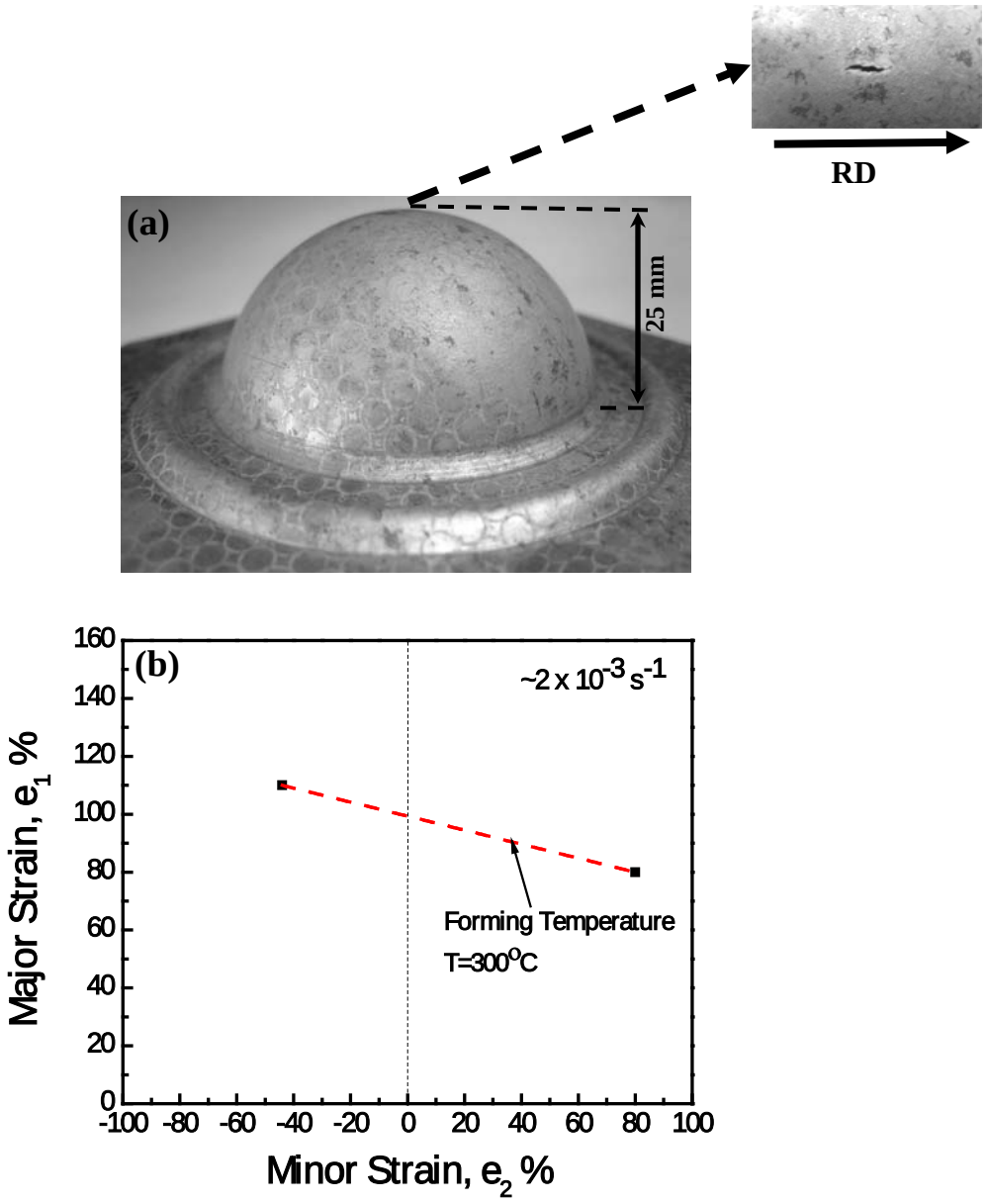

Figure 1.11 (a) Superplastically formed dome of ABRC-processed AZ31C Mg alloy, starting grain size of the alloy ~ 1.1 μm. A dome height of 25 mm is achieved at biaxial forming temperature of 300°C in 5 mins. The magnified view shows the fracture region is oriented in the rolling direction. In (b) forming limit strains are plotted for forming temperature of 300°C at ~ 2 x 10^{-3} s^{-1} strain rate (uniaxial tension test data was also included to obtain this plot).

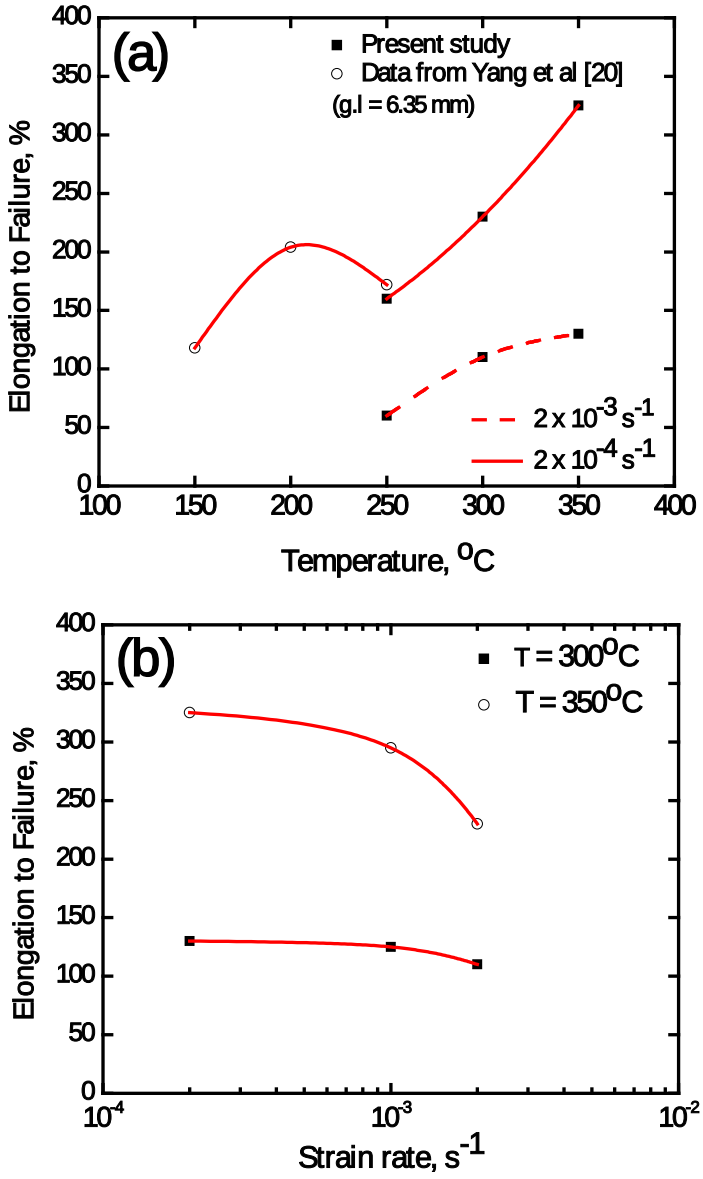

Figure 1.12 (a) Shows variation of elongation-to-failure of the as-processed AZ31C alloy at strain rates of 2 x 10^{-3} s^{-1} and 2 x 10^{-4} s^{-1}. Data from Yang et al. are included for comparison. (b) Shows the variation of elongation of the as-processed alloy with strain rate at selected temperatures of 300°C and 350°C.

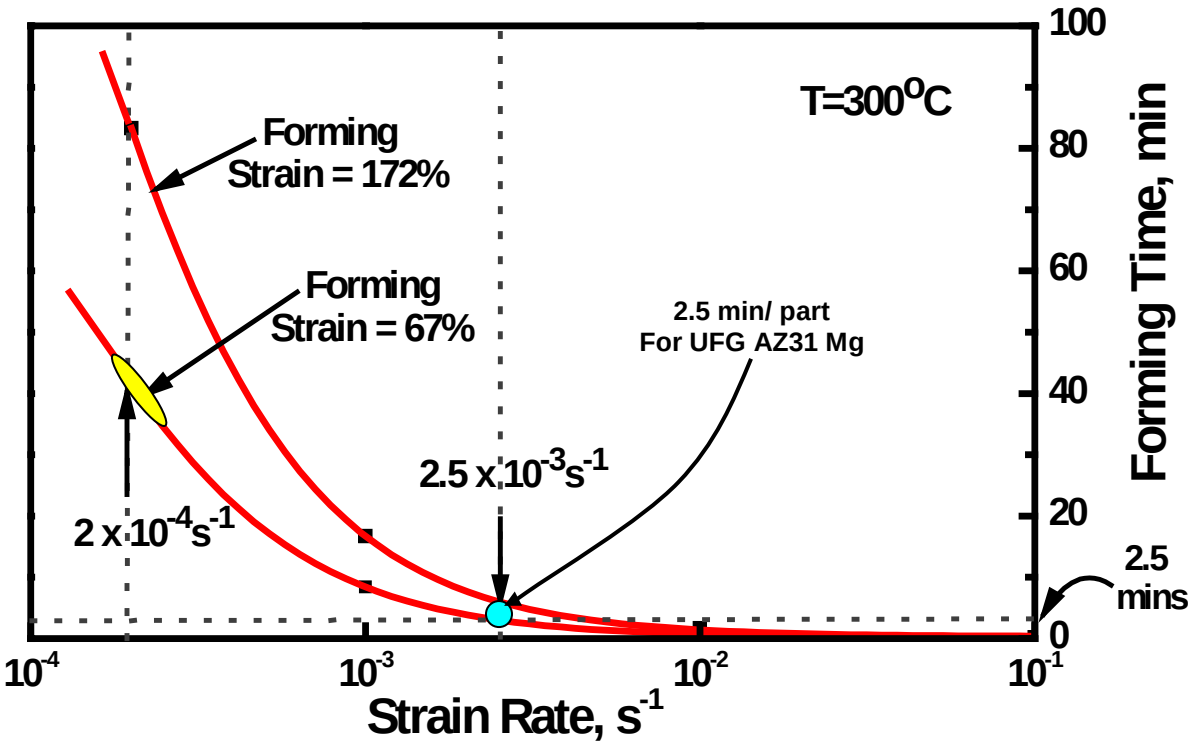

Figure 1.13 Forming time versus strain rate at 300°C expected on the basis of biaxial and uniaxial tensile elongations for UFG AZ31C, representing potential for low temperature superplasticity.

Appendix 1.A

ROOM TEMPERATURE MECHANICAL PROPERTIES

A1. Vickers Microhardness

Vicker's microhardness of twin-roll cast AZ31C Mg samples was determined for as-received and as-processed condition. Additional hardness measurements were made on ABRC-processed and hot rolled Mg. Measurements of Vickers microhardness indicated that hardness increases with decreasing grain size. This establishes the significance of grain size strengthening. Fig. A.1 shows the microhardness data plotted with the abscissa of Hall-Petch equation, i.e. inverse square root of the grain size (d). ABRC processed Mg is clearly superior in grain size strengthening. The Data from Yang et al. [28] are included in the plot for ABRC processed AZ31B Mg. Yang's data was for the hot-rolled AZ31B wrought starting material, but the grain strengthening follows a similar trend. The ABRC-processed and hot rolled AZ31C Mg shows higher microhardness even after the high-temperature finish rolling.

A2. Room temperature tensile test

The room temperature uniaxial tensile test plots for as-received and processed conditions of AZ31C Mg alloy are shown in Fig. A.2. The associated room-temperature mechanical properties of ABRC- processed and hot rolled AZ31C Mg alloy are give in Table. A.1. Data from Yang et al. are included for comparison [1, 20]. Significant increase in yield and tensile strength were observed. Total elongation of UFG Mg is superior to the coarse grain as-received material.

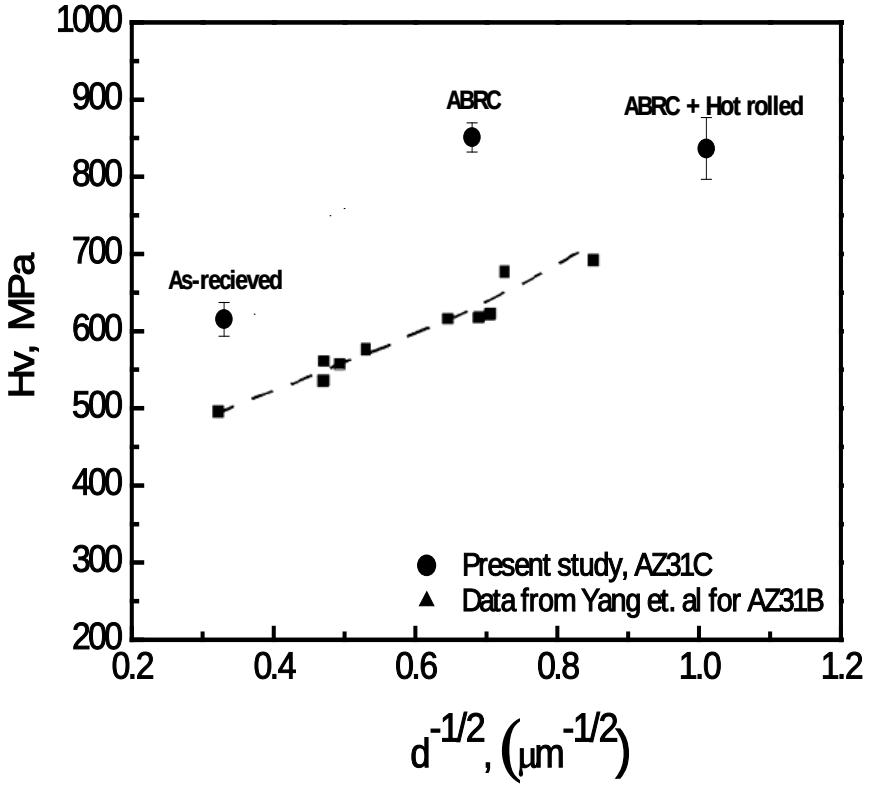

Figure A.1 Vickers microhardness versus grain size of twin roll cast AZ31C Mg. Data from Yang et al. have also been included for comparison [28].

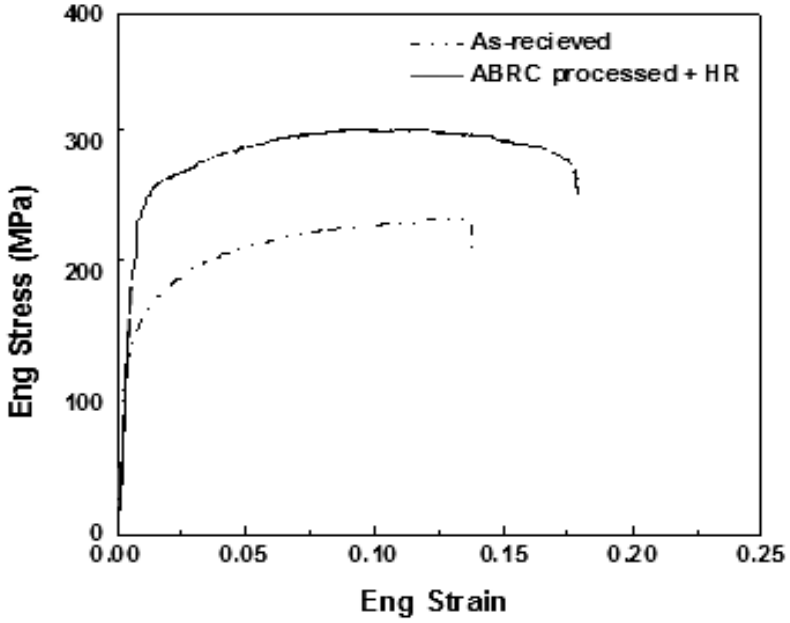

Figure A.2. Stress–strain curves in tension for as-received and as-processed AZ31C Mg.

Table A.1 Vickers microhardness versus grain size of twin roll cast AZ31C.

Test Condition	Yield Strength (MPa)	Ultimate Tensile Strength (MPa)	Total Elongation (%)	e_u, (%)	e_{pu}, (%)
Twin roll cast AZ31C	135	230	14.2	12.8	1.4
ABRC processed + HR AZ31C	245	305	18.5	11.5	7.0
ABRC processed AZ31B [20]	280	308	22.6	8.4	14.2

*Properties were determined from 12.7 mm gauge length sample.

1.6 References

[1] Q. Yang and A.K. Ghosh, *Acta Materialia*, 54 (2006), 5147-5158.

[2] B.L. Mordike and T. Ebert, *Mater. Sci. Eng. A*, 2001, vol. 302, 37–45.

[3] S. Schumann and H. Friedrich. *Mater. Sci. Forum*, 419–422 (2003), p. 51.

[4] J. Goken, J. Bohlen, N. Hort, D. Letzig and K.U. Kainer, *Mater. Sci. Forum* 426–432 (2003), 153

[5] L. Riopelle, *JOM*, 48(1996), 44-46.

[6] A. Takara, K. Higashi ,*Materials Science Forum*, v 475-479, pt.1, p 509-12, 2005

[7] E.F. Emley, *Principles of magnesium technology*, Pergamon Press Ltd, 1966.

[8] P.B Partridge, *Metallurgical Review*, 118(1967), 169-194.

[9] F.W. Bach, M. Rodman, M. Schaper, A. Rossberg, E. Doege and G. Kurz, *Magnesium*, Wiley-VCH, Weinheim, Germany (2004), p. 285.

[10] E. Doege and K. Droder, *Journal of Materials Processing Technology*, 115 (2001), 14-19.

[11] G. Song and A. Atrens, Advanced Engineering Materials A, 9 (2007), 177-183.

[12] F. H. Froes, D. Eliezer and E. Aghion, *JOM*, 50(1998), 30-34.

[13] R.Z. Valiev, N.A. Krasilnikov and N.K. Tsenev, *Mater Sci Eng A* 137 (1991), p. 35.

[14] L.R. Cornwell, K.T. Hartwig, R.E. Goforth and S.L. Semiatin *Mater. Characterization* 37 (1996), p. 295.

[15] Berbon, P.B.; Tsenev, N.K.; Valiev, R.Z.; Furukawa, M.; Horita, Z.; Nemoto, M.; Langdon, T.G. ,*Metallurgical and Materials Transactions A*, v 29A, n 9, p 2237-43, Sept. 1998.

[16] K. Kubota, M. Mabuchi and K. Higashi, *J Mater Sci* 34 (1999), p. 2255.

[17] A.V. Sergueeva, V.V. Stolyarov, R.Z. Valiev and A.K. Mukherjee. *Scripta Mater.* 439 (2000), p. 819.

[18] F. A. Lowenheim, *Electroplating* , McGraw-Hill Book Co., New York, 1978.

[19] U. Erb and A.M. El-Sherik, U.S. patent 5,352,266 (1994).

[20] H.J. Fecht et al., *Metall. Trans.*, 21A (1990), pp.2333–2337.

[21] B. Vyletel.; A.K Ghosh ; D.C VanAken, *Microcomposites and Nanophase Materials. Proceedings of a Symposium held at the 120th Annual Meeting of the Minerals, Metals and Materials Society*, p 137-48, 1991.

[22] R. Mehrabian, *International Metals Reviews*, 27(1982), 185-208.

[23] H .Watanabe, T. Mukai, M. Mabuchi, K. Higashi *Acta Materialia*, 49(2001) 2027-2037.

[24] V.M. Segal, *Mater. Sci. Eng. A*, 197(1995), p. 157.

[25] R.Z. Valiev, A.V. Korznikov and R.R. Mulyukov, *Mater. Sci. Eng. A* ,186 (1993), p.141.

[26] Y. Saito, N. Tsuji, H. Utsunomiya, T. Sakai, R.G. Hong, *Scripta Materialia*, 9(1998), 1221-1227.

[27] J.W. Yeh, S.Y. Yuan and C.H. Peng, *Mater. Sci. Eng.* A252 (1998), p. 212.

[28] Q. Yang, PhD thesis, University of Michigan, Ann Arbor (2005).

[29] X. Li , A.K. Ghosh and R. Decker, *Magnesium Technology 2007*, p 221-226

[30] B. Mansoor, S. Mukherjee, A.K. Ghosh, *Mater. Sci. Eng. A*, 512 (2009) 10–18

[31] A.K. Ghosh and W. Huang, *Investigations and Applications of Severe Plastic Deformation*, NATO Science Series, Boston, Kluwer Academic, 80 (2000), 29-36.

[32] A.K. Ghosh, R.F. Decker, U.S. patent application 11/425,067, (2006).

[33] H. Watanabe, T. Mukai and K. Higashi *Scripta Mater* 40 (1999), p. 477.

[34] T. Mohri, M. Mabuchi, M. Nakamura, T. Asahina, H. Iwasaki, T. Aizawa, *Mater Sci Eng A* 290 (2000), p. 139.

[35] H. Watanabe, T. Mukai, M. Kohzu, S. Tanabe and K. Higashi *Acta Mater* 47 (1999), p. 3753.

[36] X. Wu and Y. Liu: *Scripta Mater.*, 2002, vol. 46, pp. 269–74.

[37] M. Mabuchi, T. Asahina, H. Iwasaki and K. Higashi. *Mater. Sci. Technol.* 13 (1997), pp. 825–831.

[38] M. Mabuchi, K. Ameyama, H. Iwasaki and K. Higashi *Acta Mater* 47 (1999), p. 2047.

[39] A Bussiba, A Ben Artzy, A Shtechman, S. Ifergan and M. Kupiec, *Mater. Sci. Eng. A*, 302(2001) 56–62.

[40] R. V. Allen, D. R. East, T. J. Johnson, W. E. Borbidge, D. Liang, *Magnesium Technology 2001*, ed. J. Hryn, (2001), 75-79.

[41] H. Watari, T. Haga, K. Davey, H. Ona, S. Izawa, H. Hamano, T. Iwashita and M. Nakayama, *Mater. Sci. Forum* 426–432 (2003), 617–622.

[42] T. Haga, K. Takahashi, M. Ikawa and H. Watari, *J. Mater. Process. Technol.* 153–154 (2004), 42–47.

[43] H. Watari, T. Haga, N. Koga and K. Davey, *J Mater Process Technolgy*, 192–193 (2007), 300–305.

[44] M. Numano, N. Mori, Y. Nakai, N. Kawabe, *Mater. Sci. Forum*, 539(2007), 1650-1655.

[45] P. Friedman and A.K. Ghosh, *Metallurgical and Materials Transactions A*, 27 (1996), 3030-3042.

[46] D.H. Bae and A.K. Ghosh, *Acta Materialia*, 48 (2000), 1207-1224.

[47] S.E. Ion, F.J. Humphreys and S.H. White, *Acta Metall* 30 (1982), p. 1909.

[48] A. Galiyev, R. Kaibyshev and G. Gottstein, *Acta Metall* 49 (2001), p. 1199.

[49] M.M. Myshlyaev, H.J. McQueen, A. Mwembela and E. Konopleva, *Mater Sci Eng A* 337 (2002), p. 121.

[50] O.D. Sherby and J. Wadsworth, *Progress in Materials Science*, 33 (1989), 169-221.

[51] T.H. Courtney, *Mechanical Behavior of Materials*, McGraw-Hill Science, 1999.

[52] H.J. Frost and M.F. Ashby In: *Deformation Mechanism Maps*, Pergamon Press, Oxford (1982), p. 44.

CHAPTER 2

HIGH STRENGTH ZK60 MAGNESIUM PREPARED BY BIAXIAL CORRUGATED PRESSING AND LOW TEMPERATURE AGING

Abstract

Severe plastic deformation was imparted to homogenize and refine microstructure of an as-extruded ZK60 Mg plate by alternate biaxial reverse corrugated (ABRC) pressing [1]. Studies were conducted on room temperature strength, ductility, crystallographic texture and aging behavior of this alloy. Ultra-fine grained ZK60 Mg sheet with 0.9 μm average grain size was created by biaxial corrugated pressing in the temperature range of 350^{o}C to 165^{o}C followed by flat pressing at 150^{o}C. Room temperature mechanical property evaluation showed that in as-extruded condition ZK60 Mg exhibited high in-plane tensile yield anisotropy due to a pronounced basal texture. In comparison, ultra-fine grained ZK60 Mg exhibited a more isotropic response with a high yield strength > 350 MPa and tensile elongation > 10%. A low temperature aging treatment of ultra-fine grained alloy further improved its mechanical properties. The enhanced strength levels are believed to be influenced by sub-micron grain size and precipitates found in this alloy; while fracture ductility is believed to be strongly influenced by deformation texture.

2.1 Introduction

In recent years, Mg and Mg-based alloys have drawn significant attention as attractive lightweight structural materials due to their high specific mechanical properties. However, as compared to other widely used structural materials e.g. aluminum or steels, magnesium alloys exhibit low strength (~200 MPa) and poor ductility at room temperature [2-4]. In addition, due to hcp crystal structure Mg alloys exhibit highly anisotropic mechanical properties [1]. In addition to the tension compression yield anisotropy, mechanical property anisotropy is manifested on the rolling plane in sheet or plate form. Therefore in order to enable their widespread application, development of high strength and high ductility Mg alloys with isotropic mechanical properties is of considerable interest.

2.1.1 Grain refinement and texture

In wrought Mg alloys, grain size, precipitates and crystallographic texture strongly influence mechanical behavior. Therefore, grain refinement by severe plastic deformation is an important secondary processing practice often applied to strengthen polycrystalline metallic alloys including Mg [5-7]. Among wrought Mg, extruded ZK60 provides a fine grain size and is a favorable starting material for mechanical property improvement by grain refinement. ZK60 Mg has been used as starting material for severe plastic deformation using; for example, Equal Channel Angular Extrusion (ECAE) [8], Differential Speed Rolling (DSR) [9], Cyclic Extrusion Compression (CEC) [10] and Accumulative Roll Bonding (ARB) [11] etc. Fine grained ZK60 Mg with novel textures prepared by these methods exhibited higher tensile elongations of ~ 15-30% but very little improvement in yield strength was reported. Additionally, the plastic response was

highly anisotropic and some directions exhibit lower ductility than their conventionally processed counterparts. Similar results have been reported for other Mg alloys and hcp metallic alloys, where asymmetric textures created during grain refinement lead to increased mechanical anisotropy [12]. This has important implications in the design and fabrication of components from fine grained sheets.

Alternate biaxial reverse corrugation (ABRC) processing routinely produces ultra-fine grained (sub-micrometer or nanometer range) Mg alloy sheets from bulk material (Fig. 1) [1, 13, and 14]. In previous work, UFG Mg alloys with grain sizes of 0.9 – 1.2 μm with random distribution of basal texture have been obtained by this method. Microstructural evolution and mechanical properties of ABRC processed UFG Mg alloys has been reported [12, 14]. Therefore, the first objective of this work is to examine the possibility of improving both strength and ductility by creating ultra-fine grain size with randomly distributed basal texture in an as-extruded ZK60 Mg sheet.

2.1.2 Precipitation hardening of Mg-Zn alloys

Mg-Zn alloys have strong response to age hardening [15, 16]. Elemental addition of zirconium to Mg-Zn alloys reduces grain size during solidification and improves precipitation hardening properties [17]. Among Mg-Zn alloys, ZK60 Mg has shown better potential for strength enhancement by aging treatments [15]. Several types of precipitates have been identified in age-hardened Mg-Zn alloys (Fig. 2). In particular, age hardening behavior has been related to the precipitation of transition phase β_1' as it effectively pins dislocation movement on basal planes in Mg-Zn-Zr systems [17]. Therefore, the second objective of this work is to study effect of aging treatments on strength of UFG ZK60 Mg sheet prepared by ABRC processing.

The goal of this paper is to examine the effects of grain refinement, texture and aging on strength, ductility, anisotropy and twinning behavior of UFG ZK60 Mg alloy at room temperature.

2.2 Experimental

2.2.1 Materials

The ZK60A Mg alloy in T5 temper (solution treated at 535^{o}C for 2 hrs, quenched in hot water, and aged at 185^{o}C for 24 hrs) was received in the form of 19 mm thick extruded flat bar from Timminco Ltd., USA. The nominal composition range of this alloy is given in Table. 1.

Prior to deformation processing the 19 mm thick ZK60 flat bar was hot pressed at 400^{o}C to create 3mm thick starting material. The compression-axis during hot processing was parallel to the normal direction of extruded bar

2.2.2 ABRC processing

The details of ABRC process were previously described in Ref. [1] and a schematic illustration of ABRC process is presented in Fig. 1.

In present study, a flat 89 mm x 89 mm work-piece with thickness 3 mm cut from the hot pressed ZK60 Mg plate was isothermally pressed and corrugated between corrugated dies with lateral constraint. A total of 6 ABRC processing cycles were performed on the work-piece. During first 3 cycles deformation temperature was varied from 350^{o}C to 315^{o}C. At this stage, a flattening step was performed at 315^{o}C to create a sheet thickness of 1.5 mm. The 1.5 mm sheet was further processed by 3 more ABRC processing cycles and deformation temperature was progressively lowered from 265^{o}C to 165^{o}C. A final

flattening step was performed at 150^{o}C to create a sheet thickness of 0.75 mm. The cumulative plastic strain in the sheet after 6 ABRC cycles was about ~8.0.

At different stages of ABRC processing, flattening steps were performed at cycle temperatures to create 0.75 mm thick samples for characterization and mechanical testing. The characterization samples taken from work-piece were assigned three orthogonal directions. As shown in Fig. 1(b), D1 and D2 are orthogonal sheet plane directions and ND - is normal to the flattening plane. The details of sample sizes, various processing parameters and imparted deformation strains for ABRC are summarized in Table 2 and 3.

2.2.3 Microstructure characterization

The microstructural examination was done on the as-extruded, hot rolled and ABRC processed ZK60 Mg. The as-extruded samples were sectioned in a plane containing the normal direction and extrusion direction. Hot rolled samples were sectioned in a plane containing normal direction and rolling direction. ABRC processed samples were sectioned in a plane parallel to the plate normal direction The metallographic specimens were cold mounted in self-curing resin, fine ground and mechanically polished and were later etched with acetic-picral solution. The acetic-picral solution contains 4.2 g picric acid, 70 ml ethanol, 10 ml acetic acid and 10 ml distilled water. Cross-sectional microstructures of the specimens were examined using optical, scanning electron and transmission electron microscopes. A Philips XL30-FEG SEM was employed to observe the very fine microstructure at higher magnifications. The operating voltage was 20-30 kV. Additionally, a Philips CM-12 TEM was used in limited cases to observe nano-scale precipitates and dislocation structure, operating at 120kV. TEM foils

were prepared by twin-jet electro-polishing in an electrolyte of 20% nitric acid in methanol at -30°C. The electro-polishing voltage was 20 V. The grain and particle size was measured from micrographs by an image processing and analysis software ImageJ using a volume based approximation [1]. Grain size analysis was done on five pictures taken from different locations of the sample to achieve statistical reliability.

2.2.4 Aging treatments

To determine the optimal aging conditions for deformation processed material low temperature aging treatments were performed at 110°C, 150°C and 180°C for 5, 10 and 24 hours. The aging treatments were carried out in air inside a Lindberg box electric furnace.

2.2.5 Mechanical tests

Room-temperature mechanical behavior of as-received and processed materials was determined by tension tests. In as-extruded condition 4 mm thick samples were directly machined from the mid-surface of ZK60 Mg bar. The tensile samples had a gauge section of 15 mm long x 3 mm wide. The surfaces of tensile specimens were polished prior to testing. Tests were conducted using a computer-controlled 5505 Instron machine. A 12.7 mm gauge length extensometer, attached to the gauge length, was used to measure the tensile strain. Specimens were tested at a constant crosshead speed of 0.5 mm / min.

2.2.6 Texture measurement

Crystallographic texture measurements were made on the plate/sheet plane using a Rigaku D/MAX-B rotating anode X-ray diffractometer using CuKα radiation at 40 kV and 100 mA. Texture measurements were made for as-extruded, rolled and selected

stages of ABRC processing. Before the pole figures were collected, standard theta-2 theta scans were run to obtain the exact positions of the Bragg peaks. The Schulz reflection method was employed with sample tilt from 15^{o} up to 90^{o} and azimuthal steps of 1.67° over the entire 360°. Corrections for defocusing of the peak and background intensities were made by experimentally measuring pole figures from a fine grained random sample and developing a correction curve. Complete pole figures were obtained for {0002}, {1010} and {1011} from the experimental raw pole figure data using the harmonic method of the "Preferred Orientation Package of Los Alamos" (popLA) software obtained from The Los Alamos National Laboratory.

2.3 Results

2.3.1 Microstructure evolution

This section describes the evolution of microstructure as a function of strain and progressively decreasing deformation temperature as compared with as-extruded alloy. The typical microstructural features of as-extruded ZK60 Mg alloy in T5 condition are shown in Fig. 3. They include bimodal grain structure with distributed bands of 13 μm fine recrystallized grains and 300 μm coarse grains. It can be seen that there is considerable variation in microstructure from one region to another and despite the higher magnification in Fig. 3 (b); structure appears similar as in Fig. 3 (a). The coarse island shaped grains are elongated in the extrusion direction and make up almost 34% vol. fraction of the microstructure. They are believed to be solid-solution deficient in zinc and zirconium and have specific orientation which makes them more resistant to hot working [22]. It should be noted that precipitates formed during aging are irresolvable by optical microscopy even in the artificially aged T5 condition.

Fig. 4 shows photographs using SEM to illustrate the nature of changes occurring at microscale during the grain subdivision process. In Fig. 4 (a), the fine grain size was reduced from 13 μm in the as-received alloy to 7 μm in the sample after deformation a true strain of to 3.0 isothermally at 315°C and correspondingly, the coarse grain size was reduced from 300 μm to 50 μm. The vol. fraction of coarse grains decreased to ~18% as compared to the as-extruded condition. One key observation during this high temperature ABRC are twins that subdivided coarse grains into several small units as shown in Fig. 4 (b). Some new grains are seen near, twin boundries and coarse grain boundries of twinned grains, taking a necklace type structure.

Additional observations confirmed that the grain size reduced with increasing strain more efficiently when deformation temperature is lowered. In Fig. 5 SEM micrographs show the microstructure of ZK60 Mg ABRC samples with strain $\varepsilon = 8.0$ at 150^{o}C. Fig. 5 (a) shows some twinned and flattened out coarse grains with 5 μm avg. sizes in an over-all homogenous microstructure. Microstructure shows that at this stage of ABRC vol. fraction of coarse grains has decreased to ~ 8 %. Fig.5 (b) shows that an ultra-fine grain structure of 0.9 μm average grain size evolved in ABRC processed ZK60 Mg alloy.

Although not much grain growth was observed during 150^{o}C and 180^{o}C aging treatments, tension tests and hardness measurements indicated some deterioration in mechanical properties of fine grain ZK60 Mg. Even short aging periods at these conventional temperatures lead to extensive formation of the undesirable β_2' precipitates. However, aging at 110^{o}C for 10 hrs lead to improvement in mechanical properties of UFG Mg. TEM images in Fig. 5 show ARBC samples before and after the aging

treatment. In Fig. 6(a) with strain ε = 6.0 at 250^{o}C, several sub-micron grain are highlighted in the microstructure. The average grain size for fine grains at this stage is 2.5 μm. Some round shaped coarse precipitates are also seen in the microstructure (indicated by arrows). These maybe inhomogeneously distributed β_2' precipitates that occupy < 5% vol. fraction. Fig. 6(b) shows dislocation and precipitation structure in the ultra-fine grained ZK60 Mg alloy after heat treatment at 110^{o}C for 10 hrs. The TEM image show some dislocation density around sub-micron sized grains. In the inset, highlighted region show homogenously dispersed 30-50 nm fine precipitates. Two distinct types of precipitates β_1' and β_2' have are identified. The vol. fraction for β_1' precipitates at this final stage was ~12%. It must be noted that only preliminary TEM data for aged ABRC processed ZK60 Mg has been presented here, but this topic will be explored in greater detail in future work.

2.3.2 Texture evolution

Crystallographic textures of ZK60 Mg in T5 temper are shown in Fig. 7 (a) by complete pole figures for {0002}, {1010} and {1011} planes. The basal poles have highest intensity of ~6 multiples of a random distribution (MRD) and distant peaks are observed in the TD. The basal and prism pole figures reveal that in as-extruded condition grains with basal {0002} and prismatic {1010} planes lie parallel to the sheet plane with their c-axis perpendicular to the extrusion direction. However the intensity of prism poles is less and the basal poles with high intensity dominate. Therefore, the texture of as-extruded ZK60 Mg alloy in T5 condition can be characterized as basal texture parallel to sheet plane with some tilting of the basal poles in the transverse direction. Distribution

of basal poles orthogonal to extrusion direction after warm extrusion has also been extensively documented in other magnesium alloys [18, 19].

The pole figures for the ABRC processed materials are also shown in Fig. 7. The pole figures clearly demonstrate the different stages of texture evolution for ABRC. In Fig. 7 (b) ε = 3.0 at 315^{o}C, condition the density of basal poles is asymmetrically distributed around ND with the maximum located away from normal direction. The highest intensity of basal poles is ~12 MRD. In Fig. 7(c) for condition ε = 6.0 at 250^{o}C, the intensity of basal poles has decreased to ~ 4 MRD. However, the density of basal poles is evenly distributed and maximum intensity is located at normal direction. In Fig. 7 (d) for condition ε = 8.0 at 150^{o}C, the intensity of basal poles showed some increase to ~ 6 MRD. The intensity of basal poles after completion of ABRC processing is comparable to as-extruded condition. The basal poles show a much broader distribution around normal direction. There is possibly a tilt for basal poles about 40^{o} between D1 and D2 (so called shear plane). Overall intense shear deformation imparted during ABRC processing leads to decrease in basal texture intensity with increasing strain and decreasing deformation temperature. Pole figures measured for ABRC processed ZK60 Mg after aging 110^{o}C aging treatments show very little texture changes and are therefore not presented here.

2.3.3 Mechanical properties

Room temperature engineering stress strain curves of samples machined in orthogonal in-plane directions for as-extruded, ABRC processed and aged conditions are presented in Fig. 8 (a). Values of yield stress, ultimate tensile strength, and strain-to-failure are summarized in Table 3. It can be clearly observed that in as-extruded

condition mechanical properties are directionally dependent and exhibit a high degree of tensile yield anisotropy. The as-extruded T5-aged samples exhibit moderate strength and ductility. As shown in Fig. 8 (a) and Table. 3, in the as-extruded condition extrusion direction tension specimens exhibit much higher yield strength as compared to transverse direction specimens. The yield strength of 237 MPa in extrusion direction is almost 80% higher than transverse direction yield strength. However, the tensile elongation in the transverse direction was ~20% more.

Room temperature engineering stress strain curves for ABRC processed and aged samples exhibit much more balanced mechanical properties. Values of yield stress, ultimate tensile strength and strain-to-failure are summarized in Table 4. The following can be inferred from the plot and the table. First, the ABRC processed materials exhibit improved planar isotropy in strength and ductility compared with the as-extruded counterparts. Second, the yield and ultimate strength of processed material increases with decrease in grain size. Third, while yield strength significantly increased after ABRC processing, tensile elongation decreased due to a severe loss of work-hardening capability as compared to coarse grain counter parts. The mechanical data reported here is for the peak aged condition. Aging treatment at 100^{o}C for 10 hrs significantly improved the strength of processed material.

Over all, the 0.9 μm ultra-fine grained ZK60 Mg after aging exhibited the highest strength (YS= 362 MPa, UTS = 410 MPa); while superior ductility of 15% was achieved for ~ 0.9 μm sample. Aging restored some ductility lost during ABRC processing. It is important to note that the current ductility improvement after aging was attained simultaneously with the strength improvement. The mechanical data presented in Figure.

8(b) shows that ABRC-processed UFG ZK60 is far superior to fine grain counterparts processed by other methods [8-11]. The different strain hardening rate trends between as-extruded and processed material indicate that a different deformation mechanism may be operative.

2.4 Discussion

2.4.1 Microstructure evolution:

In present work it was found that with deformation: (i) the grain size gradually decreases with increase in accumulated strain and decrease in deformation temperatures, (ii) the microstructure becomes refined and more homogenous in comparison to the as-extruded alloy, (iii) twinning along with basal slip plays an important role in accommodating large plastic deformation during grain sub-division process. These findings are in strong agreement with our previous work on grain refinement in Mg alloys by ABRC [1, 8, and 12].

The mechanisms of grain refinement and extent of microstructural homogeneity in ABRC processing of Mg were discussed in Ref. [1, 2, and 12]. It is very well known that new grains nucleate at grain boundaries and twin boundaries in deformed material [20, 21]. New grains, nucleated at twin boundaries cause further grain refinement by dynamic recrystallization [1]. Twin boundaries provide recrystallization nuclei due to the high misorientation across them. At early stages of deformation and even at high processing temperatures, grain sub-division in coarse grains occurs mainly by twinning. Recrystallized fine grains surrounding coarse grains and twins take the appearance of “necklace-type structure”. This peculiar microstructural feature occurs by nucleation and growth of new grains and recovery of deformed structure [1]. At larger strains and lower

deformation temperatures, some amount of continuous dynamic recrystallization and greater degree of storage of dislocations combined with limited amount of recovery appears to be the primary mechanism of grain refinement [1].

The uniformity of grain refinement process is critical particularly in Mg alloys. Grain refinement tends to saturate at large strains and some fragments of coarse grains may be difficult to breakdown. It was found that after true strain 8.0 at 150°C, coarse grains population almost merged in with fine grains and their vol. fraction was reduced to only 8%. It must be noted that in present work more strain was imparted to achieve UFG Mg as compared to Yang and Ghosh's work on AZ31B Mg (~1.4 μm average grain size, A_f = 97.2, true strain 5.0). This may be explained by the fact that in present work initial ABRC cycles were performed at much higher temperature of 350^{o}C. High temperature severe deformation leads to formation of LAGB and it is difficult to further subdivide g.s without decease in temperature. The investigations on the effects of strain and deformation temperature on the resulting grain size indicate that with proper control of parameters, UFG Mg alloy could be obtained from extruded alloy by ABRC processing. This work provides further evidence that ABRC process can be successfully applied to refine and homogenize a variety wrought Mg alloys with different compositions.

2.4.2 Texture evolution

The entire course of texture evolution can be determined by the geometry of ABRC process where uniform shear deformation is induced throughout thickness of sheet. When the initial corrugated pressing step is performed on the Mg plate under iso-thermal high temperature condition, basal slip alone cannot accommodate the imposed

plastic strain. Due to processing by asymmetrically corrugated dies shear planes inclined to the plane of the sheet are generated and a resolved component of the applied compressive force results in shear stress along basal planes. This leads to basal slip and possibly $\{10\bar{1}2\}$ twinning during corrugated pressing. The shear plane may rotate the texture components and re-locate them, thereby broadening the angular distribution of basal poles around ND. In addition to that, this rotation maybe a result of the strain-path change superimposed upon a rotation around ND and in-plane directions of the work-piece during next deformation steps. It is also worth mentioning that flat pressing step after every 4 corrugated pressing steps has the tendency to align the shear planes with ND plane [1], which may explain increase in the intensity of basal poles after the final flattening step. Overall basal slip dominates deformation processes at elevated temperatures during much of the ABRC process. The intensity of basal texture increases with increasing strain and decreasing temperature. As grain size gets finer, the operation of grain boundary sliding or shearing becomes increasingly easier so that plastic deformation in all directions can be accommodated [1,8]. Grain rotation due to this effect can possibly allow the intensity of basal texture to decrease and the distribution of basal poles to become broader. The change in the grain size follows an opposite trend as the intensity of basal texture follows with strain, possibly because deformation twinning is activated under compression for basal-textured Mg, and higher strain and finer grain size inhibit both [1]. In summary, the shear plane effect during corrugated pressing and shear reversal effect during flat pressing combine to yield observed textures.

2.4.3 Improvement in strength and ductility

(a) Factors effecting strength:

It is considered that fine-grain strengthening and precipitation hardenings are dominant factors responsible for the high strength of UFG Mg. The ABRC texture best explains ductility and reduced planar anisotropy between RD and TD. An analysis to estimate the enhancement in strength due to grain size and precipitation strengthing was carried out by W.J. Kim et al. for AZ91 Mg [33]. We adopt a similar approach to understand the factors effect strength in ZK60 Mg. The YS increment due to grain-size strengthening $\Delta\sigma_{g.s}$, may be estimated using a standard Hall–Petch equation [23, 24]:

$$\Delta\sigma_{g.s} = \sigma_o + kd^{-0.5} \quad (1)$$

where d is the true grain size, k is Hall–Petch coefficient and σ_o is the friction stress (For pure Mg, k = 0.29 MPa $m^{0.5}$ and σ_o = 25 MPa [25]). The yield strength of UFG alloy is higher due to its finer structure (i.e. smaller obstacle spacing) and large vol. fraction of grain (or sub grain) boundaries. UFG Mg has reduced strain hardening rate and low uniform strain due to increased grain boundaries as they act as sinks and sources for lattice dislocations [1,8].

Fig. 10(b) schematically shows the preferred orientation and morphology of precipitates commonly found in age hardenable ZK60 Mg alloy. Sturkey and Clark identified that in Mg–Zn alloys; the β'_1 precipitate was not an equilibrium phase but rather a transition phase that could be designated as ′MgZn [17]. The disc-shaped precipitate β'_2 formed during over-ageing is the equilibrium MgZn phase. The structures of both precipitates are similar to that of laves phase ($MgZn_2$) [26]. In ZK60 Mg, age hardening behavior has been related to the precipitation of β_1' transition phase [14].

The β_1' precipitates with rod-like morphology and growth direction of [0001], lie on $\{1\,\overline{2}\,\overline{1}\,0\}$ planes. The β_2' precipitates with disc shaped morphology, lie parallel to the {0001} plane of the matrix [26]. The rod-shaped (β_1') precipitates mainly consist of {Mg, Zn}, while disc-shaped (β_2') precipitates, {Mg, Zn, Zr} or {Mg, Zn}. Plastic deformation of Mg alloys at room temperature is dominated by basal slip and since β_1' precipitates are located along the [0001] direction they can effectively pin dislocation movements on basal planes and thereby restrict plane glide. Therefore size and distribution density of β_1' precipitates is a dominant factor in age-hardening of Mg-Zn alloys. On the other hand β_2' has much less effect on hardness because it lies on the basal plane and offers little resistance to dislocation motion. Hardness decline due to over-aging is explained by the transformation of β_1' precipitates into β_2' and decrease in the density of β_1'.

In order to estimate precipitation strengthening, Nie and co-workers developed an Orowan equation for basal precipitate plates which focuses specifically on the β phase in Mg alloys [27]. The equation assumes restricted distribution of precipitate particles to a triangular array on the $(0\ 0\ 0\ 1)_\alpha$ slip plane. According to them, increment in CRSS due to Orowan strengthening $\Delta\tau$, may be expressed as:

$$\Delta\tau = \frac{Gb}{2\pi\sqrt{(1-\upsilon)\lambda}}\ln\left(\frac{d_p}{b}\right) \tag{2}$$

where G is the shear modulus (1.66×10^4 MPa for pure Mg), b is the Burgers vector (3.2×10^{-10} m for pure Mg), v is the Poisson's ratio (0.35 for pure Mg [28]), d_p the mean planar diameter of the point obstacles, and λ is the effective planar inter-obstacle spacing, $\lambda = \left(\frac{0.953}{\sqrt{f_v}} - 1\right) d_p = 1.37 \times 10^{-7}$ m where $f_v = 0.125$ and $d_p = 8.1 \times 10^{-8}$ m). The increment in YS due to Orowan strengthening, $\Delta\sigma_\beta$, is then obtained from the following relation:

$$\Delta\sigma_{\beta} = M\Delta\tau \quad (3)$$

where M is the Taylor factor. Taylor factor value of 4.5 for the randomly textured has been reported [29]. As the ABRC processed Mg has basal fiber texture, a value of $M \approx 2$ may be assumed [29]. By summing the contributions from the grain-size and dispersion-strengthening mechanisms (330 and 78 MPa, respectively), using Eqs. (1) and (3), the YS of the ABRC processed and aged material is computed to be 408 MPa. Nevertheless, the major difference in strength between the calculated (408 MPa) and measured (353 MPa) values may be due to the texture-softening effect [30].

(b) Factors effecting planar isotropy and ductility:

In as-extruded condition, the difference between yield strength along extrusion and transverse directions may be directly related to rotation spread of basal texture [31]. The ABRC-processed Mg with ultra-fine grain size and a broader distribution of basal poles exhibits isotropic planar yield behavior. The grain size and the aging treatment of UFG Mg have significant impact on ductility. However, texture modification by redistribution of basal poles is the most effective method of improving ductility of Mg alloys. The grain size effects ductility by affecting the hardening behavior. Coarse grain structures with high strain hardening rate lead to more elongation to failure as compared to fine grain counterparts. Low temperature aging improves ductility because it doesn't lead a noticeable growth of grains, but results in recovery of the defect structure of the grain boundaries and a sharp decrease of internal stresses [1,8]. This result is very important and shows that not only the mean grain size but also the high density of defects in grain boundaries influences the strength properties of ultra-fine grained materials. The texture of all ABRC samples can be simply expressed as basal fiber texture, which is the

well-known texture component that develops during various wrought procedures of Mg alloys [18, 21]. The broader distribution of the basal texture may not be as effective in improving ductility as the with strong textures developed by ECAP, in which basal planes tend mostly to be associated with high Schmid factors, but it is certainly more desirable for increasing strength and planar isotropy since texture softening and texture asymmetry are less severe in ABRC [1, 10, 18, 30]. Over all the mechanical property improvement is a cumulative effect. The strong influence comes from grain size while precipitation adds to improve superior properties of UFG alloy.

2.5 Conclusions

The results of the investigation led to the following general conclusions:

(1) High-strength and high ductility ZK60 Mg with 0.9 μm ultra-fine grain size can be created by ABRC processing and low temperature aging.

(2) It is found that during ABRC processing with increasing strain and decreasing deformation temperature: (i) the vol. fraction of fine grains dramatically increases; (ii) the vol. fraction of coarse grains decreases; (iii) the difference between grain size of coarse and fine grains also decreases.

(3) Twinning and basal slip are both responsible for grain sub-division to produce a uniform fine grain structure. Production of a fine grain size eventually inhibits twinning and grain sub-division process is mainly driven by basal slip, dynamic recovery and recrystallization. No twinning is observed below a 3-4 μm critical grain size.

(4) The intensity of basal texture increases with increasing strain until twinning is inhibited. After the critical grain size for twinning is achieved basal texture intensity decreases with increasing strain and decreasing grain size.

(5) The processed ZK60 sheet with ultra-fine grain size and broadly distributed basal texture exhibits high yield strength of > 350 MPa and tensile elongations of 12–14%. The UFG ZK60 Mg mechanical behavior is more isotropic than the as-extruded starting material.

(6) The yield strength increases while ductility decreases with decreasing grain size. Additionally, the ductility is strongly influenced by texture and in samples of comparable grain size, ductility decreases with increasing intensity of basal texture.

(7) Aging treatment ultra-fine grained ZK60 Mg at 110^{o}C and 10 hrs results in homogeneous precipitation of (20-50 nm, 18 vol. %) favorably oriented β_1' precipitates. This leads to further improvement in strength by pinning dislocation motion during basal slip. Elongation to failure is also improved in the UFG alloy which may be associated to the removal of residual stresses during aging.

Table 2.1 Nominal composition range of as-extruded ZK60A Mg (in wt. %)

Mg	**Zn**	**Zr**	**other impurities (total)**
Balance	4.8-6.2 %	0.45%	0.30

Table 2.2 Details of high temperature ABRC processing parameters

	Process	Step #	Sample thickness (mm)	Temp. (^oC)	Homogenization Period (mins)	Cumulative mid-plane Strain
ABRC (350-315^oC)	**ABRC Cycle #1**	1	3	350	30	1.3
		2				
		3				
		4				
	Flattening	1	3	350	30	0.3
	ABRC Cycle#2	1	3	315	30	1.3
		2				
		3				
		4				
	Flattening	1	3	315	30	0.3
	ABRC Cycle#3	1	3	315	30	1.3
		2				
		3				
		4				
	Flattening	1	3 (t_f =1.5)	315	30	1.0

* Cumulative plastic strain after 3 ABRC cycles is 5.5. After 3 cycles the work-piece was further processed under low temperature conditions.

Table 2.3 Details of low temperature ABRC processing parameters

	Process	Step #	Sample thickness (mm)	Temp. (^oC)	Homogenization Period (mins)	Cumulative mid-plane Strain
ABRC (265-150^oC)	**ABRC Cycle #1**	1	1.5	265	20	0.45
		2				
		3				
		4				
	Flattening	1	1.5	200	20	0.12
	ABRC Cycle#2	1	1.5	200	20	0.45
		2				
		3				
		4				
	Flattening	1	1.5	180	20	0.12
	ABRC Cycle#3	1	1.5	165	20	0.45
		2				
		3				
		4				
	Flattening	1	1.5 (t_f =0.75)	150	20	1.0

*Cumulative plastic strain after 6 ABRC cycles is ~ 8.0 and a 0.75 mm thick ABRC processed ZK60 Mg sheet with 1.5 µm grain size is achieved.

Table 2.4 Mechanical properties of as-extruded and ABRC-processed ZK60 Mg

Materials	Thickness (mm)	G.S (μm)	Y.S (MPa)	T.S (MPa)	e_f(%)
ZK60-T5 (ED)	4	13	230	296	17
ZK60-T5 (TD)	4	13	120	255	19
ZK60-ABRC (D1) ε **=6.0 at 250°C**	1.5	2.5	265	311	15
ZK60-ABRC (D2) ε **=6.0 at 250°C**	1.5	2.5	272	314	16
ZK60-ABRC+Aged (D1) ε **=8.0 at 150°C**	1.5	2.5	285	342	17
ZK60-ABRC (D1) ε **=8.0 at 150°C**	0.75	0.9	322	374	12
ZK60-ABRC (D2) ε **=8.0 at 150°C**	0.75	0.9	319	374	10
ZK60-ABRC+Aged (D1) ε **=8.0 at 150°C**	0.75	0.9	353	402	14

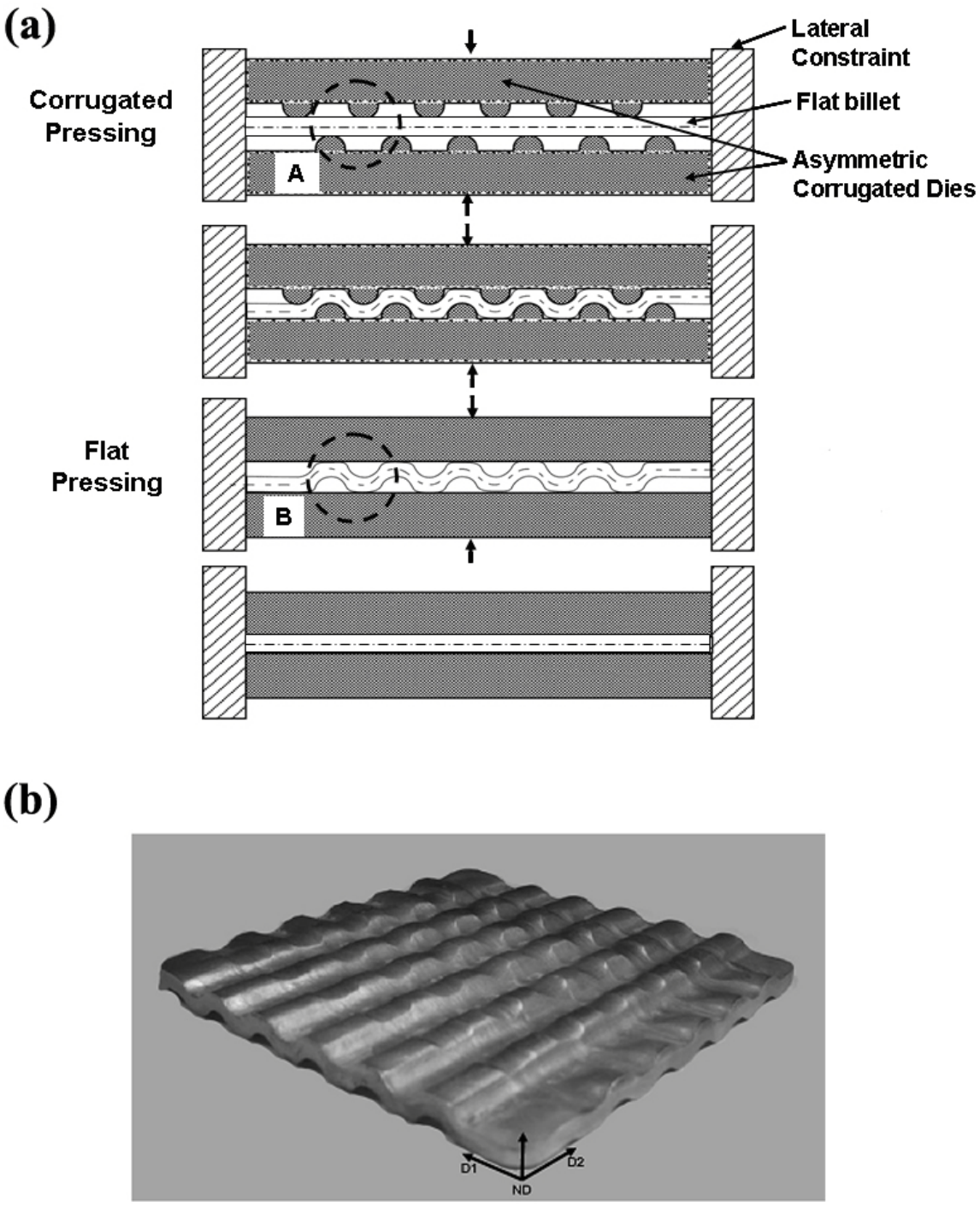

Figure 2.1 (a) Alternate biaxial reverse corrugation (ABRC) process, in which a metal work-piece is repeatedly pressed between asymmetrically corrugated dies with successive 90° in-plane rotations. Schematic shows the work piece under lateral constraint during corrugating and flattening steps. (b) ZK60 Mg work-piece after 4 corrugated pressings.

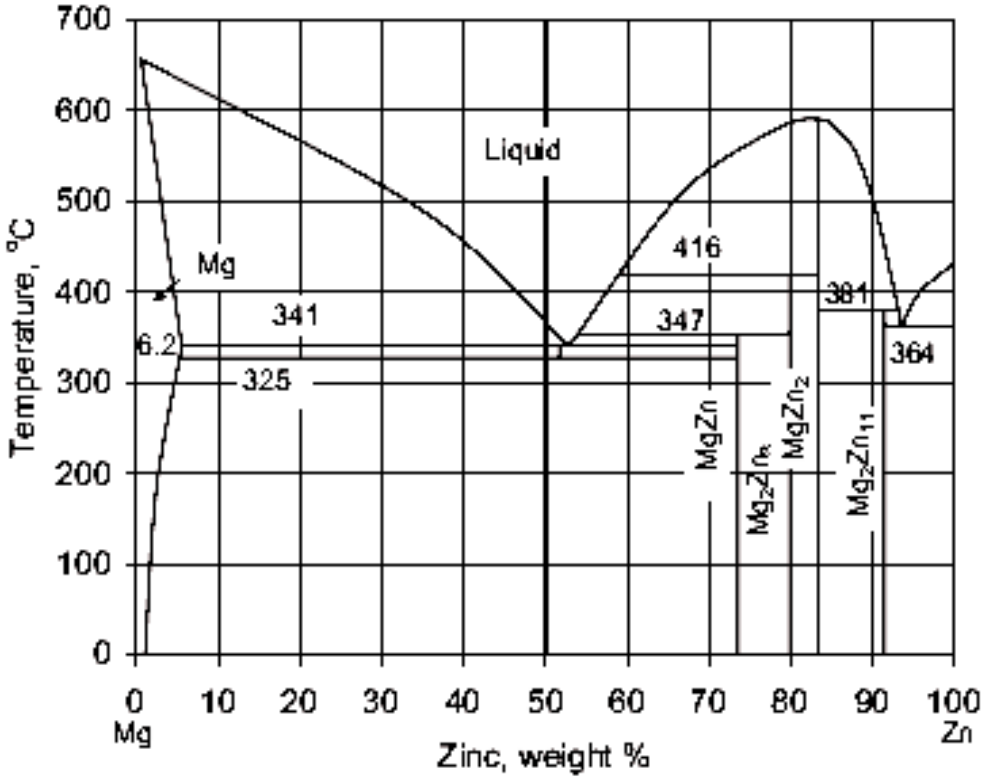

Figure 2.2 The Mg–Zn equilibrium phase diagram [32].

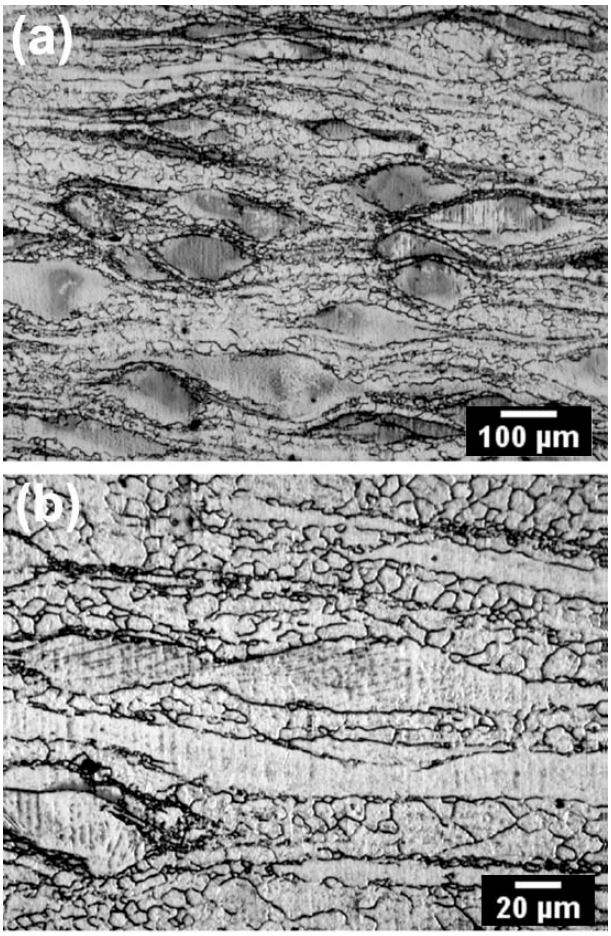

Figure 2.3 Microstructure of as-extruded ZK60 Mg artificially aged to T5 temper. In (a) a longitudinal view shows bimodal microstructure with bands of small 13 µm recrystallized grains and dark island shaped 300 µm coarse grains elongated along the extrusion direction. Coarse grains occupy 35 % vol. fraction of the microstructure. In (b) despite the higher magnification, structure appears similar as in (a). Precipitates formed during aging are irresolvable by optical microscopy.

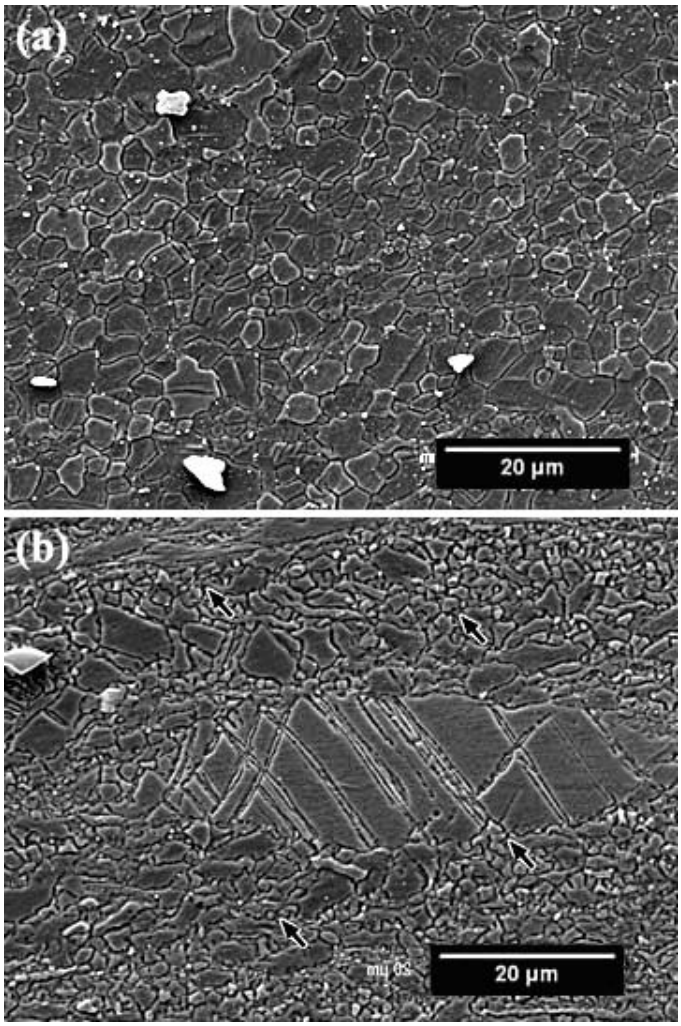

Figure 2.4 Changes in microstructure of ZK60 Mg during ABRC processing. Samples are taken from centre region with strain $\varepsilon = 3.0$ at 315^{o}C. (a) Average grain size of finer grain is ~7 µm. (b) Twinning sub-divided a coarse grain into several units. Average grain size of coarse grain is 50 µm and they occupy 18% vol. fraction of microstructure.

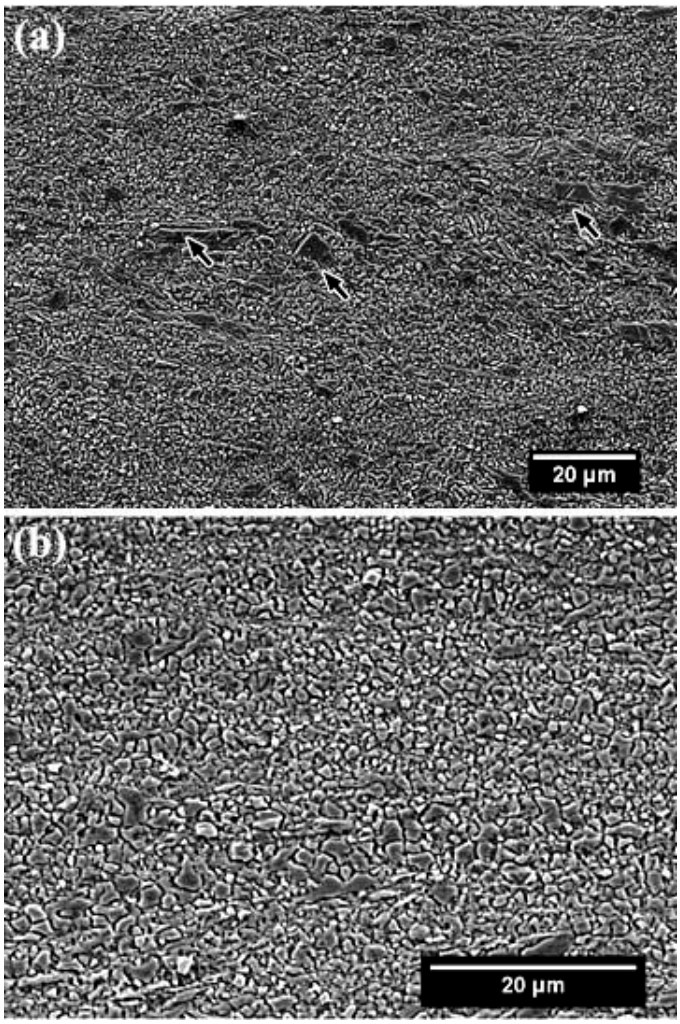

Figure 2.5 Changes in microstructure of ZK60 Mg during ABRC processing. Samples are taken from centre region with strains $\varepsilon = 8.0$ at 150^{o}C. (a) Twinned and flattened out coarse grains with 5 µm average grain size are shown in an over-all homogenous microstructure. Coarse grains occupy < 10 % vol. fraction of microstructure. (b) Ultrafine grain of 0.9 µm average grain size has evolved in the ABRC processed ZK60 Mg alloy at this stage.

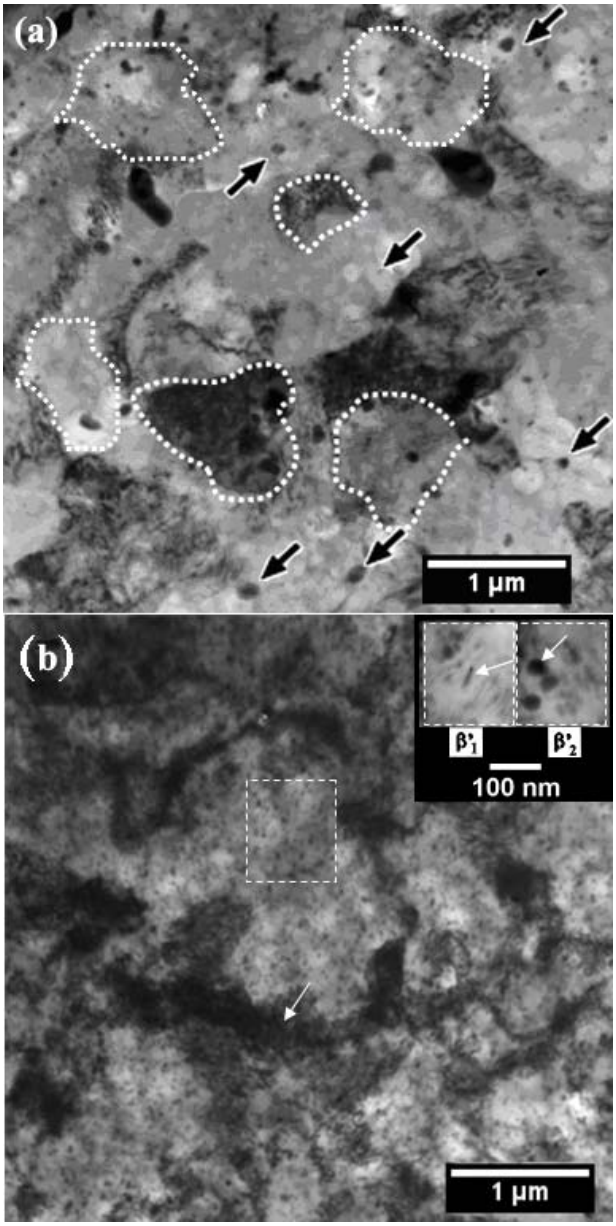

Figure 2.6 TEM image shows microstructure of ABRC processed ZK60 Mg alloy before and after aging treatment. In (a) with strain ε = 6.0 at 250^{o}C, fine grains of ~ 1 μm are highlighted; some inhomogeneously distributed precipitates are also visible in the sample (indicated by arrows). Average grain size for fine grains at this stage of ABRC is 2.5 μm. (b) Dislocation and precipitation structure in ultrafine grained ZK60 Mg alloy aged at 110^{o}C for 10 hrs. In inset, highlighted regions show homogenously dispersed 30-50 nm fine precipitates. Two distinct types of precipitates $\beta_1'$and β_2' are identified.

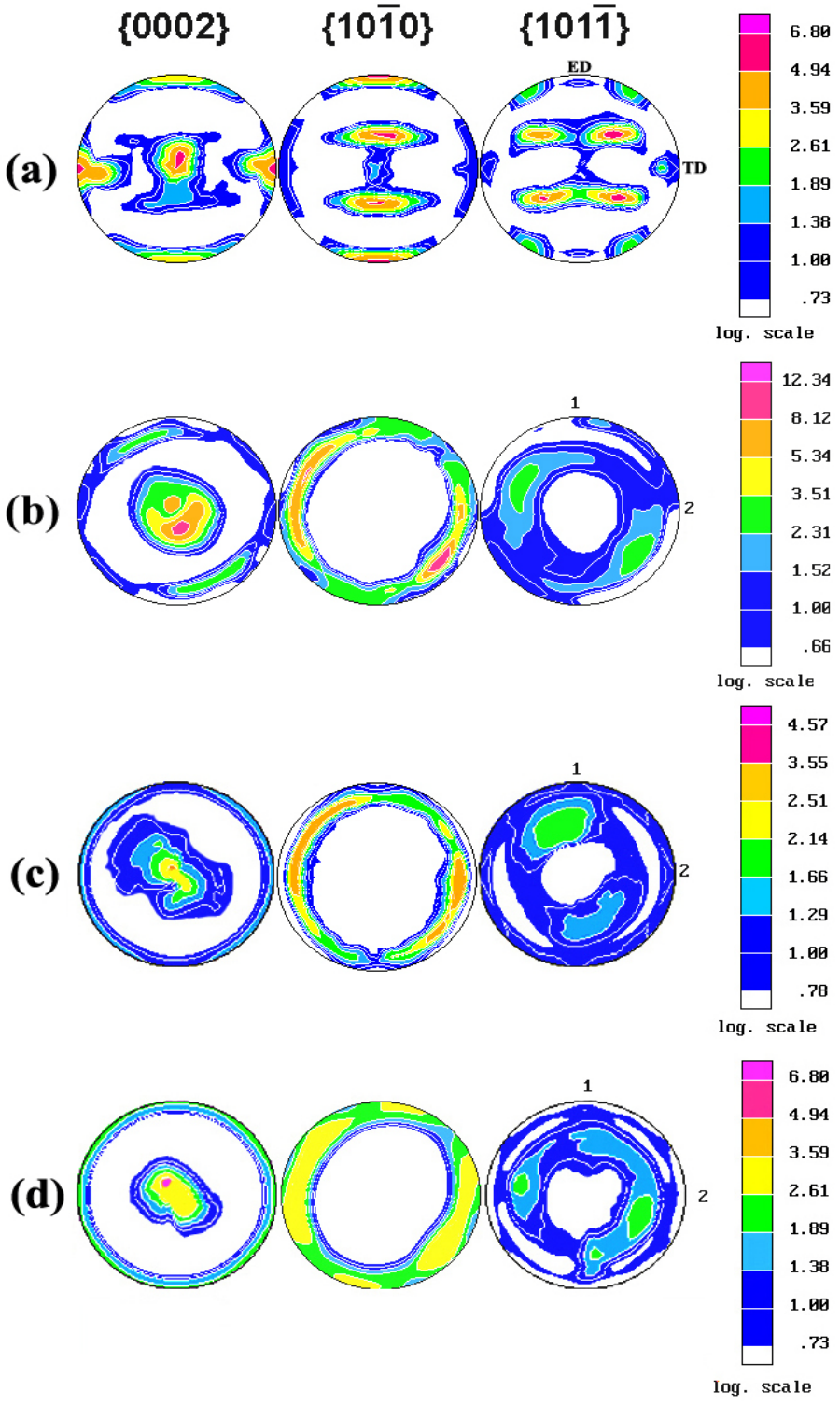

Figure 2.7 Complete pole figure for {0002}, {1010}, and {1011} crystallographic planes for ZK60 Mg in (a) as-extruded; (b) $\varepsilon = 3.0$ at 315°C, (c) $\varepsilon = 6.0$ at 250°C and (d) $\varepsilon = 8.0$ at 150°C.

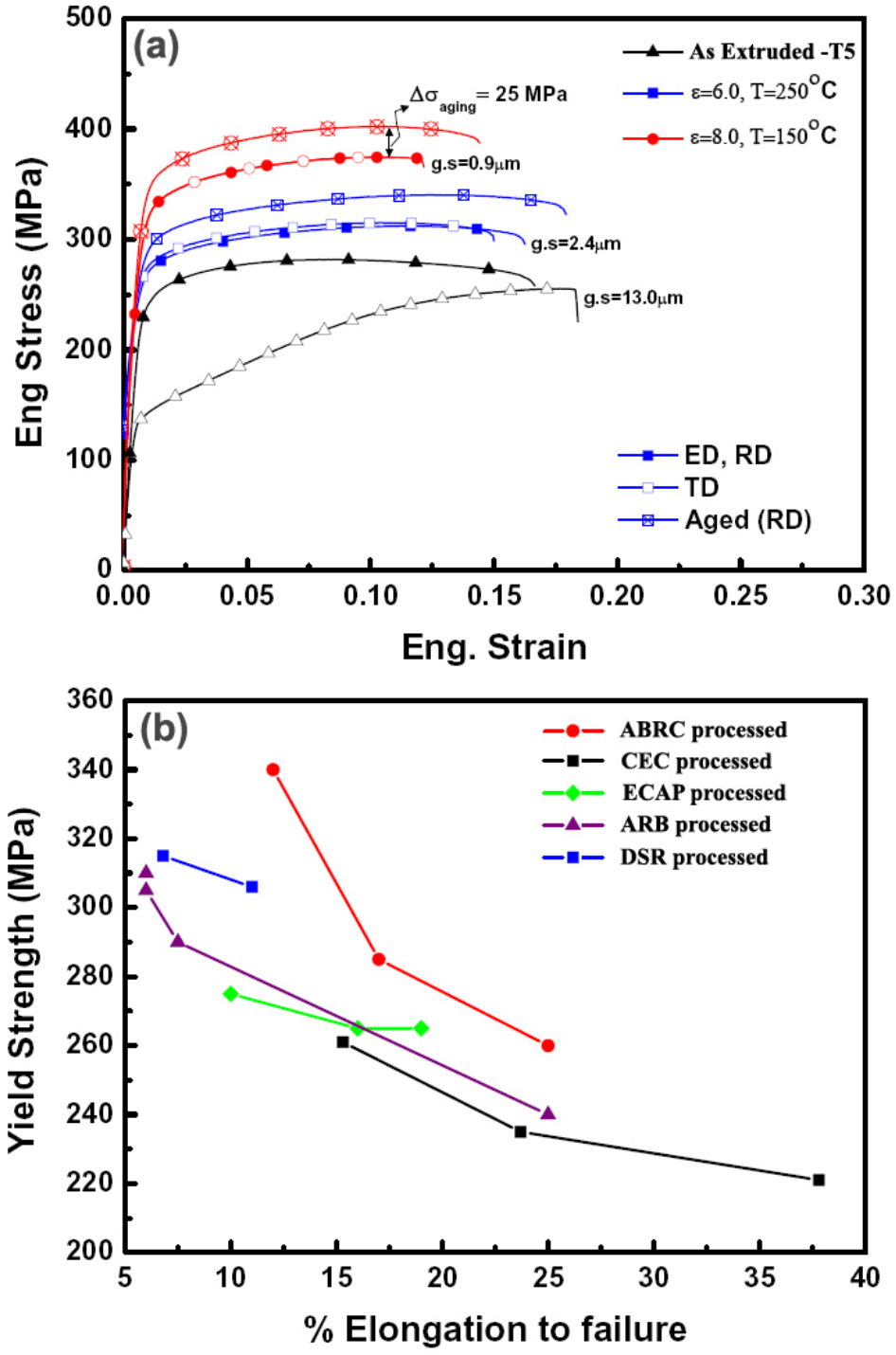

Figure 2.8 (a) Room temperature tensile stress–strain curves for as-extruded, ABRC processed and aged specimens. (b) Strength vs. elongation curves for ABRC processed UFG ZK60 vs. various fine grained ZK60 Mg processed by other severe plastic deformation methods.

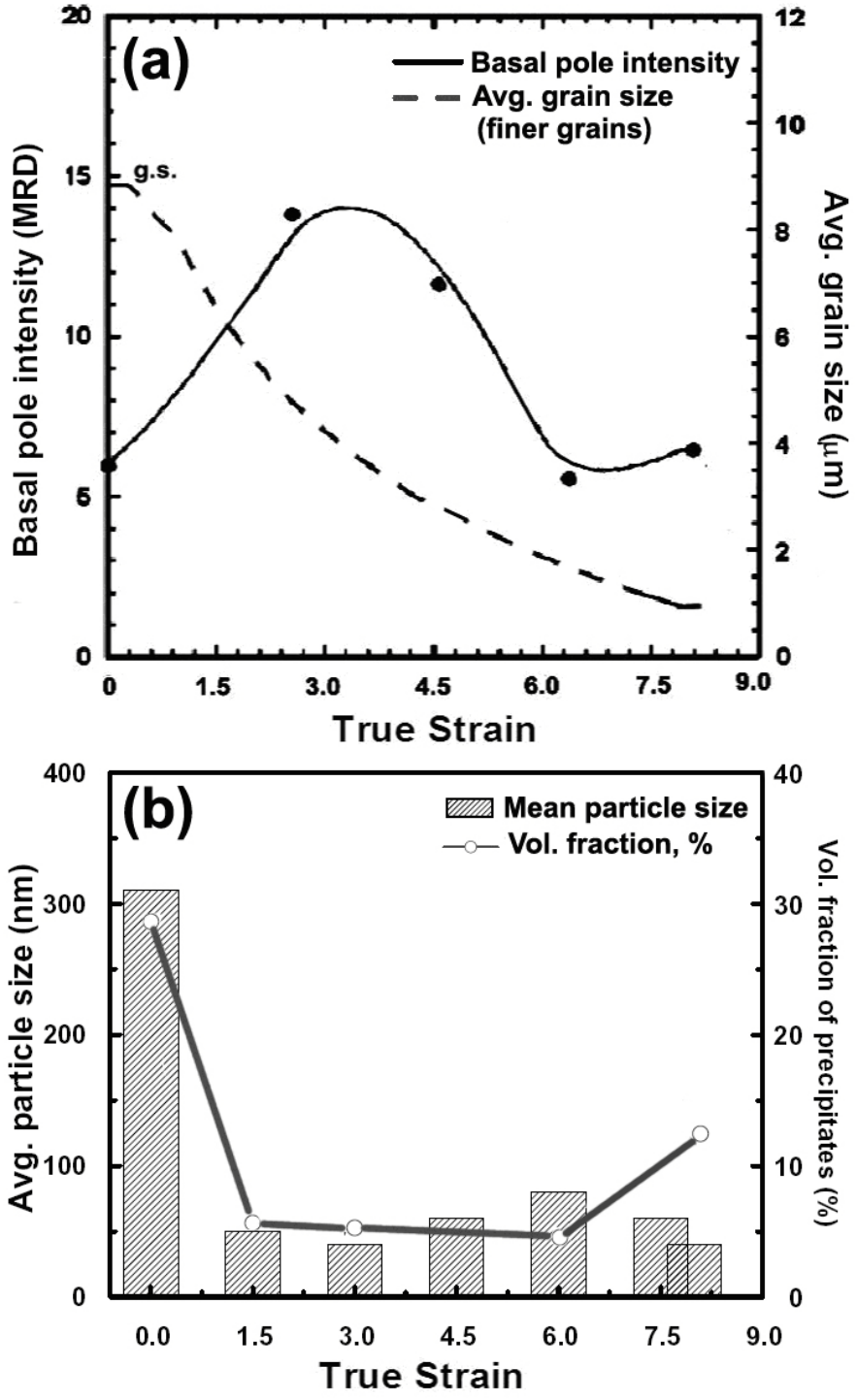

Figure 2.9 (a) Variation of grain size and basal pole intensity with strain. (b) Variation of β_1' precipitate size and % vol. fraction with strain.

2.6 References

[1] Q. Yang and A.K. Ghosh, *Acta Materialia*, 54 (2006), 5147-5158.

[2] B.L. Mordike and T. Ebert: *Mater. Sci. Eng. A*, 2001, vol. 302, pp. 37–45.

[3] J. Goken, J. Bohlen, N. Hort, D. Letzig and K.U. Kainer. *Mater. Sci. Forum* 426–432 (2003), p. 153

[4] E.F. Emley, *Principles of magnesium technology*, Pergamon Press Ltd, 1966.

[5] V.M. Segal, *Mater. Sci. Eng. A*, 197(1995), p. 157.

[6] R.Z. Valiev, A.V. Korznikov and R.R. Mulyukov, *Mater. Sci. Eng. A*, 186 (1993), p.141.

[7] Y. Saito, N. Tsuji, H. Utsunomiya, T. Sakai, R.G. Hong, *Scripta Materialia*, 9(1998), 1221-1227.

[8] R.B. Figueiredo and T.G. Langdon, Terence G. *Mater. Sci. Eng. A*, 430(2006), 151-156.

[9] X. Gong, S.B. Kang, S. Li and J.H. Cho, *Materials & Design*, 30(2009) 3345-50.

[10] J. Lin, Q. Wang, L. Peng; T. Peng, *Materials Transactions*, 49(2008), p 1021-4.

[11] H. Utsunomiya, K. Izumi, and T. Sakai, T. Mukai, *Journal of Physics: Conference Series*, 165(2009), 120-126

[12] S.R. Agnew, J.A. Horton, T.M. Lillo and D.W. Brown, *Scr. Mater.* 50 (2004), p. 377.

[13] Q. Yang and A.K. Ghosh, *Acta Materialia*, 54 (2006), 5159-5170.

[14] Li X. , A.K. Ghosh and R. Decker, *Magnesium Technology 2007*, p 221-226

[15] J.H. Cho1a, Y.M. Jin, H.W. Kim, S. B. Kang, *Materials Science Forum*,558-559 (2007) ,159-164.

[16] L.Sturkey, J.B. Clark: *J. Inst. Met.*, 88(1959-60), 177-181.

[17] J.B. Clark: *Acta Metall.*, 13 (1965), 1281-1289.

[18] S Kleiner, P.J Uggowitzer, *Mater. Sci. Eng. A*, 379 (2004) 258–263.

[19] S.R. Agnew, P. Mehrotra, T.M. Lillo b, G.M. Stoica , P.K. Liaw , *Acta Materialia* 53 (2005) 3135–3146.

[20] C.M. Sellars, *Int. Symp. on Metallury and Materials Science,* ed. N. Hansen, D. J. Jensen, T. Leffers and B. Ralph (1986), 167-187.

[21] D. Ponge and G. Gottstein: *Acta Mater.*, 46(1998), 69-80.

[22] M.H. Yoo, J.K. Lee, *Philos. Mag. A* 63 (1991) 987.

[23] E.O. Hall, *Proceedings of the Physical Society*. Section B, 64 (1951), 747-753.

[24] N.J. Petch, *Iron and Steel Institute,* 174 (1953), 25-28.

[25] N. Ono, R. Nowak and S. Miura, *Mater. Lett.* 58 (2004), p. 39.

[26] J.S. Chan and J.G. Byrne, *J. Mater. Sci.* 4 (1969), p. 861.

[27] Nie, *Scr. Mater.* 48 (2003), p. 1009

[28] H.J. Frost and M.F. Ashby, *Deformation-Mechanism Maps* (1982) p. 44.

[29] C.H. Cáceres and P. Lukáč, *Philos. Mag.* 88 (2008), p. 977.

[30] M.R. Barnett, M.D. Nave and C.J. Bettles, *Mater. Sci. Eng. A*,, 2004 (386), 205-211

[31] E.W. Kelley and W.F. Hosford Jr., *Trans. Metall. Soc. AIME* 242 (1968), p. 654.

[32] *Metals Handbook* (1973) 8th ed. vol. 8. ASM, Metals Park, Ohio.

[33] W.J. Kim, H.G. Jeong and H.T. Jeong , *Scripta Materialia,* 2009 (61),1040-1043.

CHAPTER 3

MICROSTRUCTURE AND TENSILE BEHAVIOR OF HIGH STRENGTH ZK60 MAGNESIUM PREPARED BY FRICTION STIR PROCESSING

Abstract

In this work we investigated effect of friction stir processing (FSP) to partial depths followed by warm pressing on an as-extruded ZK60 Mg plate. The microstructure, texture and resulting mechanical properties are reported here. FSP processed material had a layered microstructure and three distinct microstructures associated with stirred, transition and core region were identified. Multi-pass FSP to partial depths on top and bottom plate surfaces, followed by pressing at 200^{o}C created 0.8 μm ultrafine throughout the stirred region (55% volume fraction). The transition region (~10% volume fraction), showed extensively sheared coarse grains distributed in a matrix of finer grains. However, the core region (35% volume fraction) showed extensive twinning inside coarse grains, in an over all bimodal microstructure reminiscent of extrusion. The processed Mg with a strong basal texture exhibited high yield strength (>300 MPa) and retention of adequate tensile ductility (> 10%). The enhanced mechanical properties of processed Mg are believed to be highly influenced by the layered microstructure, finer precipitates and strong basal texture.

3.1 Introduction

In light weight structural applications specific strength is the most important material selection criterion. Mg is a natural candidate because it is 33% lighter than aluminum and 75% lighter than steel [1]. Mg and its alloys generally exhibit high specific stiffness and strength at room temperature [2]. Also, Mg alloys due to their hcp crystal structure exhibit low room temperature ductility and formability [3]. To date, most of Mg products are fabricated by casting and there are very few Mg products formed by forging, rolling, or extrusion etc. in fabrication of Mg products. Development of high strength Mg alloys with enhanced ductility is therefore imperative to fabricate a variety of light weight Mg products to increase the consumption of Mg alloys.

Earlier studies on the metallic alloys have demonstrated that grain refinement and control of precipitation attained by thermo-mechanical processing can significantly enhance strength and ductility [4-6]. Mg alloys have a limited number of independent slip systems; so, texture also strongly influences strength and ductility. Some established techniques for thermo-mechanical processing by severe plastic deformation of Mg alloys were listed in Refs. [7,8,9]. The most effective method of improving ductility of Mg alloys is through formation of textures with high Schmid factors for basal slip [10-12]. For example, Equal Channel Angular Pressing (ECAP) of AZ31 and AZ61 resulted in remarkably improved tensile elongations of 45–55% [10,11]. This is in sharp contrast to body-centered cubic (bcc) and face-centered cubic (fcc) metallic alloys with abundant slip systems at room temperature, where a considerable drop in ductility after ECAP is mostly due to the significantly reduced-work hardening ability [13]. However, when it comes to strengthening in Mg alloys, due to large Taylor factors, grain-size strengthening

effect is dominant over any other strengthening mechanism. This is also true when Mg is compared with bcc or fcc crystal structure metals. The ECAP process is also effective in refining the microstructure of Mg alloys, as in other metals, but strength is often decreased [4, 13-18]. This is attributed to the texture-softening effect being dominant over the grain-size strengthening effect in the typical range of grain sizes (1–3 μm) obtained by thermomechanical processing. For this reason, it is hard to simultaneously obtain high strength and high ductility in Mg alloys using ECAP, ARB or ECAR techniques [10,19-21]. In this work we have applied friction stir processing followed by warm flattening to an as-extruded ZK60 Mg alloy to refine its grain structure and achieve superior mechanical properties.

3.1.1 Friction Stir Processing

Friction-stir processing (FSP) is an emerging severe plastic deformation technology that is based on friction stir welding (FSW). Friction stir welding is a solid state metal joining process which was invented at The Welding Institute (TWI) in 1991 [22]. However, instead of joining FSP is exclusively used for microstructure modification. Several studies on cast alloys have shown that FSP refines grains and eliminates casting defects; thereby improving strength and ductility. Some other unique features of friction stirring include low amount of local heat generation, high strain rate intense plastic flow of material and creation of fine grains with random misorientation of grain boundaries in stirred region. Successful grain refinement of Mg-based alloy by FSP down to 1–5 μm has been widely reported recently [22-31]. In our previous work on thixomolded AM60 Mg we showed that partial depth friction stir processing improves casting defects, breaks down and disperses oxide particles, reduces gas porosity and

enhances warm formability by creating homogenous fine grain wrought microstructure [7]. The aim of the present study is to investigate the effect of partial depth FSP on the microstructure and texture of extruded ZK60 magnesium alloy. Room temperature mechanical properties of FSP processed and warm pressed alloy are also presented. A brief comparison is made with ultrafine grained ZK60 Mg alloy prepared by ABRC processing taken from Ref. [8].

3.2 Experimental

3.2.1 Materials

The ZK60A Mg alloy in T5 condition was received in the form of 19 mm thick extruded flat bar from Timminco Ltd., USA. The nominal alloy composition range is given in Table. 1.

3.2.2 Friction stir processing

Severe deformation was imparted to extruded ZK60 Mg plate by friction stir processing followed by warm pressing. Prior to friction stir processing, a 100 mm long, 80 mm wide and 9.5 mm thick work-piece was machined from extruded ZK60 plate by wire-EDM. Friction stir processing to partial depth was performed by inserting a rotating threaded pin into the top and bottom surfaces of the work-piece. A schematic illustration of friction stir processing is shown in Fig. 1. Fig. 1(b) shows stirred zone, heat-affected zone (HAZ) and weld nugget, typically observed in FSW. Fig. 1(c) shows how the retreating side of a FSP pass was overlapped by advancing side of the following pass in the present processing. In this manner, a total of 20 overlapping FSP passes were carried out on the work-piece. Therefore, the processed region was essentially a collection of advancing sides (Fig.1 (d)). In present study, FSP was performed by a Fadal milling

machine using a friction stir tool machined from H13 tool steel, heat-treated to a hardness of 52–55 Rc. The FSP tool consisted of a 13.8 mm diameter shoulder and a 3 mm long threaded pin. A tool rotation speed of 3000 rpm and a linear speed of 127 mm / min were maintained through out FSP. The FSP tool was titled by 3^{o} from the work-piece normal. In this work, FSP direction on top and bottom surfaces was parallel to extrusion direction of the work-piece.

Flattening of FSP processed work-piece with rough surface was carried out by pressing at 200^{o}C in 10-15% thickness reduction steps until a sheet of ~ 1 mm uniform thickness was obtained.

3.2.3 Aging treatments

In order to determine the optimal aging conditions of deformation processed material, low temperature aging treatments were performed at 110°C, 150°C and 200°C for 5, 10 and 24 hours. The aging treatments were carried out in air inside a Lindberg box electric furnace.

3.2.4 Microstructure characterization

The microstructural examination was done on the as-extruded, FSP processed, and warm pressed ZK60 Mg alloys. The as-extruded samples were sectioned in a plane containing the normal direction and extrusion direction. FSP processed samples were sectioned in a plane parallel to the plate normal direction The metallographic specimens were cold mounted in self-curing resin, fine ground and mechanically polished and were later etched with acetic-picral solution. The acetic-picral solution contains 4.2 g picric acid, 70 ml ethanol, 10 ml acetic acid and 10 ml distilled water. Cross-sectional microstructures of the specimens were examined using optical, scanning electron and

transmission electron microscopes. A Philips XL30-FEG SEM was employed to observe the very fine microstructure at higher magnifications. The operating voltage was 20-30KeV. The grain and particle size was measured from micrographs by an image processing and analysis software ImageJ using a volume based approximation [1]. For most of the samples, at least five photos from different locations were taken and analyzed to obtain statistical reliability.

3.2.5 Texture measurement

Crystallographic texture measurements were made on the plate/sheet plane using a Rigaku D/MAX-B rotating anode X-ray diffractometer using Cu Ka radiation at 40 kV and 100 mA. Pole figure measurements were made on the extrusion direction (ED) and transverse direction (TD) plane for as-extruded and friction stir processed plus warm pressed samples to investigate textural evolution. The XRD sample for core region was prepared by acid thinning FSP plus pressed sample to the middle of core region. Standard theta-2theta scans were run to obtain the exact positions of the Bragg peaks for the planes of interest prior to pole figures measurement. The Schulz reflection method was employed with sample. tilt from 15^{o} up to 90^{o} and azimuthal steps of 5° over the entire 360°. Corrections for defocusing of the peak and background intensities were made by experimentally measuring pole figures from a fine grained random sample and developing a correction curve. Complete Pole figures were obtained for {0002}, {1010} and {1011} from the experimental pole figure data using the Harmonic method of the Preferred Orientation Package of Los Alamos (popLA) [28].

3.2.6 Mechanical Tests

To determine mechanical behavior of the as-received and processed materials, tension tests were performed at room temperature. In as-extruded condition 4 mm thick samples were directly machined from the mid-surface of ZK60 Mg bar. Tensile samples had a gauge section of 15 mm long x 3 mm wide. The surface of tensile specimens was polished prior to testing. Tests were conducted using a computer-controlled 5505 Instron machine. A12.7 mm gauge length extensometer attached to the gauge length was used to measure the tensile strain. Specimens were tested at a constant crosshead speed of 0.5 mm/min.

3.3 Results

3.3.1 Microstructure evolution

The typical microstructural features of as-extruded ZK60 Mg alloy in T5 condition are shown in Fig.2. They include bimodal grain structure with distributed bands of 13 μm fine recrystallized grains and 300 μm coarse grains. It can be seen that there is considerable variation in microstructure from one region to another and despite the higher magnification in Fig.2 (b); structure appears similar as in Fig.2 (a). The coarse island shaped grains are elongated in the extrusion direction and make up almost 34% volume fraction of the microstructure. They are believed to be solid-solution deficient in zinc and zirconium and have specific orientation which makes them more resistant to hot working [22]. It should be noted that precipitates formed during aging are irresolvable by optical microscopy even in artificially aged T5 condition.

A low magnification photo comprising of a collage of many micrographs for partial depth FSP processed ZK60 Mg is shown in Fig. 2. As FSP tool pin partially

penetrates the depth of work-piece from both surfaces of sheet, sheet thickness can be divided in three distinct regions. The stirred region, transition region and the heat affected core region have been identified and marked in Fig.2. The resulting microstructural evolution is complicated; therefore we only focused on microstructural evolution in above mentioned regions of interest. FSP results in complete dispersion and fragmentation of grains in the stirred zones. The depth of stirred zone corresponds to FSP pin length. Intense plastic deformation and frictional heating in stirred and transition region results in breaking-up and dispersing precipitate particles and most of them are dissolved into the magnesium matrix. A bimodal grain structure similar to the extruded ZK60 Mg is retained in the core region. In the core-region friction heating causes solutionizing. The general features of FSP microstructure are consistent with earlier reported findings for Mg alloys [15, 16, and 19].

The microstructures for different regions of FSP processed and warm pressed ~1 mm thick ZK60 Mg sheet with strain $\varepsilon = 2.2$ at $200^{o}C$ are shown in Fig. 4 through 7. Microstructure of stirred region is shown in Fig.4. It consists of partially recrystallized grains with ~ 0.85 μm ultrafine grain size. A higher magnification view in Fig.4 (b) shows some precipitates inside ultrafine grains with jagged grain boundries. Microstructure of transition region between root of the tool pin and base material after warm compression is shown in Fig.5. It consists of 5-10 μm fragmented coarse grains in a matrix of ~1 μm fine grains. Microstructure of core region after warm compression is shown in Fig.6. In Fig.6 (a) longitudinal view shows bimodal microstructure with 2-5 μm fine grains and 100 μm coarse grains. In Fig.6 (b), microstructure shows a large number of parallel twins in coarse grains. This novel layered structure with UFG microstructure

stirred zone and bimodal microstructure core-region may provide a suitable combination of strength and ductility. Low temperature aging was found to be more beneficial in achieving precipitation hardening in UFG Mg prepared by ABRC. Microstructure of stirred zone before and after aging at 110^{o}C for 10 hrs is shown in Fig.7. The stirred zone after warm pressing does not indicate presence of precipitates. It shows precipitation of fine and uniformly distributed β_1' precipitates. A comprehensive TEM analysis to study the morphology and orientation of precipitates and their effect on hardening in UFG Mg will be presented in future papers.

3.3.2 Texture:

Crystallographic textures of ZK60 Mg in T5 temper are shown in Fig. 7 (a) by complete pole figures for {0002}, {1010} and {1011} planes. The basal poles have highest intensity of ~6 multiples of a random distribution (MRD) and distant peaks are observed in the TD. The basal and prism pole figures reveal that in as-extruded condition grains with basal {0002} and prismatic {1010} planes lie parallel to the sheet plane with their c-axis perpendicular to the ED. However the intensity of prism poles is less and the basal poles with high intensity dominate. Therefore, the texture of as-extruded ZK60 Mg alloy in T5 condition can be characterized as basal texture parallel to sheet plane with some tilting of the basal poles in the TD. Distribution of basal poles orthogonal to extrusion direction after warm- extrusion has also been extensively documented in other magnesium alloys [23, 24].

The pole figures for the middle of stirred region after warm pressing with strain ε = 2.2 at 200^{o}C is shown in Fig. 7(b). The {0002} pole figure shows that the density of basal poles is distributed around ND with the maximum located at ND. The highest

intensity of basal poles is ~18 MRD. There is some apparent spread of the basal poles along the FSP direction i.e. ED. The pole figures for core region after warm pressing with strain $\varepsilon = 2.2$ at 200^{o}C is shown in Fig. 7(c). The maximum intensity of basal poles is to ~ 10 MRD. The {0002} pole figure shows that the density of basal poles is evenly distributed and maximum intensity is located at ND. There is an apparent spread in the TD which is typical of warm pressed samples. Overall FSP processing followed by warm pressing leads to the formation of strong basal texture with spreads along different directions in stirred and core regions. Pole figures measured for FSP processed and warm pressed ZK60 Mg samples after aging treatments show very little texture changes and are therefore not presented here.

3.3.3 Room temperature tensile tests

Room temperature engineering stress strain for as-extruded and FSP + warm pressed are presented in Fig.8. Data for and UFG Zk60 Mg prepared by ABRC processing is also included for comparison. Values of yield stress (YS), ultimate tensile strength (UTS) and strain-to-failure are summarized in Table. 2 The as-extruded T5 aged samples exhibits moderate strength and ductility. As shown in Fig.8, in as-extruded condition extrusion direction (ED) tension specimens exhibits 237 MPa yield strength in ED with tensile elongation of ~18%. In case of processed material, the following can be inferred from the plot and the table. First, the FSP + warm pressed material with layered microstructure exhibits high yield strength. Second, tensile elongation was less than extruded condition which maybe related to a strain softening effect. Third, aging treatment at 110^{o}C for 10 hrs significantly improved the strength of processed material

and restored some ductility. However, aging treatment carried out at the conventional T5 temperature lead to decrease in yield strength but elongation to failure increased.

Over all, processed-Mg with the layered microstructure exhibited the highest strength (YS = 345 MPa, UTS = 390 MPa) and superior tensile elongation of 12% after aging. These results are comparable to UFG ZK60 Mg prepared by ABRC processing however, some amount of strain hardening was observed in ABRC samples. It is important to note that the current ductility improvement after aging was attained simultaneously with the strength improvement.

3.4 Discussion

3.4.1 Microstructural evolution

In our previous work, we have investigated the effect of friction stir processing on warm formability of thixomolded AM60 Mg. It is very well known that during friction stir processing, rotational and translation speeds of tool have significant effects, on the grain size evolution in stirred zone. Several studies have shown that during FSP, shear happens parallel to the surface of the tool pin and basal poles align themselves around the surface of the pin. Therefore, deformation happens mainly by basal slip. In multistep processing, accumulation of frictional heat may relax the CRSS of non-basal slip systems. Therefore, some prism slip maybe expected while, at the same very little twinning deformation is expected. Dynamic recrystallization due to frictional heating and plastic strain in stir zones of the friction stir processed Al alloys is widely reported [33-35]. Mg alloys experience dynamic recrystallization more readily than Al alloys, because the recrystallization temperature of Mg alloys is about 220^{o}C, which is lower than that of most Al alloys [9]. Since the peak temperature of the stir zone is higher than the

recrystallization temperature, dynamic recrystallization should occur in the stir zone during FSP stirring, along with breakup/dissolution of precipitate particles. A much finer microstructure evolved in the stirred region of ZK60 Mg compared to FSP processed AM60 Mg [7]. This may be also be explained on the basis of higher dynamic recrystallization temperature for ZK60 Mg and the presence of precipitate particles. A UFG structure was much easily achieved in precipitate-hardened ZK60 Mg alloys due to the effective grain boundary pining effect [25-27]. The deformation imparted during flattening step further refines the grain size in stirred region.

Significant microstructural changes take place in the core region during the flattening steps. Earlier investigations have shown that compression parallel to c-axis results in $\{10\overline{1}1\}$ banding, consisting of $\{10\overline{1}1\}$ twinning followed by $\{10\overline{1}2\}$ retwinning and basal slip within the doubly twinned band. At the beginning stage of deformation, twinning takes place within those grains unfavorably oriented for basal slip. Stress concentration at grain boundary resulting from incompatible plastic strain can be relieved by twinning [9]. Higher strain level of > 2 true strain may require the activation of non-basal slip systems. The twin angle was found to increase with strain, which indicates the rotation of twins with further compression. This characteristic was also has been observed by other investigators [36]. It is believed that slip occurring between the twinned areas is responsible for this effect. The large coarse grains with number of parallel twins inside them are eventually sub-divided into many units. The evolution of bimodal structure with sheared coarse grains and ultrafine grains in transition region between stirred and core region is also of significance. Its development however, is not clear at this point as the material flow between the root of the rotating tool pin and base

material is much more complicated. Since the volume fraction contribution from transition region is small, its effect on over all mechanical properties may not be that significant.

3.4.2 Texture evolution:

Several researches have shown by micro-texture measurements that during a single pass of FSP various changes take place in texture of base material. Region near surface develops a strong basal texture due to the forging effect of tool shoulder. Our discussion however will focus on stirred region. Shear plastic flow during FSP destroys the texture in the stir zone via dynamic recrystallization and results in a texture in which the basal plane normal is roughly surrounding the rotating pin surface as shown in Fig.10 [8]. A similar texture is expected to develop throughout the stirred region after multi-pass FSP. The warm pressing steps have a significant impact on texture and FSP texture is converted in to a strong basal texture. However, due to partial depth processing a textural gradient develops between stirred region and core. Both regions have a strong basal texture but basal poles were mainly distributed towards extrusion direction in stirred region and towards transverse direction in the core region.

3.4.3 Mechanical property improvement

Typically, it is difficult to improve both strength and ductility. Improvement in yield strength of fine grained alloy is often accompanied by loss in ductility and vice versa. Hexagonal metals present a more complex case due to their low symmetry and limited number of independent slip systems [38], and their strong plastic anisotropy. Because of the latter, the soft slip systems carry the bulk of the plastic strain, but the

overall strength of polycrystalline aggregates is controlled by the CRSS of the hard systems [38]. In addition, the activation of twinning at low strains [39] further complicates the overall picture as it may enhance the metal's ductility [39], and affect the flow behaviour [39-41]. The increase in yield strength in the friction stir processed and warm pressed ZK60 Mg with layered microstructure may be related to a combination of grain size and precipitation strengthening. Hall-petch equation combined with rule of mixtures may be used to estimate the yield strength by taking into account the volume fraction input from ultra-fine grain stirred region and coarse bimodal grain core region. Plastic deformation of Mg alloys at room temperature is dominated by basal slip and since β_1' precipitates are located along the [0001] direction they can effectively pin dislocation movements on basal planes and thereby restrict plane glide. The contribution from precipitation strengthening may be estimated by an Orowan equation for basal precipitates, as were previously used in Ref. [8]. Therefore size and distribution density of β_1' precipitates is a dominant factor in age-hardening of Mg-Zn alloys. Yield strength decline in samples aged at 200^{o}C may be due to some grain growth and transformation of β_1' precipitates into β_2' leading to decrease in the density of β_1' precipitates.

Strain softening was observed in the FSP condition as compared to ABRC condition where some strain hardening was observed. Strain softening was also observed in the as-extruded condition with strong basal texture. This “apparent” strain softening in layered microstructure means that softening effect of bimodal coarse grains in core region (that have similar structure as the as-extruded condition) overwhelms strain hardening provided by ultra-fine grains in stirred region. Despite the fact that stirred region occupies much larger volume of the material. Samples aged at 200^{o}C exhibit strain hardening

which leads to improvement in ductility. However, this ductility improvement comes at the expense of yield strength.

3.4.4 Efficacy of multi-step friction stir processing

It is necessary to achieve homogeneous grain refinement and distribution of precipitates in order to enhance the mechanical properties. Conventionally, a solution treatment at a higher temperature for a long time is required to dissolve second-phase particles into the magnesium matrix, and then an aging is conducted to generate fine precipitates. However, such a procedure may be time consuming; resulting in not only increased material cost but also surface oxidation and grain coarsening. It in our companion paper on processing of high strength ZK60 Mg by alternate biaxial reverse corrugated pressing we showed that significant grain refinement and homogenization can be achieved [33]. ABRC processing combined with low temperature aging for 10 hrs provides a good combination of strength and ductility. However, 6 ABRC cycles were required to achieve such properties. In comparison, use of the FSP technique results in the significant grain refinement breakup/dissolution of precipitate particles. As compared to other methods, FSP imparts severe plastic deformation in the stirred region, with a strain rate of 100 to 10^3 s^{-1} [42–44] and a strain of up to ~40 [45]. This facilitates grain refinement and solutionizing due to the significantly accelerated diffusion rate and shortened diffusion distance. Thus, large numbers of microstructural defects are introduced to accommodate the strain incompatibility, which is beneficial for grain refinement by dynamic recrystallization. In addition to the fine and equiaxed grains, the microstructure in FSP is characterized by a high fraction of high-angle boundaries. In some studies fraction of high-angle boundaries as high as 85 to 95 % has been reported

[46-47]. This ratio is significantly higher than that obtained in conventional thermo-mechanical processed Mg alloys with a typical ratio of 50 to 65 %. Because the microstructure can be controlled by changing the FSP parameters, processing depth, tool design, vertical pressure, active cooling/heating, processing direction on top and bottom surface it is likely that the mechanical properties of a metallic material can be tailor made via FSP.

3.5 Conclusions

(1) The ability of friction stir processing to produce high strength Mg alloy with multiple overlapping passes to partial depth was demonstrated in this study.

(2) Overall a layered structure comprising of three distinct microstructural regions was identified in the processed alloy.

(3) Microstructure in the stirred region nearly equiaxed and recrystallized 0.8 μm grains. Aging resulted in precipitation of fine and uniformly distributed particles. Core region in the middle showed extensive twinning in coarse grains in a largely bimodal microstructure after warm pressing.

(4) Textural evolution indicated that material flow happened mainly by basal slip during FSP and while it involved extensive $\{10\bar{1}2\}$ twinning in the core region during warm flattening.

(5) Tensile testing showed that high yield strength (> 350 MPa) with adequate ductility (elongation to failure 10%) can be achieved in extruded ZK60 Mg by FSP processing and low temperature aging.

(6) The major difference between tensile behavior of FSP processed and ABRC processed Mg was strain-softening which maybe related to bimodal coarse grain structure in the core region.

Table 3.1 Nominal Composition range of as-extruded ZK60A Mg (in wt. %)

Mg	Zn	Zr	Other impurities (total)
Balance	4.8-6.2 %	0.45%	0.30

Table 3.2 Mechanical properties of as-extruded and ABRC processed ZK60 Mg

Materials	Thickness (mm)	G.S (μm)	Y.S (MPa)	T.S (MPa)	Elongation to failure, %
ZK60-T5 (ED)	4	13	230	296	17
FSP+ warm pressed (ED)	1	13	320	373	11
FSP+ warm pressed (ED) Aged 110^{o}C/10hrs	1	2.5	345	390	12.5
FSP+ warm pressed (ED) Aged 200^{o}C/10hrs	1	2.5	272	361	17
ZK60-ABRC+Aged (D1) ε =8.0 at 150^{o}C	0.75	0.9	353	402	14

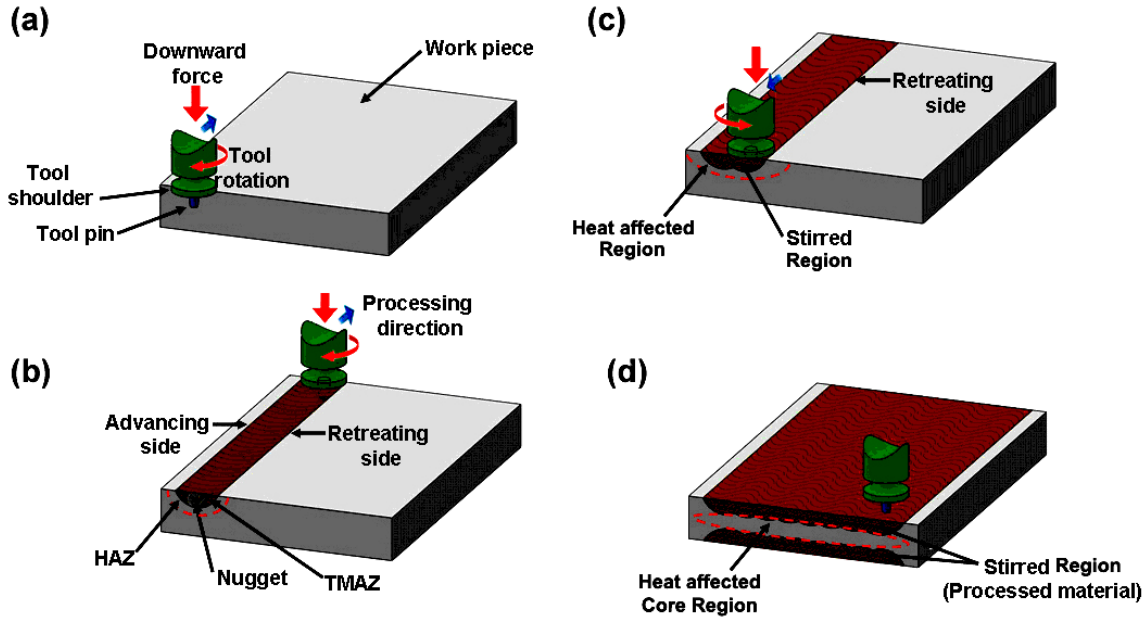

Figure 3.1 Schematic illustration shows several stages of overlapping passes for partial depth FSP, stirred region (processed material) and heat affected core region (base material) have been identified.

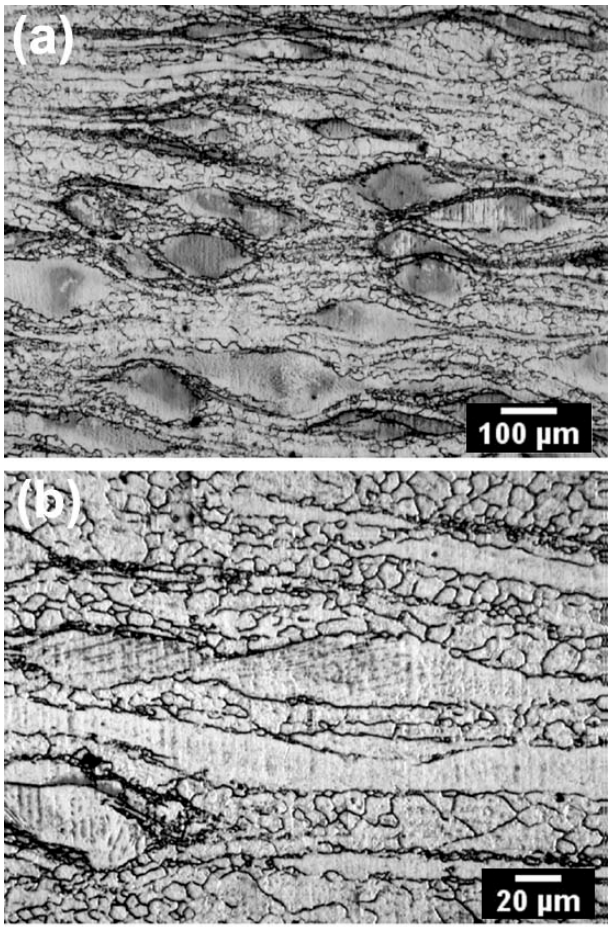

Figure 3.2 Microstructure of as-extruded ZK60 Mg artificially aged to T5 temper. In (a) longitudinal view shows bimodal microstructure with bands of small 13 µm recrystallized grains and dark, island-shaped 300 µm coarse grains elongated along the extrusion direction. Coarse grains occupy 35 % vol. fraction of the microstructure. In (b) despite the higher magnification, structure appears similar as in (a). Precipitates formed during aging are irresolvable by optical microscopy.

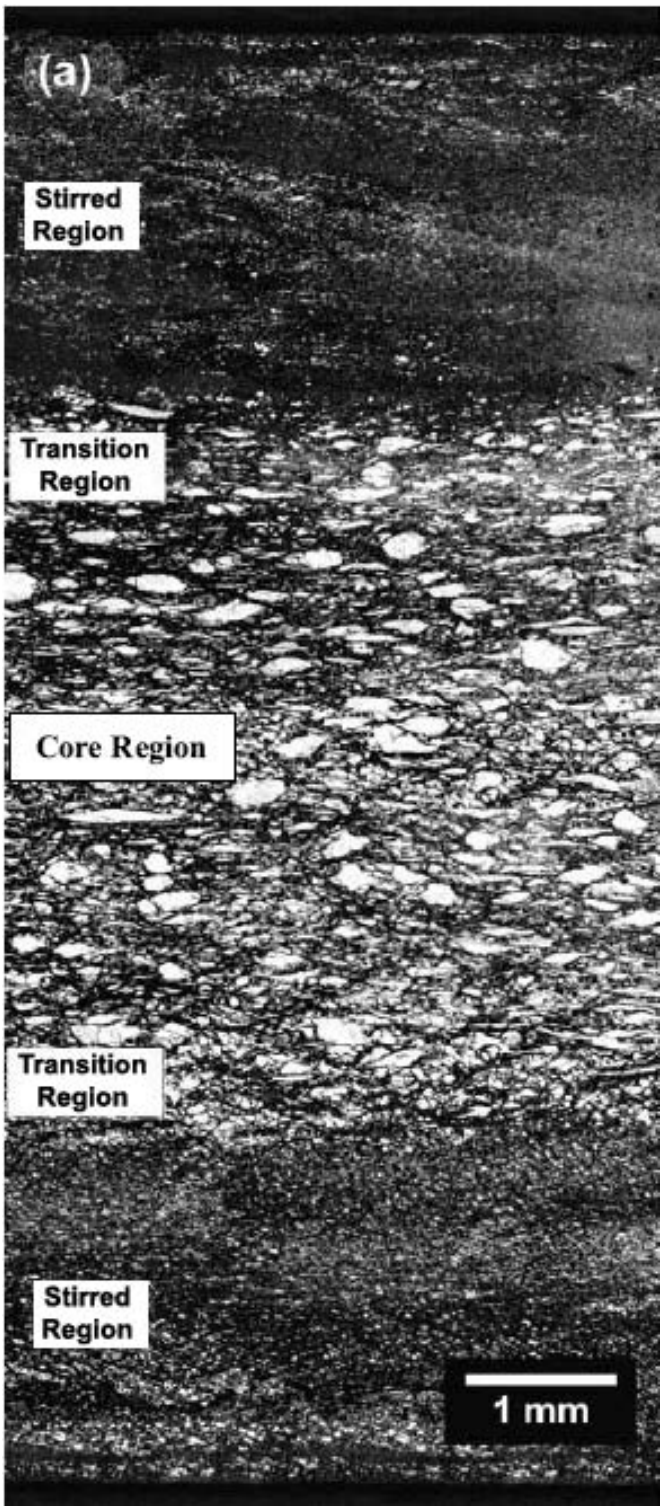

Figure 3.3 Collage of micrographs shows microstructure of friction stir processed ZK60 Mg. Multiple over-lapped FSP passes to partial depths from top and bottom surfaces creates a novel layered microstructure. Stirred region, transition region and heat affected core region have been identified.

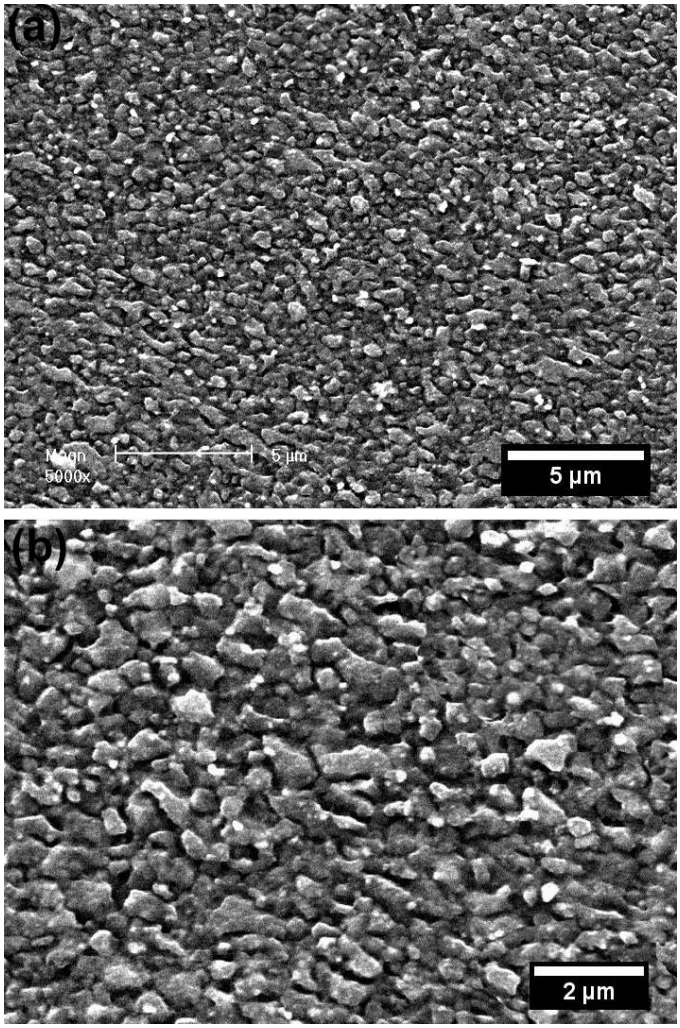

Figure 3.4 Microstructure of stirred region after warm compression at 200^{o}C with true strain $\varepsilon = 2.2$.

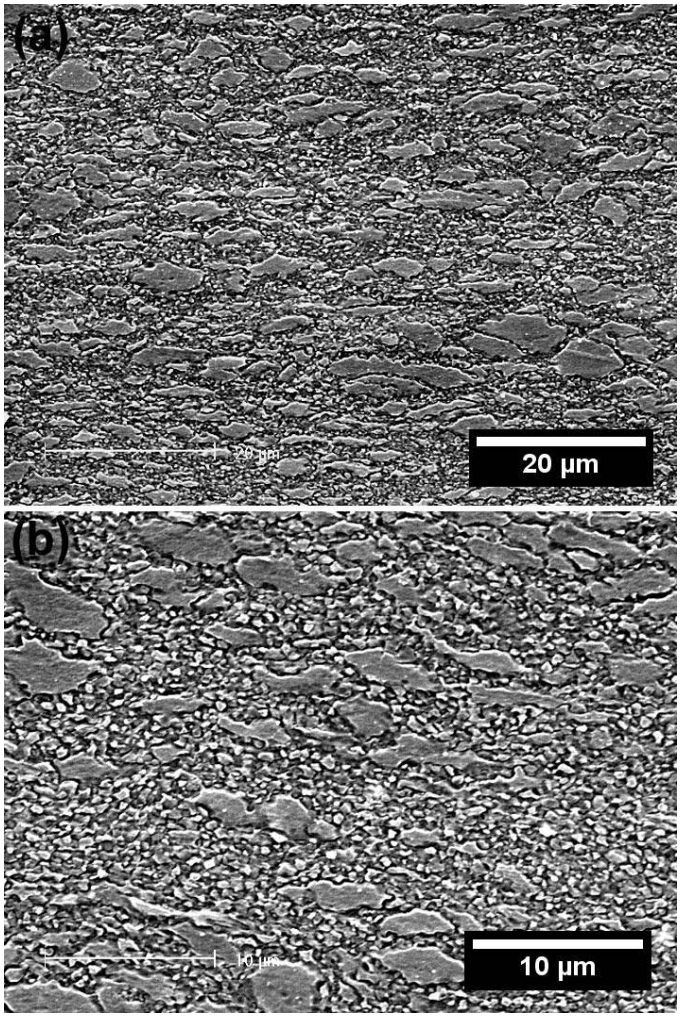

Figure 3.5 Microstructure of transition region between stirred region and core region after warm compression at 200^{o}C with strain $\varepsilon = 2.2$.

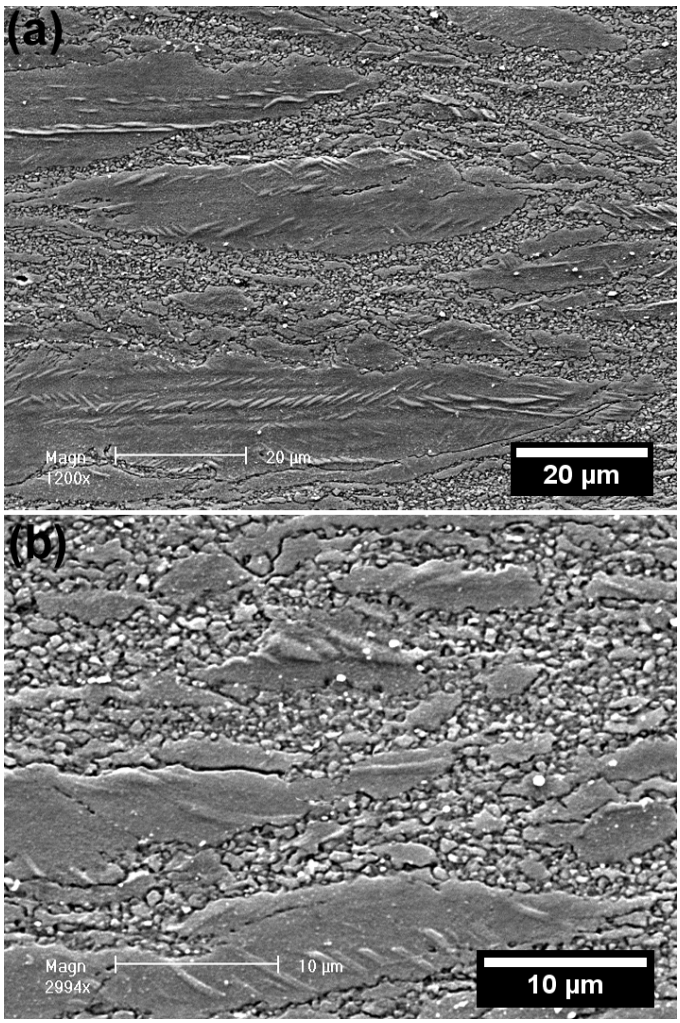

Figure 3.6 Microstructure of core region after warm compression at after warm compression with strain ε = 2.2. In (a) longitudinal view shows bimodal microstructure with 2-5 µm fine grains and 100 µm coarse grains. In (b) a large number of parallel twins are observed in coarse grains.

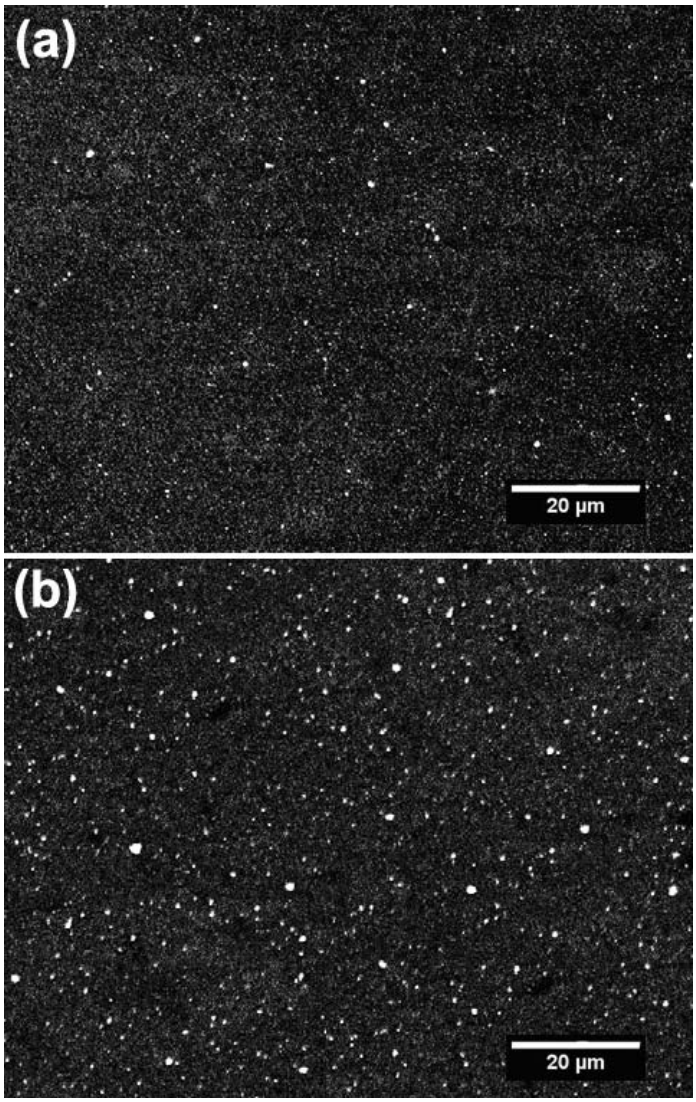

Figure 3.7 Low magnification SEM picture of stirred region in warm pressed Mg before and after being aged at 110^{o}C for 10 hrs. In (a) not many precipitates are observed. In (b) precipitation of fine and uniformly distributed β_1' particles.

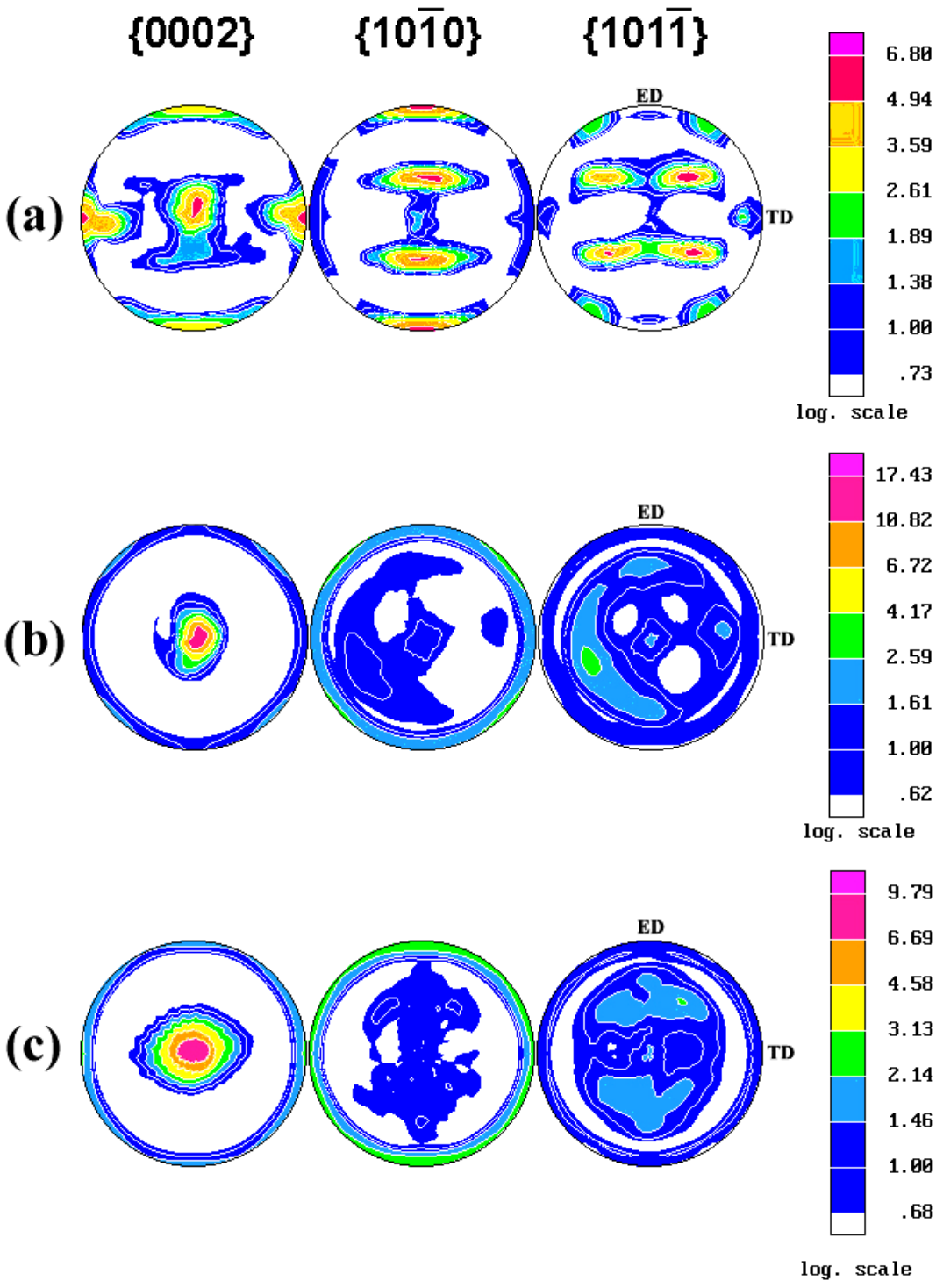

Figure 3.8 Pole figure for {0002}, {1010}, {1011}, crystallographic planes. Samples were taken for (a) as-extruded condition, warm pressed with ε = 2.2 at 200^{o}C (b) stirred region and (c) core-region.

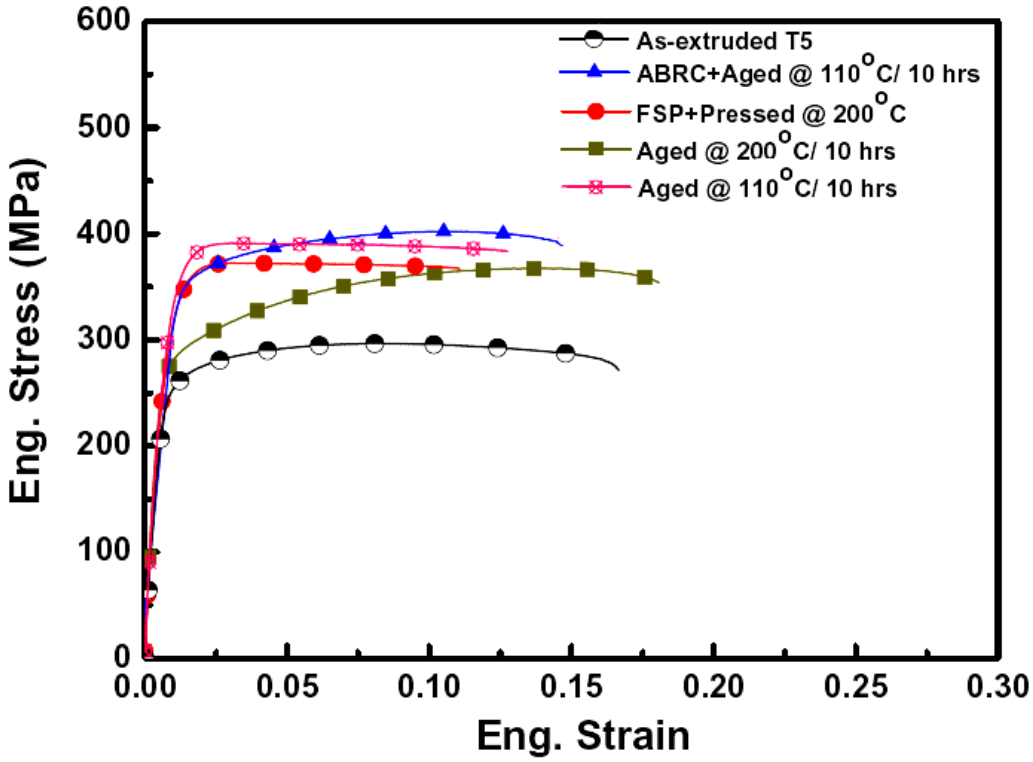

Figure 3.9 Room temperature tensile stress–strain curves for processed-Mg after different aging treatments.

3.6 References

[1] D. R. Askeland, P. P. Phule, *The Sci. and Eng. of Mater.s 5th ed.*, Thomson Canada Limited, 2006, 504, 574, 595, 597.

[2] B.L. Mordike and T. Ebert: Mater. Sci. Eng. A, 2001, vol. 302, pp. 37–45.

[3] P.G. Patridge, *Met. Rev.* 118 (1967), p. 169.

[4] V.M. Segal, MSE. A, 197(1995), p. 157.

[5] R.Z. Valiev, A.V. Korznikov and R.R. Mulyukov, MSE. A, 186 (1993), p.141.

[6] Y. Saito, N. Tsuji, H. Utsunomiya, T. Sakai, R.G. Hong, Scripta Materialia, 9(1998), 1221-1227.

[7] B. Mansoor, S. Mukherjee, A.K. Ghosh, *Mater. Sci. Eng. A*, 512 (2009) 10–18

[8] B. Mansoor, *Chapter 2, PhD thesis*, University of Michigan, Ann Arbor, 2010.

[9] Q. Yang and A.K. Ghosh, *Acta Materialia*, 54 (2006), 5147-5158.

[10] W.J. Kim, S.I. Hong, H.T. Jeong and J.D. Lee, *Acta Mater.* 51 (2003), p. 3293.

[11] J. Koike, T. Kobayashi, T. Mukai, H. Watanabe, M. Suzuki, K. Maruyama and K. Higashi, *Acta Mater.* 51 (2003), p. 2055.

[12] W.J. Kim and H.T. Jeong, *Mater. Trans.* 46 (2005), p. 251.

[13] Y.T. Zhu and T.G. Langdon, *JOM* 56 (2004), p. 58.

[14] W.J. Kim, S.I. Hong, Y.S. Kim, S.H. Min, H.T. Jeong and J.D. Lee, *Acta Mater.* 51 (2003), p. 3293.

[15] J. Koike, T. Kobayashi, T. Mukai, H. Watanabe, M. Suzuki, K. Maruyama and K. Higashi, *Acta Mater.* 51 (2003), p. 2055.

[16] W.J. Kim and H.T. Jeong, *Mater. Trans.* 46 (2005), p. 251.

[18] S.R. Agnew, J.A. Horton, T.M. Lillo and D.W. Brown, *Scr. Mater.* 50 (2004), p. 377.

[19] M.T. Pérez-Prado, J.A. del Valle and O.A. Ruano, *Mater. Lett.* 59 (2005), p. 3299.

[20] M.Y. Zhan, Y.Y. Li, W.P. Chen and W.D. Chen, *J. Mater. Sci.* 42 (2007), p. 9256.

[21] W.J. Kim, S.J. Yoo, Z.H. Chen and H.T. Jeong, *Scr. Mater.* 60 (2009), p. 897

[22] A.H. Feng and Z.Y. Ma, *Scripta Mater.* 56 (2007), p. 397

[23] Y. Morisada, H. Fujii, T. Nagaoka and M. Fukusumi, *Mater. Sci. Eng. A* 419 (2006), p. 344

[24] Y. Morisada, H. Fujii, T. Nagaoka and M. Fukusumi, *Scripta Mater.* 55 (2006), p. 1067.

[25] C.J. Lee and J.C. Huang, *Mater. Trans.* 47 (2006), p. 2773

[26] C.J. Lee, J.C. Huang and P.J. Hsieh, *Scripta Mater.* 54 (2006), p. 1415.

[27] C.I. Chang, Y.N. Wang, H.R. Pei, C.J. Lee and J.C. Huang, *Mater. Trans.* 47 (2006), p. 2942.
[28]F.Y. Hung, C.C. Shih, L.H. Chen and T.S. Lui, *J. Alloys Compd.* 428 (2007), p. 106.

[29] J.A. Esparza, W.C. Davis, E.A. Trillo and L.E. Murr, *J. Mater. Sci. Lett.* 21 (2002), p. 917.
[30] C.I. Chang, C.J. Lee and J.C. Huang, *Scripta Mater.* 51 (2004), p. 509.

[31] W. Woo, H. Choo, D.W. Brown, P.K. Liaw and Z. Feng, *Scripta Mater.* 54 (2006), p. 1859.

[32] R.S. Mishra and M.W. Mahoney, *Mater. Sci. Forum* 357–359 (2001), p. 507.

[33] C.G. Rhodes, M.W. Mahoney, W.H. Bingel, R.A. Spurling and C.C. Bampton, *Scripta Mater.* 36 (1997), p. 69.

[34] L.E. Murr, G. Liu and J.C. McClure, *J. Mater. Sci. Lett.* 16 (1997), p. 1801.

[35] J.-Q. Su, T.W. Nelson, R. Mishra and M. Mahoney, *Acta Mater.* 51 (2003), p. 713.

[36] Li X. , A.K. Ghosh and R. Decker, *Magnesium Technology 2007*, p 221-226.

[38] U.F. Kocks and H. Mecking, *Prog. Mater. Sci.* 48 (2003), p. 171.

[39]U.F. Kocks and D.G. Westlake, *Trans. AIME* 239 (1967), p. 1107.

[40] J. Koike, *Proceeding of the Winter TMS Meeting*, TMS, Charlotte, NC (2004).

[41] M.H. Yoo, *Metall. Trans.* 12A (1981), p. 409

[42] C.I. Chang, C.J. Lee, J.C. Huang: *Scripta Mater*., 2004, vol. 51, pp. 509–14.

[43] B. Askari, S. Silling, B. London, M. Mahoney: *JOM*, 2004, vol. 56, pp. 245–46.

[44] R.L. Goetz and K.V. Jata: in *Friction Stir Welding and Processing*, TMS, Warrendale, PA, 2001, pp. 35–42.

[45] P. Heurtier, C. Desrayaud, F. Montheillet: *Mater. Sci. Forum*, 2002, vols. 396–402, pp. 1537–42.

[46] R.S. Mishra, M.W. Mahoney: *Mater. Sci. Forum*, 2001, vols. 357–359, pp. 507–12.

[47] I. Charit, R.S. Mishra: *Mater. Sci. Eng., A*, 2003, vol. A359, pp. 290–96.

CHAPTER 4

MICROSTRUCTURE AND POROSITY IN THIXOMOLDED MAGNESIUM ALLOYS AND MINIMIZING ADVERSE EFFECTS ON FORMABILITY

Abstract

The purpose of this research was to investigate possible changes in warm formability of thixomolded Mg alloys by applying severe deformation processing. The microstructure of as-thixomolded magnesium alloys can be complex, as it can contain a variety of constituents such as $Mg_{17}Al_{12}$ intermetallic particles, shrinkage and gas porosity, as well as internal oxide films and entrapped residues. It was found in this research that these dissolved gases and heterogeneities adversely influence warm formability of the molded sheet, and contribute to variability in strength and ductility. Furthermore, these inherent heterogeneities affect fracture properties of thixomolded alloys when they are hot rolled into sheet products. Heat treatments, hot rolling and friction stir processing experiments were carried out to alter microstructure of thixomolded AM60 Mg (Mg-6%Al) plate provided by a commercial supplier. The macrostructure and microstructure resulting after these experiments demonstrated that for a given lot of thixomolded Mg plate, considerable changes in the microstructure, porosity and warm formability are caused by stirring and severe deformation processing approach.

The knowledge gained from this study could benefit thixomolding community, as well as wrought Mg applications in regard to factors that affect formability.

4.1 Introduction

Magnesium alloys hold great potential for use in aircraft, automotive and electronic industry. Due to low density, high specific strength and the ability of re-cycling, there is great interest in these alloys [1-3]. However Mg alloys, due to their hexagonal closed packed crystal structure and limited number of independent slip systems, exhibit poor formability at room temperature [4, 5]. At higher temperatures activation of additional slip systems assist flow and consequently enhancement in formability is seen [6]. More than 90% of Mg automotive parts are still produced by die casting but there is considerable interest at this time to take advantage of elevated temperature formability of magnesium. Several earlier investigations demonstrated that grain refinement could enhance strength and ductility at room temperature as well as make alloys superplastic under high strain rates at elevated temperatures [7-9]. Rapid forming at low levels of elevated temperatures ($\leq 300^{o}$C) is desirable because oxidation problem for Mg at higher temperatures complicates manufacturing, adding to cleaning cost for parts [10-12]. Nevertheless, Mg alloy sheets are of considerable interest at this time [13].

Thixomolded magnesium alloy plate offers fine grained cast structure, potentially a favorable starting point to convert cast microstructure into wrought microstructure to improve formability for large plastic deformation. Thixomolding® is a semi-solid metal molding technique that combines conventional die casting with plastics injection molding for production of near-net-shape parts from magnesium alloys rapidly [14-15]. Compared

with traditional casting techniques, thixomolding combines slurry making and component production into a single-step process.

4.1.1 Thixomolding process and its speed

This process is marked by extreme rapid melting, mixing and injection of material for high throughput of parts. Mg alloy granules are introduced as feedstock in a barrel fitted with auger. The high affinity of magnesium for oxygen makes Mg alloy granules prone to surface oxide formation [16], which is exacerbated by the large surface area/volume of granule feedstock. Inside the barrel, the Mg feedstock is heated to high temperatures while maintaining pressure and shear on it. The oxides already present on feedstock can grow in thickness under high thixomolding temperatures. A large fraction of the material eventually becomes liquid mixed with a portion of primary solid particles under high shear rate of mixing. The semi-solid slurry is then injected into a preheated metal mold to make a net shape part.

Removal of moisture from a pack of granules or powder under vacuum is known to require very long time. As found in refs. 17 and 18 large amounts of hydroxyl species can be contained in light metals e.g. in aluminum powder metallurgy work where long degassing is absolutely necessary for high quality low porosity products [19, 20]. In a powder metal mass, the stochastic collision of gas molecules attempting to exit from the barrel of a thixomolder under superimposed pressure is nearly impossible in a rapidly executed process. The hydrated oxide layer in magnesium granules cannot be fully released as augur compresses granules and closes the release path. Moisture reacting with Al or Mg can form Al_2O_3 amorphous film or MgO crystallites releasing hydrogen [18]. In conventional melting of alloys, fluxing permits dross to float and be removed. This slow

process is not permitted during rapid thixomolding. The rapidity of processing and melting operation in thixomolding, followed by rapid freezing on the mold does not permit full removal of gases or oxide, and this is further exacerbated when melt streams mix within the mold, thereby entrapping air or gases. Literature shows that the oxygen content in the final thixomolded finished parts is approximately an order of magnitude higher than that in the starting initial feedstock for thixomolding process [21, 22].

In addition to porosity and oxides, thixomolded AM60 Mg alloy microstructure typically consists of 3% to 15% primary solid fraction of α-Mg globules (30μm average size) in a matrix of α-Mg grains (8-10 μm average size) surrounded by eutectic mixture consisting α-Mg and β-$Mg_{17}Al_{12}$ intermetallics (average size of 1–2 μm). Strain incompatibility between the intermetallic particles (bcc) and α-phase (hcp) leads to brittleness of the interface between them [23]. It is thought that formability of these materials can be enhanced by breaking interfacial intermetallics and removing porosity to obtain improved mechanical property sheets.

4.1.2 Objectives of this research

The objective of this study was to examine the interaction of porosity and microstructural inhomogeneity issues mentioned above with deformation processing imparted to the alloy. Thixomolded AM60 was selected for secondary processing because Thixomat Inc. has extensive experience in producing this alloy. To understand the effects of elevated temperature deformation it was decided that the effect of temperature alone on the alloy be first examined to verify the hypothesis that dissolved gases may remain within material above and beyond what is visible in the macro and micro cross-section of molded alloy plates. The temperature of these thermal treatments were intentionally

selected to be at a higher level (~ 400°C) than one may generally consider for hot rolling molded plate to verify gas evolution during high temperature processing. Severe deformation of thixomolded alloy was pursued to disperse the intermetallic constituents and remove gas induced porosity. This was done by Friction Stir Processing (FSP), a high strain rate deformation process based on Friction Stir Welding (FSW) process. It is often used to modify, homogenize and refine heterogeneous microstructures in solid state [24]. Many recent studies have been reported on FSW/FSP of magnesium alloys [25-30]. FSP involves plunging a rapidly rotating tool with a profiled pin and larger diameter shoulder, beneath material surface and then traversing the tool across. Forging action of the tool shoulder provides a constraint to upward material flow. The frictional heating and intense plastic deformation due to mechanical stirring causes material flow around tool pin and fragments grains and grain boundaries. This leads to formation of dynamically recrstallized and equiaxed fine grains in stirred zone. A thermo-mechanically affected zone (TMAZ) is also produced in the material by frictional heating and plastic deformation due to rubbing and forging action of tool shoulder near plate surface. Also, frictional heating could dissolve some of the intermetallic precipitate particles in heat affected base material [25, 28]. Multi-pass FSP is expected to disperse particles; refine grains and reduce porosity.

4.2 Experimental

The thixomolded alloy examined in this work is AM60 Mg, a well-established alloy produced by Thixomat Inc. for many years. The alloy was received in the form of 153 mm long x 102 mm wide and 3 mm thick plates from Thixomat Inc. Its composition is Mg-6%Al-0.38%Mn-0.11%Zn-0.04%Si (more commonly stated Mg-6%Al-0.4%Mn).

4.2.1 Hot rolling

Hot rolling experiments were carried out to create a 1 mm thick sheet from the 3 mm thick thixomolded AM60 plates in one rolling pass of approximately 60-70% thickness reduction. Before rolling, the work piece was pre-heated in a furnace at 350^{o}C for 15 mins. The rolling temperature was empirically chosen from one or two experiments. In the work presented here hot rolling was carried out on a two-high reversing with 8" dia 7" long Stanant rolling mill.

4.2.2 Heat treatment

Since porosity and second phase particles were previously identified in the alloy, it was decided to perform several heat treatments to homogenize microstructure and study the origin of pore formation, pore coalescence and blistering. The solvus temperature for this alloy is near 400^{o}C and this was selected as the heat treat temperature. The heat treatment was performed for 2 hrs. Similar heat treatment studies were performed on friction stir processed samples for comparison of porosity evolution and other microstructural features.

4.2.3 Friction stir processing

Friction stir processing to partial depth was performed on top and bottom faces of thixomolded plate by inserting a grooved (or threaded) pin into the metal rotating at 2000-3000 rpm to breakdown cast microstructure. A schematic illustration of friction stir processing is shown in Fig. 1. Fig. 1(b) shows stirred zone, heat-affected zone (HAZ) and weld nugget, typically observed in FSW. Fig. 1(c) shows that retreating side of the first FSP pass was overlapped by advancing side of the next pass. In this manner, a total of 35 overlapping FSP passes were carried out on a 153 mm long x 102 mm wide and 3

mm thick work-piece. Therefore, the processed region is essentially a collection of advancing sides (Fig. 1 (d)). In present study, FSP was performed by a Fadal milling machine using a friction stir tool machined from H13 tool steel, heat-treated to a hardness of 52–55 Rc. The FSP tool consisted of a 12.7 mm diameter shoulder and a 1.2 mm long x 2.54 mm dia threaded pin. 2-3 mins long dwell periods of shoulder rubbing were applied prior to each step to reach sufficiently high temperature (300-350^{o}C). A tool rotation speed of 3000 rpm and a linear speed of 127 mm/min were maintained through out FSP. Each time the FSP tool was moved by 1.2 mm from the pin axis to apply the overlapping FSP step. The FSP tool was titled by 3^{o} from the work-piece normal. In this work, FSP direction was parallel to extrusion direction of the work-piece.

Flattening of FSP processed sheet with rough surface was carried out by hot pressing the sheet at 350^{o}C until a sheet of uniform thickness 1.8 mm was obtained.

4.2.4 Microstructure characterization

The microstructural and porosity examination in as-molded, heat treated, rolled and friction stir processed alloys was performed by using optical and scanning electron microscopy. Metallographic specimens were cold mounted in self-curing resin, fine ground and mechanically polished and were later etched with acetic-picral solution. The acetic-picral solution contains 4.2 g picric acid, 70 ml ethanol, 10 ml acetic acid and 10 ml distilled water. A Philips XL30-FEG SEM operating at a voltage of 20-30 KeV was employed to observe very fine microstructure and for EDXS analysis.

4.2.5 Biaxial forming

Formability of as-molded and processed sheets was verified by a corrugated pressing test. The apparatus for the test includes a pair of asymmetrically corrugated dies as shown in Fig. 2 (a). This setup was previously used to impart severe deformation to wrought Mg work-piece by a process termed as Alternate Biaxial Reverse Corrugation (ABRC). The details of ABRC processing are described in Ref. [31], but in this work the corrugated dies were used to evaluate warm formability. ABRC pressing was applied to as-thixomolded and FSP processed AM60 Mg at deformation temperature of 350^{o}C.

4.3 Results and discussions

4.3.1 Microstructural characterization of as-received alloy

The typical microstructural features of thixomolded AM60 Mg are shown in Fig. 3. The microstructure can be described as equiaxed primary particles of (unmelted) α-Mg dispersed in a continuous matrix of solidified aggregate of fine secondary α-Mg and β ($Mg_{17}Al_{12}$). This microstructure corresponds to a reasonably rapid cooled liquid (~100^{o}C/s), since no long dendrites are visible. Three distinct morphologies of the primary solid particles spheroidized during thixomolding are found in the micrograph as α_p-Mg* shown in Fig. 3(a), one is essentially unmodified solid, one with rosette shape and the last is the solid particle with entrapped liquid [14]. Fig. 3(b), shows fine secondary α_s-Mg* grains surrounded by a network of eutectic component that is a mixture of α_e-Mg* film and an intermetallic compound β ($Mg_{17}Al_{12}$). The average grain

size o f α_s-Mg grains is 7.2 μm, while the eutectic intermetallics mixture distributed between the spaces of α_s-Mg grains shown in Fig 3(c) has a thickness of about 2 μm.

---

* α_p *refers to* primary solid α-Mg grains, α_s *refers to secondary fine grain* α-Mg grains *and* α_e*-Mg refers to the* α*-Mg film in the eutectic aggregate.*

4.3.2 Porosity in as-thixomolded alloy

One of the matters of interest in this work is the presence of porosity in thixomolded magnesium, which can potentially deteriorate its mechanical properties and formability. Optical micrographs, in Fig. 4 show porosity on unetched samples of as-received thixomolded 3 mm thick AM60 Mg both before and after heat treatment at 400^{o}C for 2 hrs. In Fig. 4 (a), porosity in as-received condition varied from about 2 to 3 pct. by volume with bands of high porosity regions. These are possibly from the die filling.

The porosity in heat treated condition varied from about 6 to 8 pct. by volume as shown in Fig. 4(b). The pore size typically increases and the number density of pores decreases although no detailed characterization was performed. Pore coalescence is believed to be responsible for this as some of the pores observed are on the order of millimeters in size. This heterogeneous distribution of entrapped gas porosity and their growth can be the reason for observed differences in pore size between as-received and heat treated thixomolded AM60 samples. The microstructure of heat-treated AM60 in Fig. 4(c) shows a single phase structure and it shows grain boundary fissuring, which may be a mechanism for transport of gas pores to collect in larger bubbles as shown later. Pore distribution in thixomolding process or the effect of isothermal hold has not been

systematically studied to our knowledge; it is usually attributed to the entrapment of air or the argon gas during secondary solidification, but generally any possible role of oxide or hydrated oxide film on feedstock is not discussed.

Fig. 5(a) and (b) show that after heat treatment at 400^{o}C for 2 hrs, approximately 40% sample surface area is covered by pore bubbles and blisters (2-5 mm in diameter) pushing through the surface. As shown in Fig. 5(c) the large size pore bubbles push through sample surface, and the significant enlargement in their size cannot be simply due to pore coalescence, because during isothermal hold coalescence of many pores would tend to reduce pressure in the larger pore. This effect must be primarily due to evolution of new gas pores that were not observed in the as-molded condition. Such expansion is possible only if hydrated oxides dissociate to release hydrogen gas as a function of time, as is well know from Al alloy practices. Although the beta particle network shown in Fig. 3(c) is dissolved during heat treat and a homogenous single phase microstructure is obtained as shown in Fig. 4(c), this blistering effect is a sign that as molded material due to the rapid processing is in a metastable state with regard to gas phase separation from alloy. But this internal gas could limit formability.

4.3.3 Microstructure and porosity in hot rolled thixomolded Mg

Preheating for hot rolling is for a short time and carried out at lower temperature than that used in section 3.2 and for this case blistering problem was not as intense. Fig. 6 shows blistering effect observed on hot-rolled sheet. These gas blisters are 1-3 mm in size and could be responsible for variability in tensile properties. In Fig. 7 (a) and (b) SEM micrographs of hot rolled AM60 show elongated grains aligned in the rolling direction. Arrows indicate shallow channels between elongated grains, which are sections

of elongated gas pores somewhat flattened during the hot rolling. In some locations longer pore channels were fragmented and became intermittent. Polishing and etching of samples reveals them. These pore channels are believed to cause reduced ductility and variability in mechanical properties especially along the transverse direction tensile tests. The fact that these features appear between α_s-Mg phase where eutectic phase is located that is last to freeze during alloy molding suggest that internal gas porosity and shrinkage cavities are likely to be located here. When an etchant attacks polished surface the shallow channels (typically smeared by polishing step) are revealed.

It was thought that additional grain refinement would occur after a second rolling step but it appears that saturation in grain refinement has occurred as shown in Fig 7(b). It is well known that a characteristic grain dimension exists for hot rolling below which the structure does not refine further with strain [32]. The dislocations generated due to the large imposed strains also reach saturation for 350^{o}C at the observed grain size. The mean grain size of 4.2 μm for hot rolled AM60 Mg does not change much with additional rolling passes, but with longer exposure to temperature during subsequent rolling operation, the finer pores seem to transport gas molecules by diffusion and cause coalesce to permit visibility of the voids.

The data obtained from the room-temperature tensile tests of single sheet hot rolling presented in Table.1 show significant statistical variability in different mechanical properties. The strengths and ductility varied with every sample and low strain rate sensitivity values are observed for these alloys in hot rolled condition [13]. The tensile strength varies from 250 MPa to 318 MPa, while uniform elongation varies from 4.8 to 16.5 % in hot rolled condition. Additional tests were done on hot roll bonded Mg alloy

sheets and a similar variability in mechanical properties was observed, stack roll bonding had similar strengths and ductility as compared to the single rolled sheets. This complex behavior is possibly related to the bands of high porosity and surface blisters. Fig. 7 (c) shows the SEM image of hot rolled sample containing MgO particles, EDXS examination on the right corner confirms the presence of MgO particles that remain even after the hot rolling process. Oxide particles are likely to initiate cracks during mechanical tests and reduce tensile elongation.

Fig. 8 shows the fracture surface from tensile tests carried out at room temperature; elongated gas porosity channels are visible in the fracture surface as demonstrated in Fig.7. The fracture path preferentially goes through regions containing large amount of clustered porosity. The high localized porosity may be present in the regions containing large gas pore channels or regions containing a large number of clustered smaller gas pores.

4.3.4 Microstructure and porosity in FSP thixomolded alloys

Since the tool pin partially penetrates the depth of work piece during FSP, sheet thickness can be divided in two distinct zones as shown in Fig. 9. The stirred zone and heat-affected zone (HAZ) have been identified and marked as 1 and 2 in Fig. 9 (a). The interface between the recrystallized stirred zone and the HAZ is also visible. The HAZ is located in the middle of the sample. The microstructural changes in these zones have significant effect on post processing mechanical properties.

The HAZ is shown in Fig. 9(b). It retains the grain structure similar to the as-molded AM60 Mg. FSP process has relatively small effect on microstructure homogenization of middle layer (HAZ); but it results in the complete dissolution of

network of eutectic mixture of α_e-Mg and an intermetallic compound β ($Mg_{17}Al_{12}$) into a uniform α-Mg matrix and reduction of primary solid α-Mg phase by melting. This uniform microstructure is likely to improve ductility and formability especially at elevated temperatures. The stirred zone microstructure is shown in as shown in Fig. 9(c). Intense plastic deformation and frictional heating during FSP result in generation of a recrystallized fine-grained microstructure throughout the stirred zone. Since FSP results in temperature increase up to 300-350^{o}C within the stirred zone, due to frictional heating and plastic deformation, eutectic intermetallic mixture and primary solid phase α_p-Mg dissolve into α_s-Mg matrix and the microstructure is observed to consist of relatively equiaxed grains (5-7 μm) of with homogeneous composition characteristic of AM60 (Mg + 6% Al) . The general features of the processed zone microstructure and elimination of β ($Mg_{17}Al_{12}$) particles is consistent with the earlier reported FSW findings for thixomolded AZ91D and AM60 [26, 27].

The effect of FSP on porosity and gas inclusions is presented in optical micrographs in Fig. 10, which shows features of porosity on unetched samples of FSP thixomolded 3 mm thick AM60 Mg, both before and after heat treatment at 400^{o}C for 2 hrs . The porosity has decreased from 2- 3 vol. pct. in the as-molded condition to < 1 vol. pct. in the FSP condition. It is likely that any evolving gas bubbles are easily thrown out from hot circulating material in stir zone during FSP. Furthermore, the vigorous flow of friction stirred Mg promotes coalescence of bubbles and their elimination by expulsion from the softened zone. During FSP gas bubbles may drift with flow of metal. Also they have a tendency to diffuse toward the surface due to the difference in the densities of the bulk material and the bubbles. It is fair to expect that due to repeated and rapid thermal

cycles in each over lapping pass, big pores formed in the stirred zone will have more time to be expelled. The rpm and traverse speed for process are likely to affect this bubble removal process. However, small pores may not be removed fully in available time of a stir cycle.

Another important observation that supports the findings described in the previous paragraphs is that pores are located in HAZ while the stirred zones are virtually free from porosity. The proximity and connections between the large and the small pores and the shape of the large pores in Fig. 10 (b) reveals possible nucleation of new pores, the growth of the pores resulted from the coalescence and expansion of the remaining small pores in the HAZ of the friction stir processed AM60 Mg. After heat treatment some porosity bubbles are visible at the surface but the size of the pores is considerably smaller than what was observed in the as-received material after heat treatment. In short FSP remedies the two main problems of thixomolded material i.e. eutectic phase has been dissolved in both zones and the inherent porosity and gas inclusions have been nearly removed from the stirred zone and significantly reduced from HAZ.

4.3.5 Elevated temperature formability

The sheet obtained after 35 overlapping FSP passes and press flattening was placed between a pair of heated corrugated dies to perform biaxial forming. The flat work piece was isothermally pressed and corrugated between the sine-wave dies with lateral constraint as shown in Fig 2(b). This is primarily a plane-strain operation which causes plastic bending and stretching of the work piece. The plastic strain has a gradient in the thickness direction from a high value at the exterior stirred zone surface to a lower value in the interior HAZ of the material. The wavy work piece from the as-thixomolded Mg

shows fractures on the surface indicating poor formability Fig. 11 (a). The extensively deformed FSP Mg withstands multiple cross-corrugations successfully as shown in Fig. 11 (b). The FSP work piece shows no cracking or other surface defects. It proved to be an excellent material with extensive formability for severe biaxial deformation during ABRC process.

It has been demonstrated that the FSP AM60 Mg showed higher formability during biaxial stretching and bending operation without surface cracking or fracture. This indicates that the fundamental obstacle to its elevated temperature formability in as-thixomolded condition has been eliminated by FSP. Hence we have established that FSP enhances the ductility by modifying the complex cast-microstructure of the thixomolded AM60 Mg into a homogenous wrought microstructure with reduced gas porosity and paves the way for wrought processing of thixomolded alloys.

4.4 Conclusions

(1) Thixomolded alloys contain shrinkage and gas (air) porosity, as well as localized processing defects such as internal oxide films and entrapped residue that affect mechanical properties and formability of these materials. Strain incompatibility between the body-centred cubic beta-phase and the hexagonal close-packed alpha-phase leads to brittleness of AM60 Mg in as-thixomolded condition.

(2) A porosity study after isothermal exposure to elevated temperature shows pore expansion and calescence, and evolution of new gas molecules and transport of pore bubbles and formation of blisters on the sample surface. A significant increase in volume percent porosity is witnessed in the heat treated AM60 Mg.

(3) The expansion of pores with elevated temperature exposure suggests that internal pressure is created by greater volume of gas in the alloy with time, possibly due to hydrogen evolution. The ductility is likely to be influenced by pore size and heterogeneous distribution of pores.

(4) Hot rolling of thixomolded AM60 Mg results in some grain refinement but shallow channels between elongated grains are observed in the etched condition. The data obtained from room temperature tensile tests shows significant variability in different mechanical properties and the fracture surface shows pore channels.

(5) Friction stir processing of the thixomolded AM60 Mg enhances ductility by fragmenting the grains and in the process dispersing and removing any internal hydrated oxide films and entrapped gases associated with it. It produces homogeneous, recrystallized, equiaxed grain (5-7μm) structure (Mg+6% Al) with no apparent loss in strength in the stirred zone. In HAZ it causes complete dissolution of intermetallic particles but some primary solid α_p-Mg particles remain near the mid surface

(6) During FSP, gas bubbles may drift toward the surface. The friction stir processed thixomolded AM60 Mg shows enhanced ductility by almost completely removing porosity from stirred zones while significant reduction in porosity is seen in HAZ.

(7) The elevated temperature formability of the FSP-processed Mg is significantly improved than the as-received thixomolded AM60 Mg. Fracture and cracking at elevated temperature is typically due to pore formation and coalescence, but the FSP Mg is biaxially formed without cracking when pressed in sinewave shaped dies by bending and stretching at elevated temperature (ABRC). The present study shows that partial depth multi pass FSP can be used to produce highly formable Mg plates which may also be readily rolled into sheets if desired with improved properties.

Table 4.1 Nominal composition range of thixomolded AM60 Mg (in wt. %)

Al	Mn	Zn	Si	Mg
5.6-6.4%	0.26-0.5	0.20 max	0.05 max	Bal.

Table 4.2 Mechanical properties of hot rolled thixomolded AM60 Mg

Test Condition	**Prop Limit (MPa)**	**Yield Strength (MPa)**	**Ultimate Tensile Strength (MPa)**	**Uniform Elongation (%)**	**Total Elongation (%)**
As-mold	40 - 49	125 - 140	195 - 210	4.0 - 5.4	4.1 - 5.5
Hot Rolled	40 - 90	188 - 260	250 - 318	4.8 - 16.5	5 - 19.5

* Several other room temperature tensile tests were carried out on hot roll bonded thixomolded alloys; similar strengths and ductility were observed. In short stack rolling didn't seem to have much effect on variability of mechanical properties.

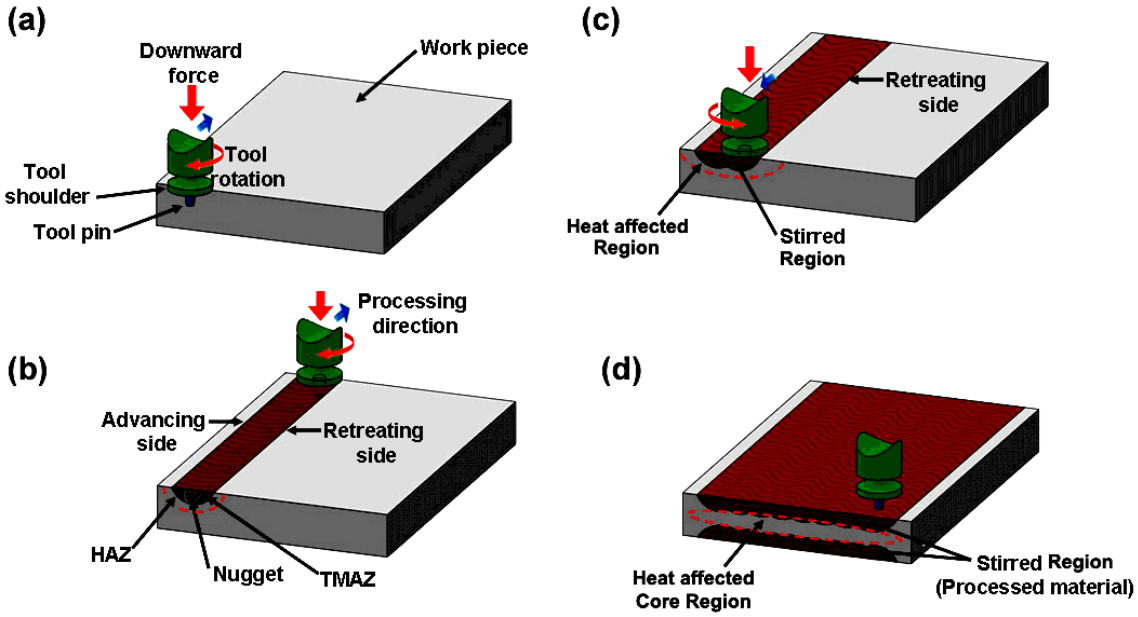

Figure 4.1 Schematic illustration shows several stages of overlapping passes for partial depth FSP, stirred region (processed material) and heat affected core region (base material) have been identified.

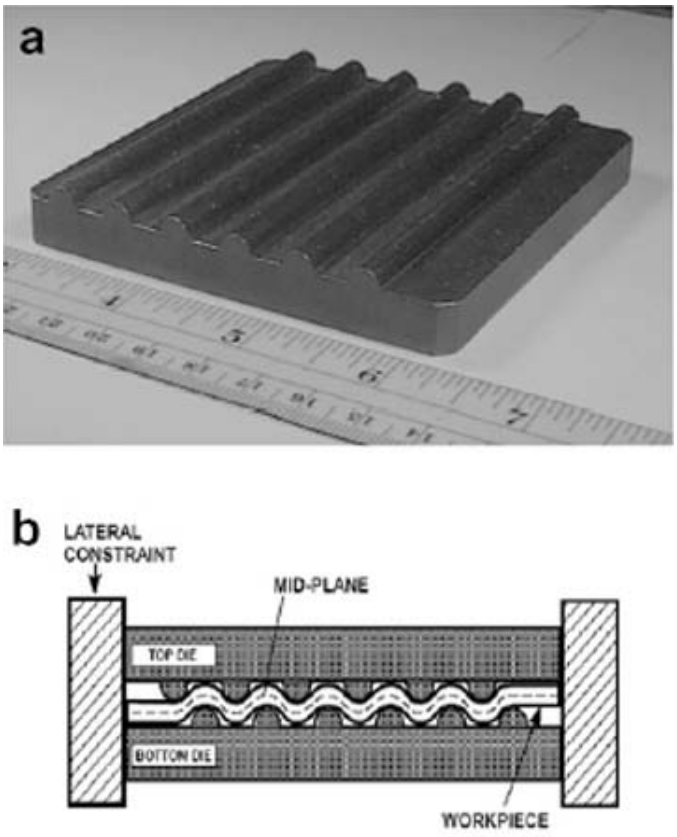

Figure 4.2 (a) Sinewave dies used for sheet corrugation; (b) schematic shows Alternate Biaxial Reverse Corrugation (ABRC) process, in which a metal work piece is corrugated between sine wave shaped dies. The work piece is under lateral constraint during processing [30].

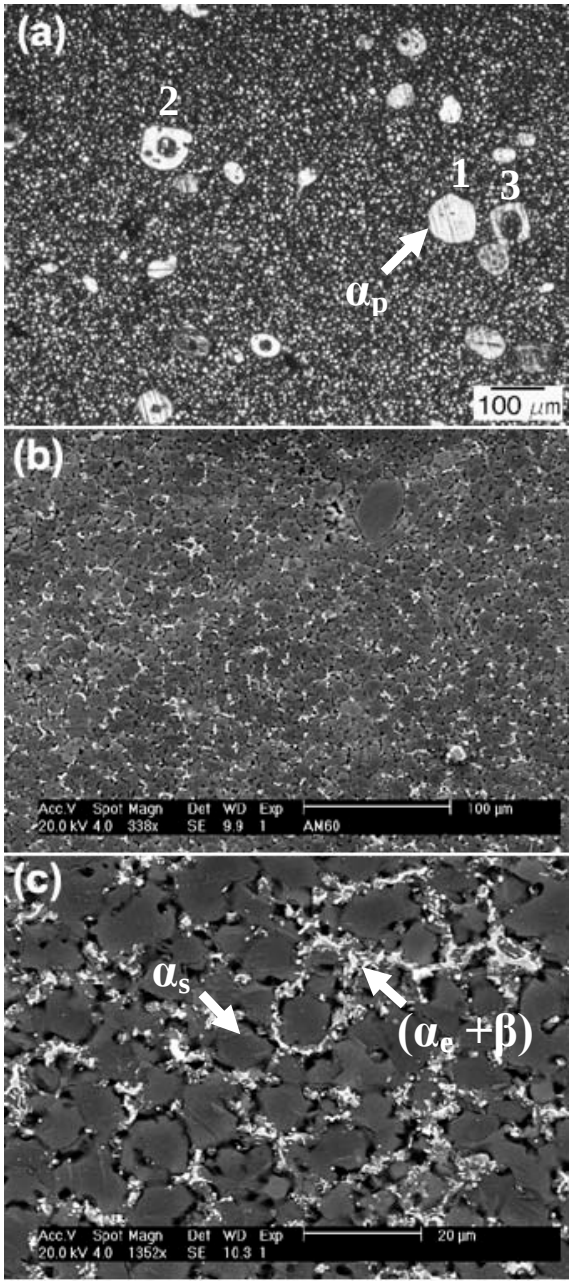

Figure 4.3 Microstructure of as-thixomolded AM60 Mg . Optical micrograph in (a) shows the overall structure and three distinct morphologies of primary solid phase α_p-Mg particles. SEM micrograph in (b) shows matrix of equiaxed secondary α_s-Mg grains. SEM micrograph in (c) shows the eutectic ($\alpha_e + \beta$) intermetallic network, distributed in spaces around secondary α_s-Mg grains (indicated by the arrow).

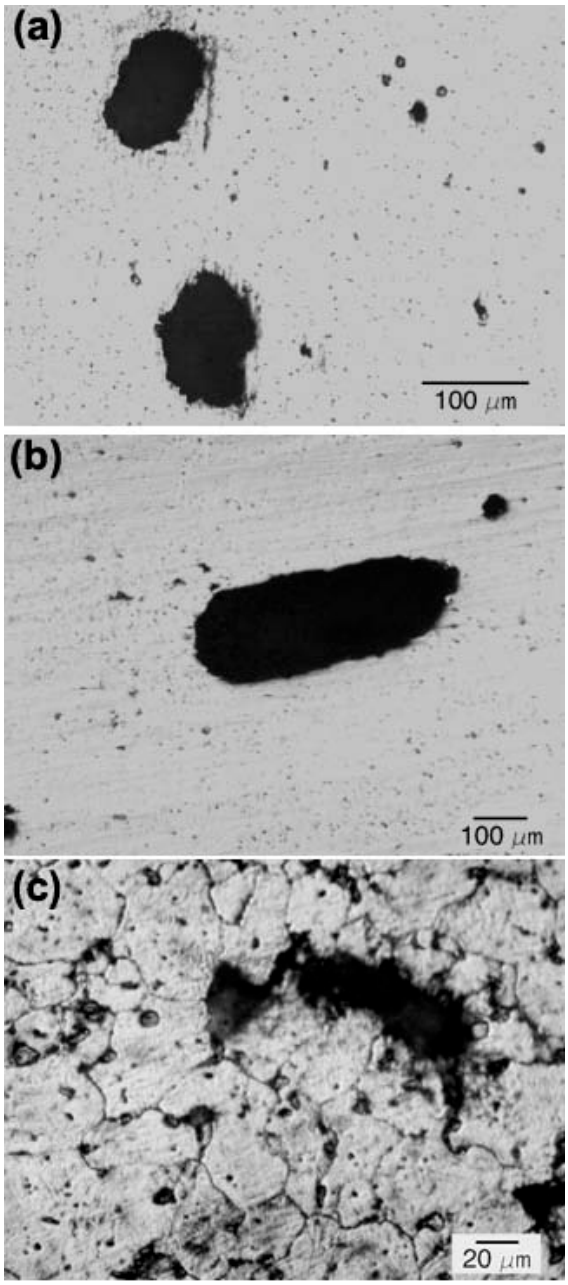

Figure 4.4 Optical micrographs showing features of porosity on samples of as-received thixomolded 3 mm thick AM60 Mg, (a) un-etched micrograph shows 2-3% by volume porosity in as-received AM60 before heat treatment; (b) un-etched micrograph shows 6-8% by volume porosity in as-received AM60 after heat treatment at 400^{o}C for 2 hrs (c) etched micrograph of the heat treated thixomolded AM60 shows grain boundary fissuring while the eutectic intermetallics have been completely dissolved.

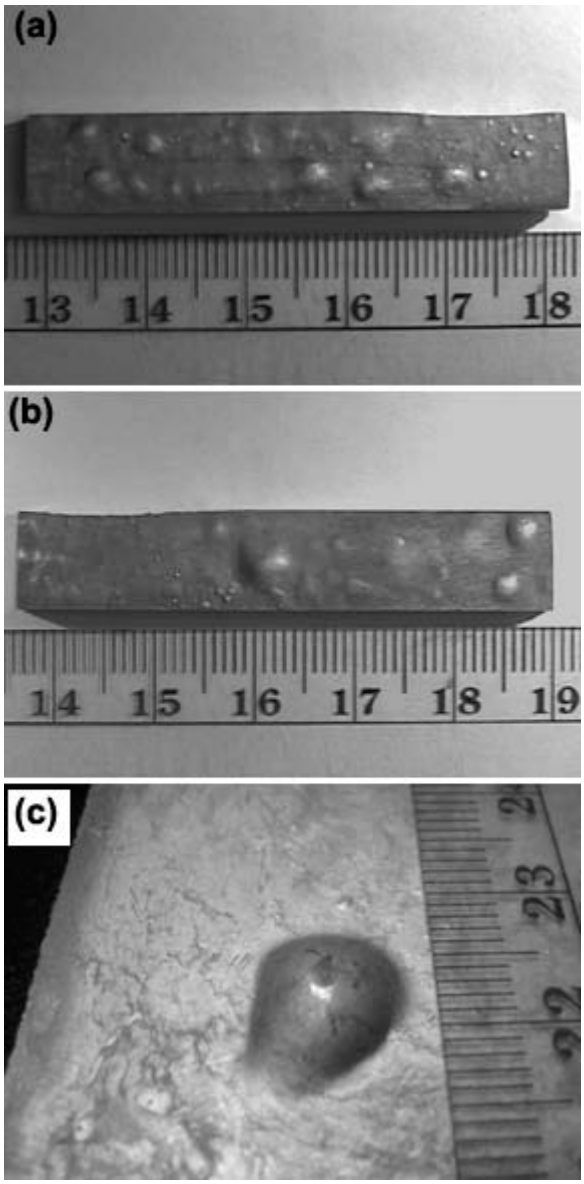

Figure 4.5 (a) & (b) Macrographs of thixomolded AM60 Mg samples after heat treatment show bubbles and blisters on the surface of 3 mm thick plates (face of plate shown). Almost 40% surface area of alloy plate is covered by pore bubbles and blisters (c) The porosity bubbles on the surface and the increase in their size can be attributed to expansion of the surface by increased internal gas pressure in pores.

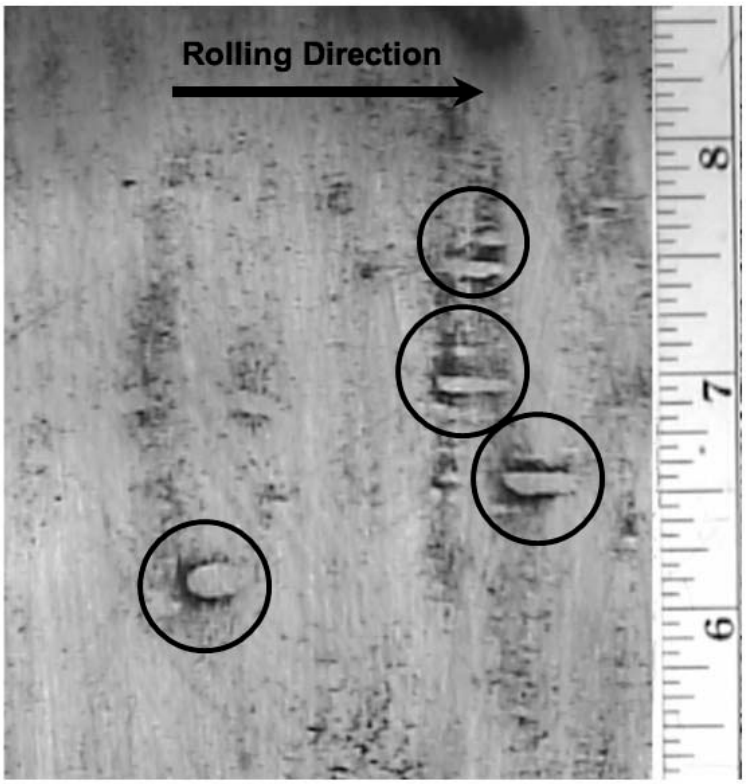

Figure 4.6 The macrograph of the surface hot rolled thixomolded AM60 plate. Highlighted areas show the formation of blisters which are possibly related be related to inherent porosity. These pores are somewhat elongated in the rolling direction and form channels that may adversely affect the mechanical properties of these alloys in the hot rolled condition.

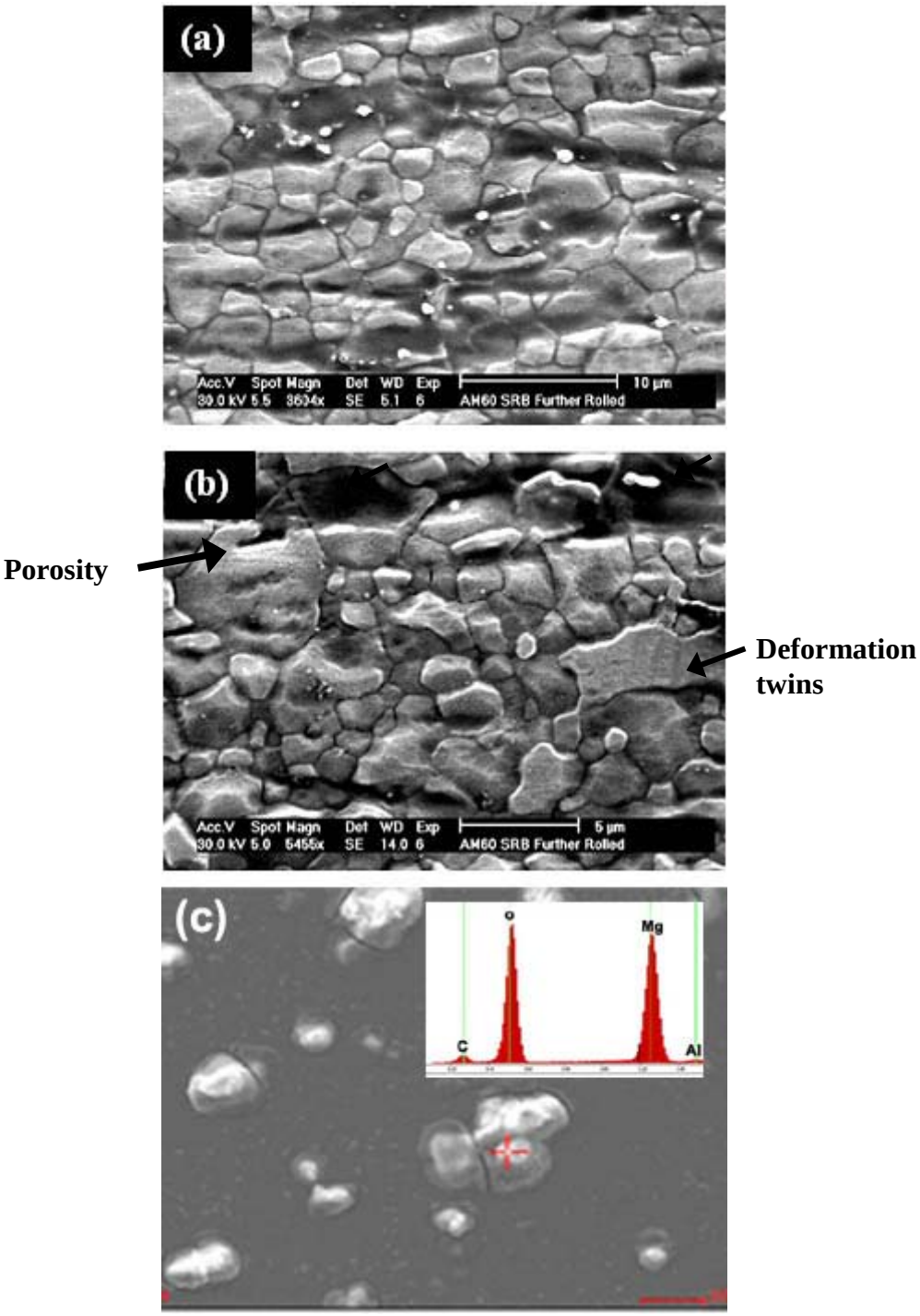

Figure 4.7 Grain structure of thixomolded AM60 Mg after hot rolling at T=350^{o}C, viewed under the SEM; (a) After 80% reduction the elongated grains aligned in the rolling direction are seen, arrows indicate some shallow channels which may be result of the internal inherent porosity, (b) magnified view showing grain structure after 2nd rolling step, some twinning is observed in grains that are > 6 µm size, while the eutectic phase has completely dissolved. In (c) SEM image shows MgO particles in rolled condition microstructure (inset shows EDXS).

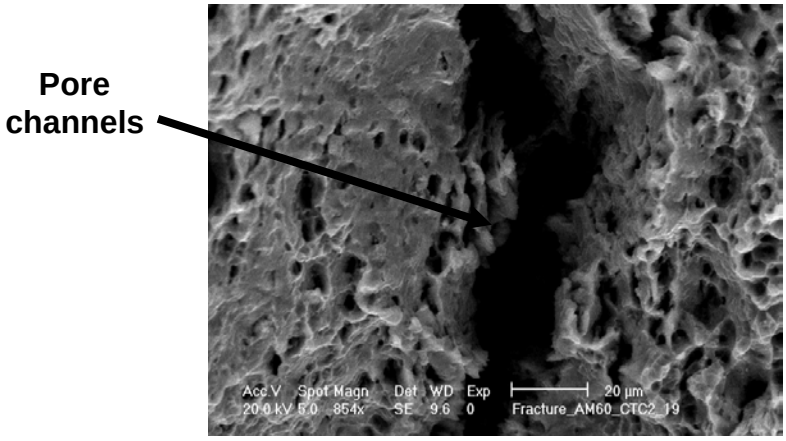

Figure 4.8 SEM micrograph shows fracture surface of a tensile test specimen depicting porosity and pore channels.

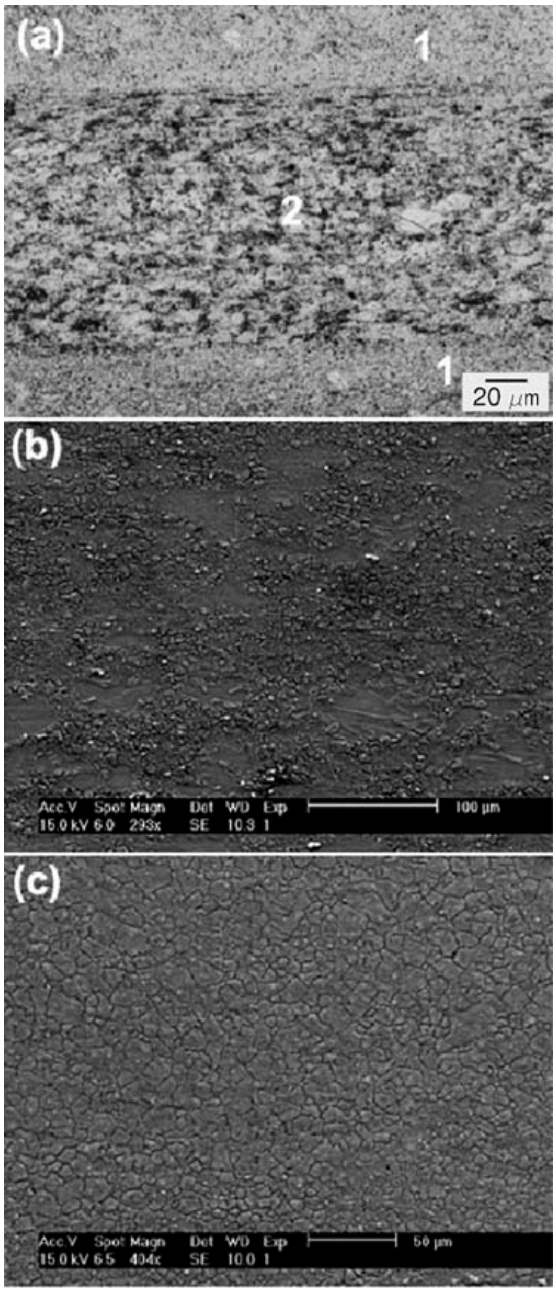

Figure 4.9 (a) Optical micrograph shows the microstructure of friction stir processed AM60 Mg, two distinct zones are identified as '1' and '2', the top and bottom layer represent the microstructure of the FSP zone. The layer in the middle represents the unprocessed zone. (b) SEM micrograph shows the microstructure of middle layer, it still shows some primary solid fraction but shows complete absence of intermetallic network. (c) SEM micrograph shows the microstructure of the top and bottom friction stir processed layers, clearly the cast microstructure is converted to a homogeneous (Mg + 6% Al)), recrystallized, equiaxed grain (10–15 μm) wrought microstructure in the stirred zone.

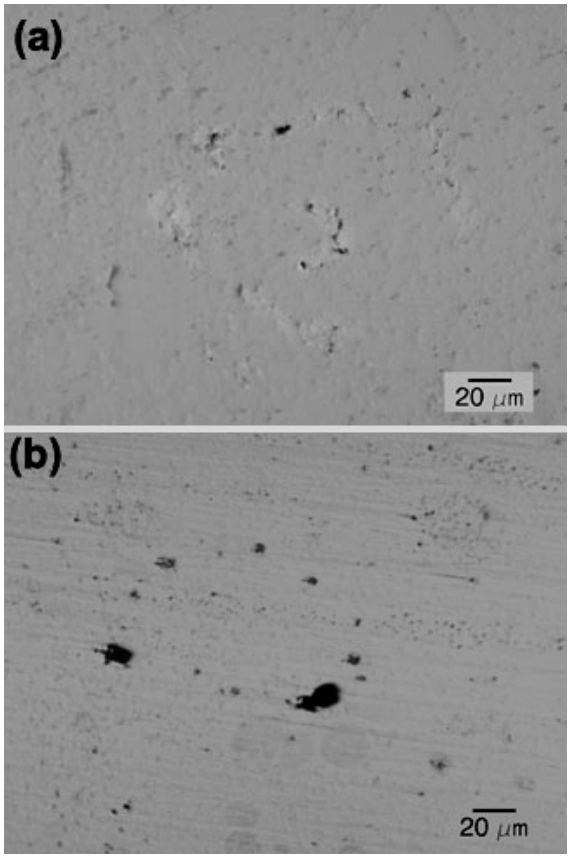

Figure 4.10 Optical micrographs showing features of porosity on un-etched samples of FSP Thixomolded 3mm-thick AM60 , both before and after heat treatment (a) FSP AM60 Mg before heat treatment ; (b) FSP AM60 Mg after heat treatment at 400^{o}C for 2 hrs .

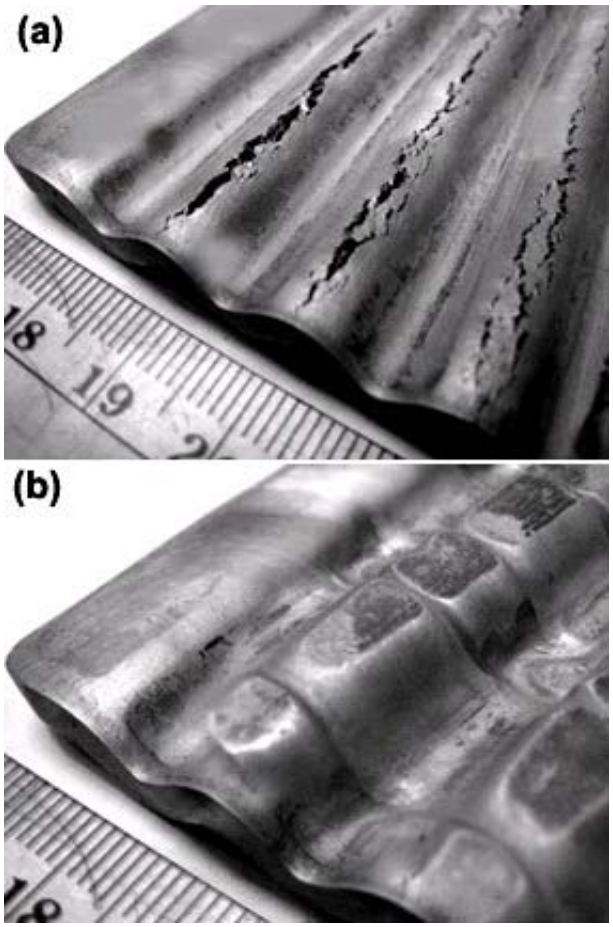

Figure 4.11 Pictures show the comparison of ABRC processed work pieces for the two process conditions under similar parameters, (a) shows the as-received Thixomolded AM60 work-piece after the initial ABRC step, extensive cracking is visible and no further processing can be carried out. (b) Shows the friction stir processed thixomolded AM60 work-piece after initial ABRC step, it shows improved ductility and is readily processed. The details of ABRC processing are given elsewhere [26].

4.5 References

[1] A.A. Luo, *JOM* ,54 (2002), pp. 42-48.

[2] B.L. Mordike and T. Ebert, *Mater. Sci. Eng. A*, 302 (2001), pp. 37-45.

[3] L. Riopelle, *JOM* ,48 (1996), pp. 44-46.

[4] P.B. Partridge, *Metall. Rev*., 118 (1967), pp.169-194.

[5] E.F. Emley, *Principles of magnesium technology*, Pergamon Press Ltd, (1966), pp.1013.

[6] E. Doege and K. Droder, *Journal of Materials Processing Technology*, 115 (2001), pp.14-19.

[7] O.A. Kaibyshev, *Mater. Sci. Eng. A*, 324 (2002), pp. 96-102.

[8] K. Kubota, M. Mabuchi and K. Higashi, *J. Mater Sci,*. 34 (1999), pp. 2255-2262.

[9] A.V. Sergueeva, V.V. Stolyarov, R.Z. Valiev and A.K. Mukherjee, *Mater. Sci. Eng. A*, 323 (2002), pp. 318-325.

[10] G. Song and A. Atrens, *Advanced Engineering Materials A*, 9 (2007), pp.177-183.

[11] K. Matsubara, Y. Miyahara, Z. Horita and T.G. Langdon, *Acta Mater*., 51 (2003), pp.3073-3084.

[12] X. Li, A.K. Ghosh and R.F. Decker, *Magnesium technology*, (2007), pp.221-226.

[13] B. Mansoor, A.K. Ghosh and R.F. Decker, technical report presented at the University of Michigan, (2007), pp. 73.

[14] L. Pasternak, R. Carnahan, R.F Decker, and R. Kilbert, *Proceedings of the 2nd International Conference on the Processing of Semi-Solid Alloys and Composites*, 1993, pp. 159-169.

[15] J. Mihelich and R.F. Decker, *Apparatus for Processing Corrosive Molten Metals*, U.S. Patent 5,711,366, 1998.

[16] S.J. Splinter, N.S. McIntyre, W.N. Lennard, K. Griffiths, G. Palumbo, *Surface Science*, 292 (1993), pp.130-144.

[17] G. Song, A. Atrens and M. Dargusch, *Corrosion Science*, 41 (1999), pp. 249-273.

[18] J.C. Fuggle, L.M. Watson, D.J. Fabian and S. Affrosman, *Surface Science*, 49 (1975), pp.61-76.

[19] J. R. Pickens, *JOM*, 16 (1981), pp.1437-1447.

[20] V. Chiavazza, M. Pijolat and R. Lalauze, *JOM* ,23 (1988), pp. 2960-2964.

[21] D.M. Walukas, R.F. Decker, A.W Totten, *Proceedings of Minerals, Metals and Materials Society Annual Meeting*, 2001, pp. 95-98.

[22] F. Czerwinski, *Acta Mater*., 50 (2002), pp. 2639-2654.

[23] Y.Z. Lu, Q.D. Wang, W.J. Ding, X.Q. Zeng and Y.P. Zhu, *Mater. Lett*., 44 (2000), pp. 265-268.

[24] R. S. Mishra, M. W. Mahoney, S. X. Mcfadden, N. A. Mara and A. K. Mukherjee, *Scripta Mater*., 42 (2000), pp.163-168.

[25] K. Nakata, S. Inoki, Y. Nagano, T. Hashimoto, S. Johgan, M. Ushio, *Journal of Japan Institute of Light Metals*, 51 (2001), pp. 528-533.

[26] S. H. C. Park, Y. S. Sato, H. Kokawa, *J. Mater Sci*., 38 (2003), pp. 4379-4383

[27] J. A. Esparza, W. C. Davis, L. E. Murr, *J. Mater Sci*., 38 (2003), pp. 941-952.

[28] Y. S. Sato, S.H.C. Park, A. Matsunaga, A. Honda and H. Kokawa, *Mater. Sci. Eng. A*, 40 (2005), pp. 637-642.

[29] M. Santella, A. Frederick, C. Degen and T.Y. Pan, *JOM*, (2006), pp. 56-61.

[30] P. Cavaliere, P.P.D Marco, *J. Mater Sci.* 41(2006), pp. 3459-3464.

[31] Q. Yang and A.K. Ghosh, *Acta Mater.*, 54 (2006), pp. 5147-5158.

[32] J. J. Jonas and T. Sakai, *Deformation, processing, and structure*, G. Krauss (Ed.), ASM Materials Science Seminar, ASM, Ohio, USA (1982), pp.185-228.

CHAPTER 5

MICROSTRUCTURE AND MECHANICAL PROPERTIES OF AZ31B MAGNESIUM SHEETS PROCESSED BY REPEATED BENDING AND REVERSE BENDING

Abstract

Commercial Mg alloy sheets have low strength and poor formability at room temperature owing to their coarse grain size and strong basal texture. In this study, a method termed “bending reverse bending” (BRB) was applied to improve the mechanical properties of magnesium alloy sheets by microstructure and texture modification. The evolution of microstructure, texture and mechanical properties of Mg sheets processed by BRB are reported here. In BRB processed sheets, $\{10\bar{1}2\}$ twinning was activated at low deformation temperatures during bending along rolling direction and c-axis became inclined to the normal direction. When a BRB processed sheet was warm rolled at 225 °C, the tensile strength at room temperature was considerably improved without loss of ductility. The BRB processed and hot rolled Mg exhibited enhanced superplasticity at low temperatures of 300^{o}C and 350^{o}C. The improved mechanical properties of BRB processed and hot rolled sheet is a direct consequence of a finer grain size and weaker and a more dispersed basal texture along the rolling direction.

5.1 Introduction

There is great interest in Mg alloys for use in aerospace, automobile and electronics industries because of their low density, high specific strength and the ability to be recycled [1-4]. In wrought Mg alloys, the achieved properties to a large extent depend on alloy chemistry and the microstructure. The scale of the microstructure can vary by a large magnitude (mm to micron size) due to a wide range of conventional wrought processing methods e.g rolling, warm-extrusion. AZ31 (with nominal composition Mg–3 wt. % Al–1 wt. % Zn) is currently the most common and commercially important Mg sheet alloy. It is produced by several hot, warm- and cold-rolling steps and exhibits moderate strength of ~200 MPa. Rolling orients the {0001} basal planes approximately parallel to the sheet surface (known as the "basal texture"), with the $\{10\bar{1}0\}$ axis in the rolling direction [5-10]. The microstructure of cold-rolled AZ31 is known to contain extensive twinning [6]. On the other hand, hot-rolled AZ31 and AZ31-H24 tend to have non-uniform and bimodal grain structures [11, 12]. Hot-rolled AZ31 shows a perfect basal fiber texture; while warm-rolled sheet exhibits an egg-shaped distribution of {0001} planes in pole figures [5-10]. A basal texture is considered inadequate for deformation, because it places most grains in such an orientation that the resolved shear stress on the basal planes becomes practically zero. This leads to stress concentrations and premature failure [11]. It is very well known that grain size reduction and formation of basal texture away from rolling plane improves strength and formability of magnesium alloy sheets [12]. Considerable effort is currently being directed to develop secondary thermo-mechanical processing techniques to create fine grain size and weak basal texture in Mg sheets [12]. The eventual goal is the development of high strength

wrought Mg sheets with enhanced ductility, capable of being formed into a variety of products for target industries.

We have developed a new deformation processing method called Bending Reverse Bending (BRB) aimed at refining grain structure and alleviating basal texture of Mg sheets. This new method is based on Tension Roller Leveling (TRL) process, which is conventionally used at room temperature to improve flatness of sheet and strip products [13-16]. TRL process removes shape defects related to length differences such as buckles, pockets, wavy edges and it may also be employed for temper-rolling operations. In TRL process, the material is subjected to a series of alternate bends under superimposed tension as shown in Fig. 1. Shape defects are removed by ensuring that all longitudinal material 'fibers' possesses the same length. In this work, the proposed repeated bending and reverse bending deformation is carried out at warm temperatures to promote recovery and recrystallization during accumulation of large plastic strains. The present paper reports the preliminary results on the effect of bending reverse bending process to refine grain size and modify basal texture of rolled magnesium alloy sheet

5.2 Experimental

Commercial AZ31B magnesium alloy (Mg–3 wt. % Al–1 wt. % Zn) in H-24 temper was used in the work. The as-received Mg was hot rolled at 350^{o}C with 10% thickness reduction steps to achieve a 0.75 mm thick sheet. This hot rolled sheet was subsequently annealed at 375^{o}C to achieve an O-temper, coarse grain condition.

5.2.1 BRB processing

A small BRB processing unit for laboratory experiments is fabricated as shown in Fig. 2 (a). The unit has two non-powered 55 mm diameter H-13 steel rolls. These BRB

rolls are off-set in the horizontal direction to provide the bending reverse-bending path. The work-piece is passed through the BRB rolls and attached to 155 mm diameter coilers. The winding of material on the coilers provides tension. Coiling and uncoiling of material on coilers is used to move the material strip through the BRB rolls. Fig. 2 (b) shows the strip geometry and loading conditions inside the apparatus. The Mg strip, is isothermally bent and reverse bent between a pair of rolls under tension with a constant speed. This is primarily a plane-strain operation which causes plastic bending and reverse-bending of strip along the rolling direction. The strip is traversed back and forth between the BRB rolls. In this manner, a large number of bending reverse-bending cycles are performed on the strip. The strip processing zone is inside a heated chamber. The temperature inside the chamber is maintained by a steady stream of low pressure hot air. Instrumentation was available to measure and control coiler speeds.

When a sheet is subjected to a pure bending moment as shown, it is observed that axial fibers bend to form circumferential fibers and transverse fibers remain straight and become radial fibers. In the process of bending there are axial fibers that do not extend or contract. The surface in the middle, described by a fiber that do not extend or contract is called the neutral axis. Lines on one side of the neutral surface extend and on the other contract since the arc length is smaller on one side and larger on the other side of the neutral surface. The Fig. 1(b) shows the neutral axis in the bent configuration. The axial engineering-strain per unit length in a fiber at distance *y* above the neutral fiber can be expressed during bending by e:

$$e = \frac{l - l_o}{l_o} = \frac{\theta(\rho - y) - \theta\rho}{\theta\rho} = -\frac{y}{\rho} \tag{1}$$

where ρ, is the radius of to the neutral axis. The reverse-bending part of strain is estimated in a similar manner and is superposed. In bending reverse-bending experiments significant elongation takes place due to applied tension. The total deformation strain is estimated by adding the bending reverse-bending and elongation strain. It was estimated that under low deformation temperatures each BRB cycle results in approximately 3-5 % engineering strain.

Strips of 450 mm × 50 mm (length × width) size; cut from 0.75 mm and 2.5 mm thick Mg sheets were used here. An experimental program was used here to examine the effectiveness of BRB processing in grain refinement and texture modification. The experimental study consisted of 4 test programs. The thickness and deformation temperature was varied during these experiments.

The microstructural examination of as-received, as-processed and hot rolled samples was performed by optical and scanning electron microscopy. Metallographic specimens were cold mounted in self-curing resin, fine ground and mechanically polished and were later etched with acetic-picral solution. The acetic-picral solution contains 4.2 g picric acid, 70 ml ethanol, 10 ml acetic acid and 10 ml distilled water. A Philips XL30-FEG SEM was employed to observe the very fine microstructure at higher magnifications. The mechanical properties at room-temperature were investigated by tensile testing. The tensile tests specimens were machined in the rolling direction. The tensile strength, 0.2% yield stress and elongation were obtained by averaging data from at least three tests in each condition. Additionally some high-temperature constant strain

rate tests were also performed. The details of high-temperature tensile testing and specimens have been described in previous Ref. [17].

5.3 Results and discussion

5.3.1 Microstructure and texture evolution

Microstructure of as-received AZ31-H24 Mg is shown in Fig. 3. In (a) microstructure of near-surface region shows fine grains inside shear bands. Extensive twinning is seen in coarse grains. In (b) microstructure of mid-surface region shows relatively coarse grain microstructure. Some twins are also visible. The average grain size of as-received AZ31 Mg is 8 μm. In (c) {0002} experimental pole figure of the as-received material shows a slight off-basal character to the primarily basal texture [18].

Microstructure of hot rolled and annealed 0.75 mm thick AZ31 Mg sheet is shown in Fig. 4. In (a) coarse grains evolve after hot rolling at 350 ^{o}C and annealing at 375 ^{o}C / 5hr. In (b) the structure is relatively homogenous in the ND-RD cross-section. The average grain size is 25 m. In (c) {0002} experimental pole figure of the hot rolled and annealed sample shows a perfect basal texture [5-10]. The intensity of basal poles increases to 12 multiples of random (MRD).

The experimental program was started by BRB processing of 0.75 mm thick sheet at 200^{o}C. A total of 1500 BRB cycles were applied to the sample but no significant change in thickness was observed in this experiment. Therefore, it was assumed that the deformation occurred only by bending and reverse-bending. The microstructure of 0.75 mm thick hot rolled and annealed strip processed at 200^{o}C by 2000 bending reverse bending cycles is shown in Fig. 5. In (a), a fine grain structure (3 μm) evolves in the near-surface regions; while the core region shows an equiaxed coarse grain (10 μm)

microstructure. The fine grain structure shows extensive twinning. The grain size of finer grains is about. In (b) higher magnification image shows coarse grain structure in the mid-surface region of the strip after processing. The amount of deformation experienced by the region near the surface is higher than that in the center, which makes it possible to produce a finer grain size in near surface regions. The {0002} experiment pole figure in (c) shows a perfect basal texture similar to the starting condition but the intensity of basal poles is decreased to ~10 MRD. This shows that bending reverse-bending reduces the intensity of basal poles. However, the c-axis is still mainly distributed parallel to the ND.

The next set of experiments was performed on the 2.5 mm AZ31 Mg sheet in H-24 condition, to increase the amount of strain per BRB cycle. The BRB cycles were carried out at 250^{o}C, 200^{o}C and 180^{o}C. The microstructures presented here are after 1000 BRB cycles in each case to make comparisons. All of the presented micrographs were taken for the near-surface regions, where the bending deformation was severe. In the first case, the strip elongates after BRB at 250^{o}C. The final thickness of the strip is 2.0 mm. As shown in Fig. 6 (a), grain growth is evident. The as-received microstructure recovers under the high deformation temperature and in (b) an equiaxed coarse grain microstructure (15 μm) evolves in the strip. Further processing under these conditions did not reveal any evidence of grain refinement. It is difficult to activate basal slip during bending because of the strong basal texture of as-received sheet. Therefore, the next BRB experiment was carried out at 200^{o}C, to promote twinning which is beneficial in grain refinement. The microstructure of AZ31 Mg BRB processed at 200^{o}C and 1000 cycles is shown in Fig.7. In (a) the average grain size is approximately 10 μm, and presence of small grains near grain boundries indicate recovery and perhaps some amount of

recrystallization. In (b), arrows indicate several twins present in the coarse grain interiors. The final BRB experiment was carried out at 180^{o}C, to promote more twinning. It should be noted that earlier investigations have shown that significant recovery is possible during deformation at this temperature [12]. The microstructure of AZ31 Mg BRB processed at 180^{o}C is shown in Fig. 8. In (a) fine grain structure evolves in the material with an average grain size of 4 μm. In (b) higher magnification shows that BRB causes significant grain refinement and the as-received microstructure has been considerable refined. In (c) the {0002} pole figure shows a basal texture still exists in BRB processed sheet, but the intensity and distribution of basal changes considerably. The basal pole intensity is ~7 MRD and a broader distribution with a tilt in the RD is seen. The structure is homogenous. The 180^{o}C BRB processed samples were warm rolled at 200 and 225^{o}C in a single step of 60% thickness reduction. The procedure for hot rolling is described in Ref. [17]. Fig. 9 shows the microstructure BRB-processed AZ31 Mg after hot rolling at 225^{o}C with true strain 1.0. In (a) fine grain structure shows that BRB-processed structure has been further refined significantly along the rolling direction by warm temperature rolling. Twinning was not seen and the over all grain structure is homogeneous. Over all BRB processing under this condition produced a homogenous and fine grain structure with 2 μm average grain size in the entire strip. In (c) the {0002} pole figure shows a basal texture still exists in BRB processed sheet after warm rolling, but the intensity and distribution of basal changes considerably. The basal pole intensity is decreased to ~5 MRD after warm rolling and a much broader distribution of basal poles is observed. The BRB experiments performed below 180^{o}C resulted in crack

formation on strip surfaces leading to fracture. At temperatures < 180^{o}C, material was able to withstand very few BRB cycles before failure due to fatigue.

In summary, at the beginning stage of the BRB processing, when the sheet passes over the rolls, it is very difficult to activate basal slip during bending because of the strong basal texture. At this stage, plastic deformation depends mainly on prismatic slip and twinning. The result of prismatic slip is that the grains rotate around the c-axis, but the basal-plane orientation does not change. However, pyramidal twins cause the basal planes of the grains to rotate to an orientation that forms an angle with the untwined region. As more deformation is imparted, the orientations and stress states of the grains change because of the alternating operations of slip and twinning. With an increase in the basal Schmid factor and activation of the basal slip system, an angle is formed between the basal planes of the grains and the bending direction so that the c-axis becomes inclined from the ND towards the RD. This results in a broader distribution of basal poles around the ND with a tilt in the RD, thereby weakening the basal texture.

5.3.2 Mechanical properties

The mechanical properties of as-received, as-processed and warm rolled conditions are given in Fig. 10. The room-temperature tensile stress-strain plots show many differences which can be attributed mainly to the effects of finer grain size and texture. .The following can be inferred from the plot and the table. First, the BRB processed and hot rolled samples exhibit improved strength with adequate ductility as compared to as-received counterparts. Second, the yield and ultimate strength of processed material increases with decrease in grain size. Third, while yield strength significantly increased after BRB processing and warm rolling, tensile elongation

decreased as compared to coarse grain counter parts. Over all, the 2 μm fine grain AZ31 Mg after exhibited the highest strength (YS= 332 MPa, UTS = 270 MPa); while superior ductility of 16% was achieved.

Fig. 11 shows typical (σ-ε) flow curves of as-processed and warm rolled AZ31 Mg alloy subjected to strain rate of and 2 x 10^{-4} s^{-1} at selected temperatures of 300^{o}C and 350^{o}C. The true stress is calculated under an assumption that specimens undergo uniform deformation. This assumption does not hold after the maximum stress level and the true stress values after stress peak are too low. Increasing temperature or decreasing strain rate leads to a lower peak stress, higher tensile elongations and fracture strains. The as-processed AZ31C alloy shows a maximum tensile elongation of 225% at 350^{o}C and 2 x $10^{-4}s^{-1}$. Extensive initial strain hardening takes place at 300^{o}C, while a steady strain hardening is for higher test temperatures. At 300^{o}C after reaching a maximum, strain softening occurs and flow stress continuously decreases until fracture. This is not seen in other test conditions and after reaching maximum flow stress the onset of fracture is quite rapid.

5.4 Conclusions

(1) Bending reverse bending deformation was applied to 0.75 mm (hot rolled and annealed) and 2.5 mm thick (as-received H-24 condition) AZ31 Mg sheets at warm temperatures.

(2) In 0.75 mm thick sheet, fine grain structure of ~ 3 μm evolves in near surface regions after 1500 BRB cycles performed at 200^{o}C cycles; while an equiaxed coarse grain structure ~ 10 μm was observed in the mid-surface region.

(3) Grain growth was observed during BRB processing at temperatures > 200^{o}C. Temperature range of ~ 180^{o}C was found to be better suited for performing BRB cycles.

(4) A ~ 4 μm grain size was produced in AZ31 Mg by 1000 BRB cycles, performed at 180^{o}C. The broader distribution of basal texture around normal direction was achieved in the BRB processed Mg. The intensity of basal poles was found to decrease with increasing BRB deformation cycles.

(5) Hot rolling experiments were performed on BRB-processed (180^{o}C/ 1000 cycles) samples. It was shown that BRB processed samples can be successfully hot rolled at warm temperatures between 200-225^{o}C. A ~ 2 μm grain size was produced in BRB-processed samples after warm rolling.

(6) Room-temperature tensile tests indicate significant improvement in strength can be achieved in AZ31 Mg without compromising on ductility, after bending reverse-bending and warm rolling. However, AZ31 Mg alloy still exhibits lower strength levels as compared to ZK60 Mg processed by friction stir processing or by alternate biaxial corrugated pressing.

(7) Elevated temperature tensile tests demonstrate improvement in warm formability of processed material. High tensile elongations of > 200% can be achieved in BRB-processed and hot rolled Mg at strain rate of 2 x 10^{-4} s^{-1}.

(8) The improved mechanical properties of BRB-processed and hot rolled sheet is a direct consequence of a finer grain size and weaker and a more dispersed basal texture.

Table 5.1 Nominal composition range of as-received AZ31 Mg (in wt. %)

Al	Mn	Zn	Mg
3-3.6 %	0.6	1.0	Bal.

Table 5.2 Mechanical properties of as-received and as-processed AZ31 Mg

Materials	**Thickness (mm)**	**G.S (µm)**	**Y.S (MPa)**	**T.S (MPa)**	**e_f(%)**
As received –H24 (RD)	2.5	8	230	295	20
Hot rolled @ 200 ^{o}C + Annealed @ 375 ^{o}C/ 5hrs	0.75	25	135	215	13.5
BRB @ 200 ^{o}C C/ 1500 cycles	0.75	3 (finer grains)	180	275	15
BRB @ 200 ^{o}C C/ 1000 cycles + Warm rolled @ 200 ^{o}C	1	1.8	290	-	~1
BRB @ 200 ^{o}C C/ 1000 cycles + Warm rolled @ 200 ^{o}C	1	2	270	332	16

Table 5.3 Tensile elongation and fracture strain of as-processed fine grain AZ31 Mg at warm temperatures for selected strain rates.

Test Condition		**Tensile Elongation, %**	**Fracture Strain, ε_f**
Temperature, ^oC	**Strain Rate, s^{-1}**		
300	2×10^{-4}	162	1.0
350	2×10^{-4}	220	1.25
25*	5.5×10^{-4}	18.0	0.2

* Room temperature data included for comparison, RT test was a constant CHS test with initial strain rate of 5.5×10^{-4}.

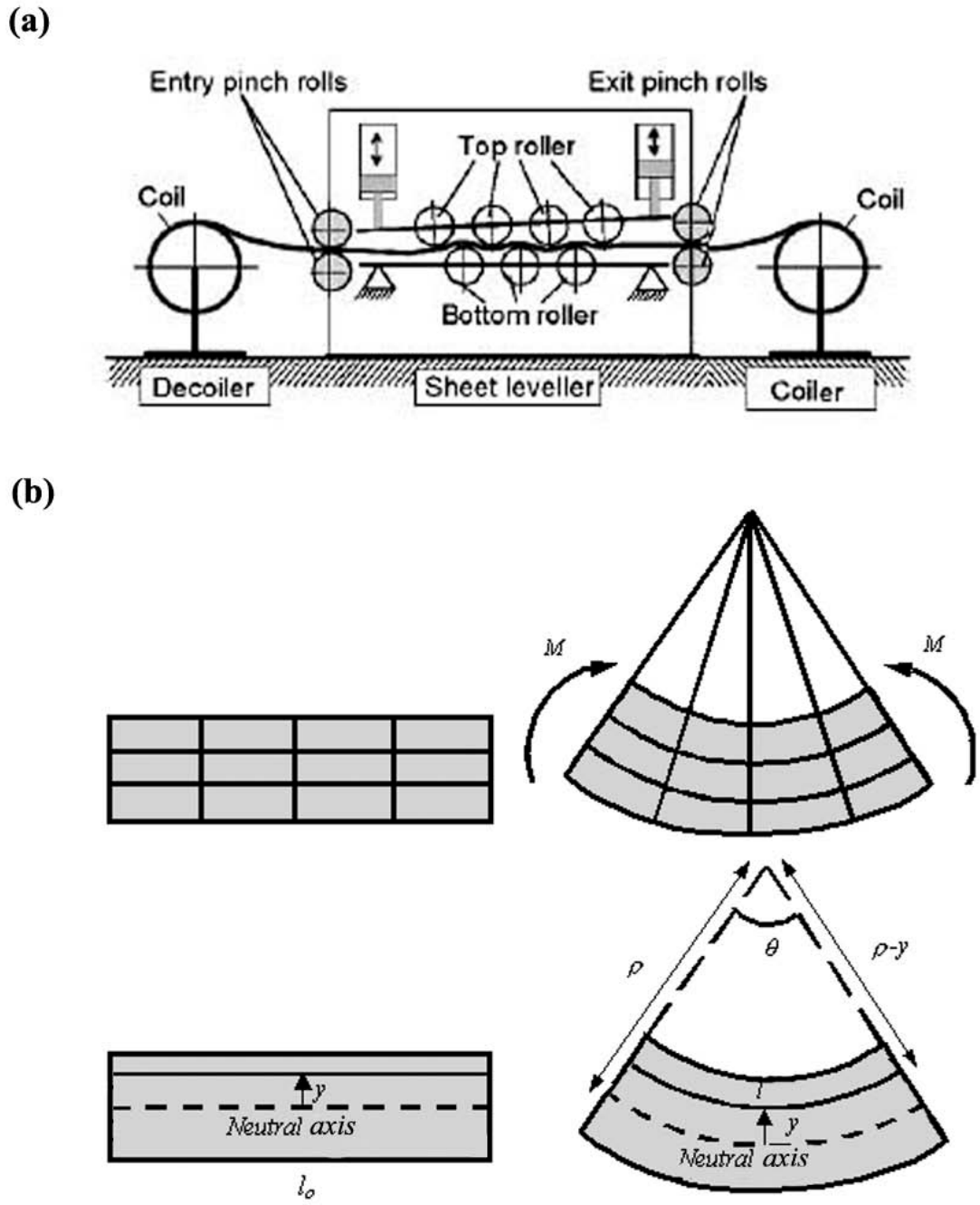

Figure 5.1 (a) Illustration of tension roller leveling process. (b) Sheet in pure bending.

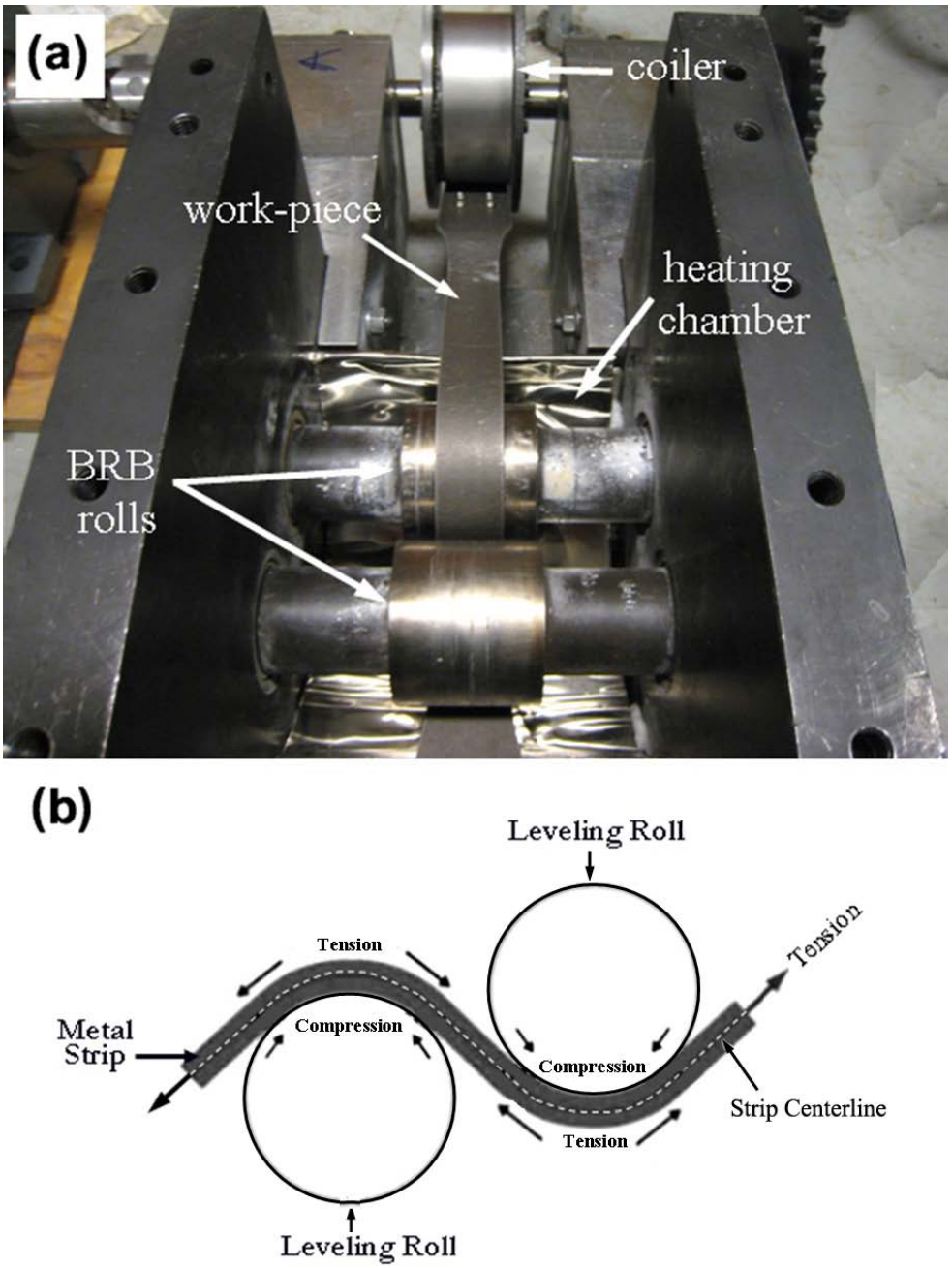

Figure 5.2 (a) Experimental bending reverse bending setup. (b) Details of strip geometry and loading while strip is in contact with the rolls.

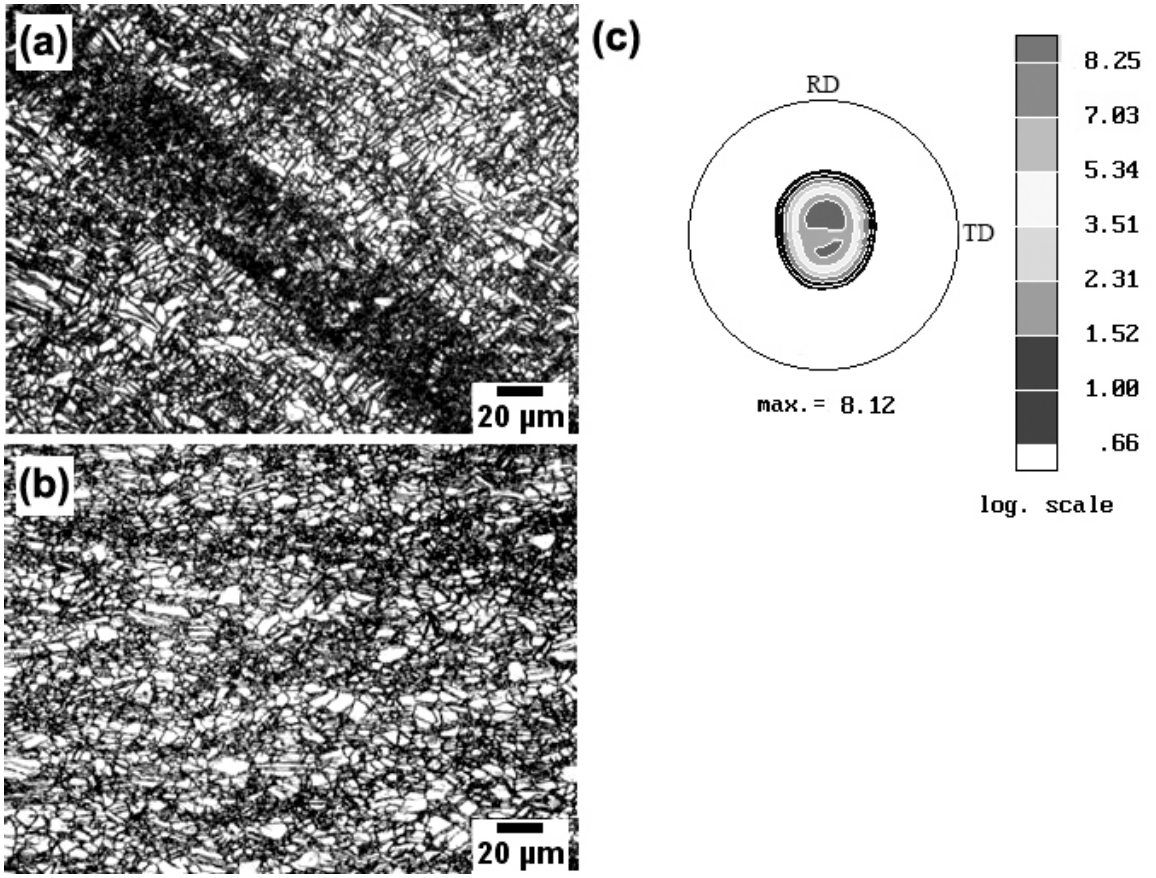

Figure 5.3 Microstructure of as-received AZ31-H24 Mg. In (a) microstructure of near-surface region shows fine grains inside shear bands and twinning in coarse grains. In (b) microstructure of mid-surface region shows relatively coarse grain microstructure. The average grain size of as-received AZ31 Mg is 8 µm. (c) {0002} experimental pole figure of the as-received material (RD up and TD right).

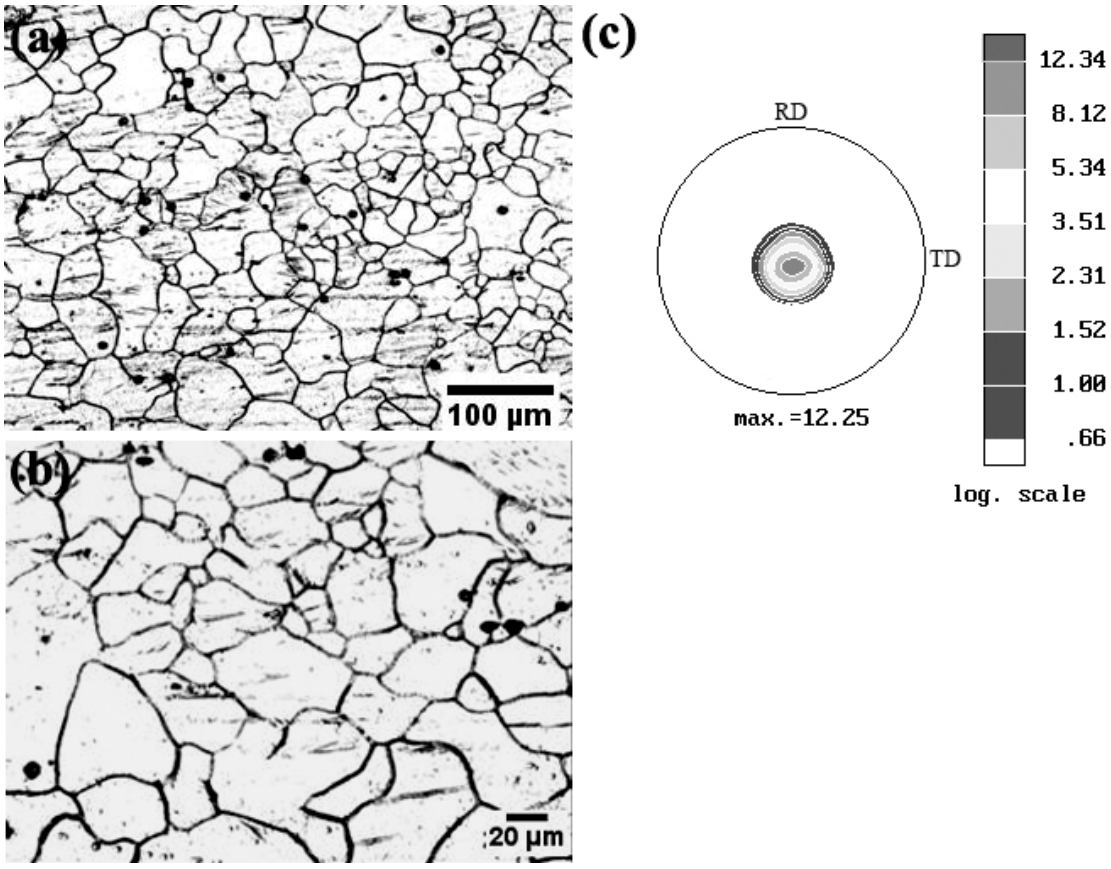

Figure 5.4 Microstructure of 0.75 mm thick hot rolled and annealed AZ31 Mg. In (a) coarse grains evolve after hot rolling at 350 ^{o}C and annealing at 375 ^{o}C / 5hr. (b) The structure is relatively homogenous in the ND-RD cross-section. . The average grain size is 25 µm. (c) {0002} experimental pole figure of the hot rolled and annealed sample.

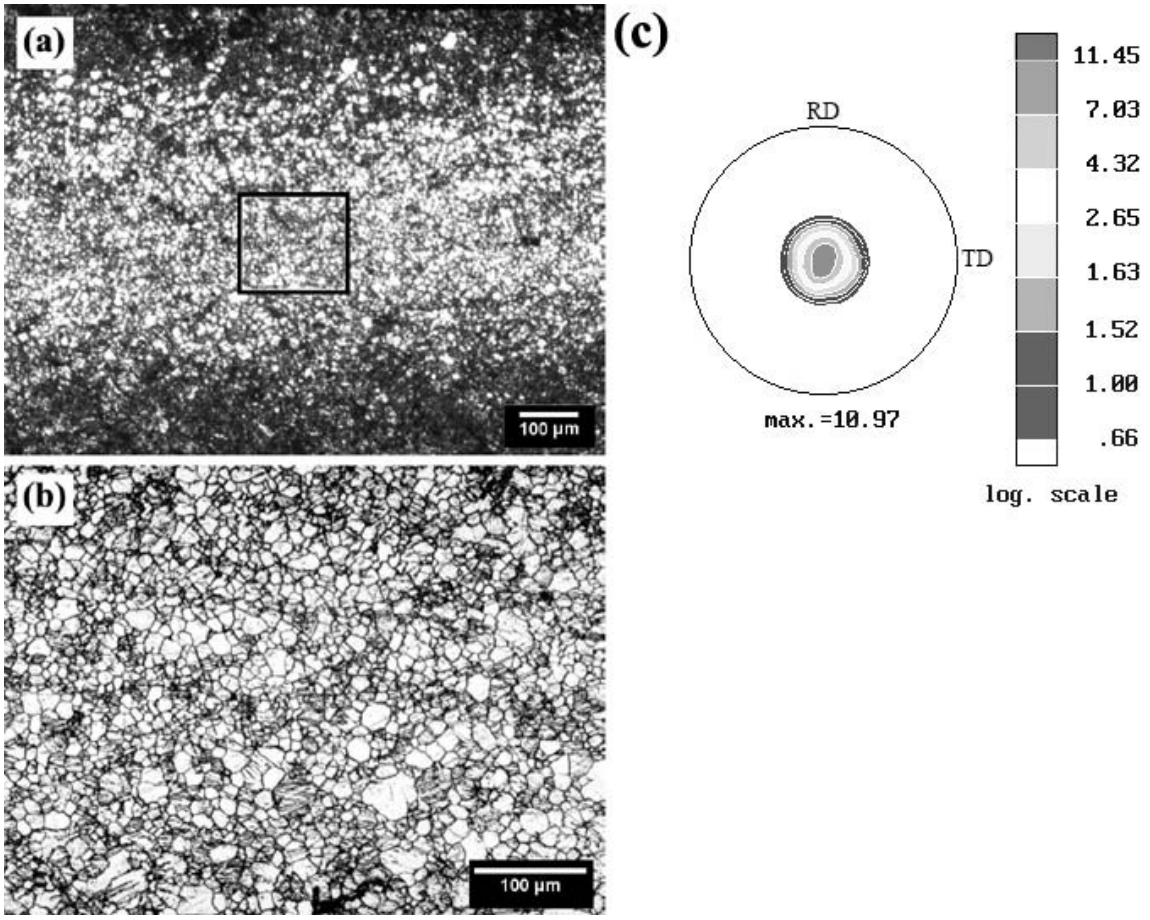

Figure 5.5 Microstructure of 0.75 mm thick hot rolled and annealed strip processed at 200^{o}C by 2000 bending reverse bending cycles. (a) Fine grain structure with 3 µm average grain size evolves in the near-surface regions; while (b) higher magnification image in (b) shows coarse grain structure (10 µm average size) in the mid-surface region of the strip after processing. (c) {0002} experimental pole figure of BRB processed sample.

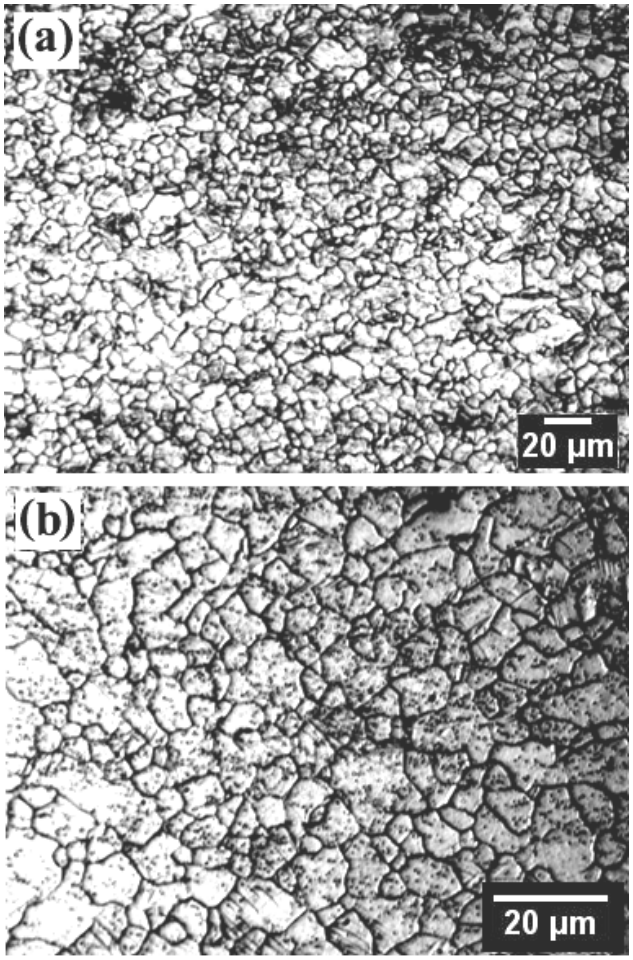

Figure 5.6 Microstructure of 2.5 mm thick AZ31 Mg BRB processed at 250^{o}C by 1000 bending reverse bending cycles. (a) Grain growth is evident in the structure; while higher magnification image in (b) shows coarse grain structure in the mid-surface region of the strip after BRB processing. The average grain size is 15 µm.

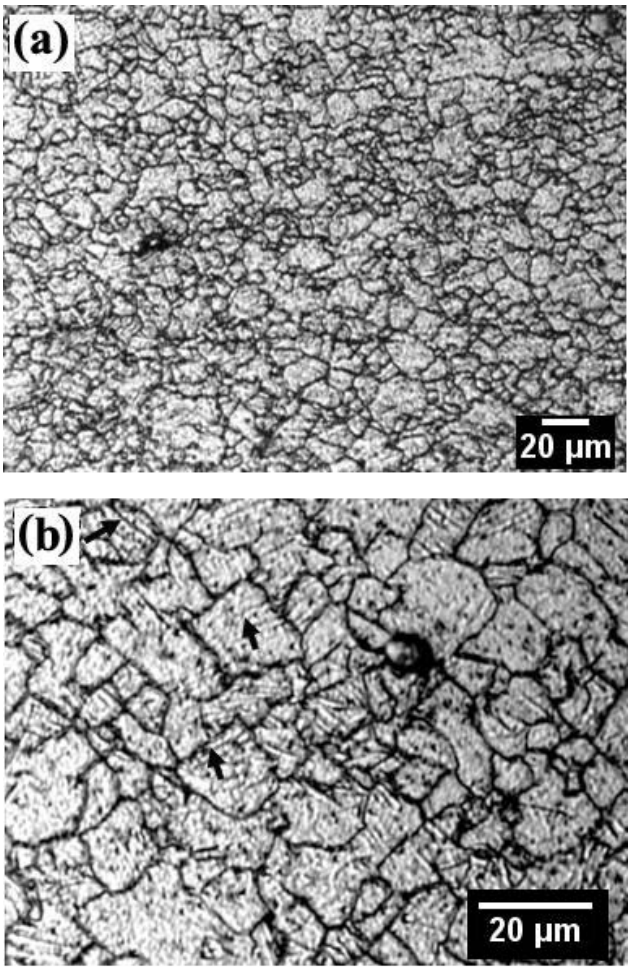

Figure 5.7 Microstructure of 2.5 mm thick AZ31 Mg BRB processed at 220^{o}C by 1000 bending reverse bending cycles. (a) Fine grain structure evolves in the near-surface regions; while (b) higher magnification image in (b) shows coarse grain structure in the mid-surface region of the strip after BRB processing. Twinning is observed in coarse grains as indicated by arrows. The average grain size is 10 μm.

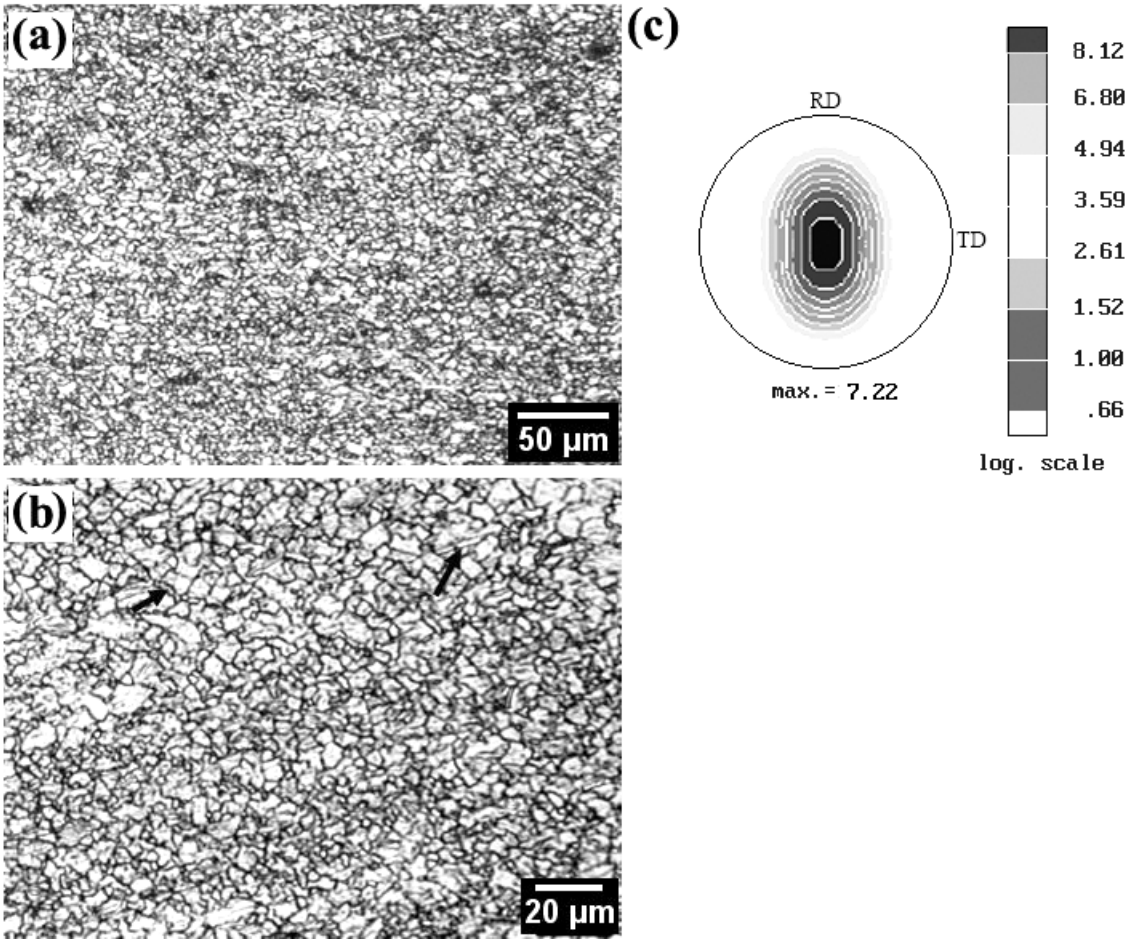

Figure 5.8 Microstructure of 2.5 mm thick AZ31 Mg BRB processed at 180^{o}C by 1000 bending reverse bending cycles. (a) Fine grain structure evolves in the near-surface regions; while (b) higher magnification image in (b) shows coarse grain structure in the mid-surface region of the strip after BRB processing, some twinning is also observed in the sample. The average grain size is 4 µm. (c) {0002} experimental pole figure of BRB processed sample.

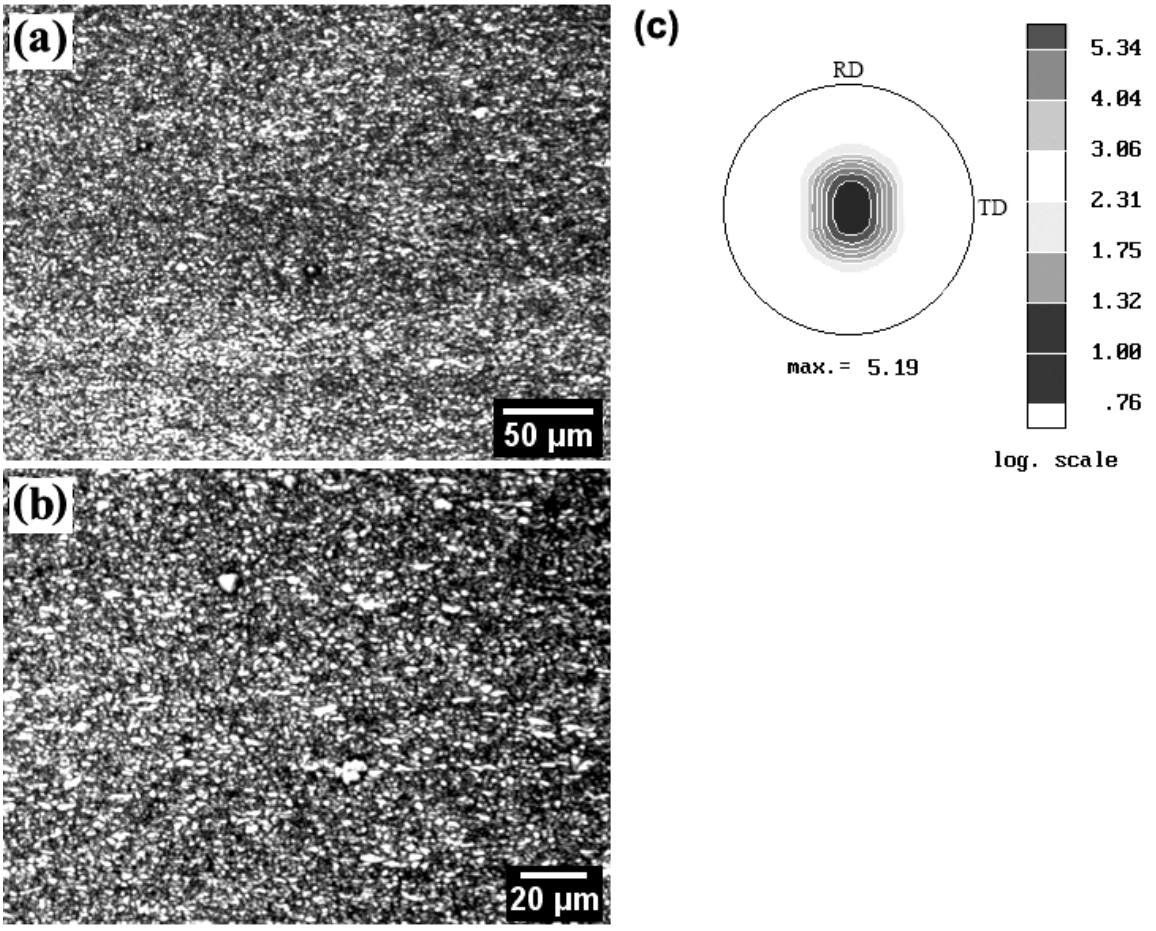

Figure 5.9 Microstructure of 1.0 mm thick as-processed AZ31 after warm rolling at 225^{o}C with true strain ε = 1.0 (a) Fine grain structure of 2 µm average grain size evolves in the sample. In (b) higher magnification micrograph shows that BRB refined grains have been further refined significantly along the rolling direction. Twinning was not seen and the over all grain structure is homogeneous. (c) {0002} experimental pole figure of BRB processed and warm rolled sample.

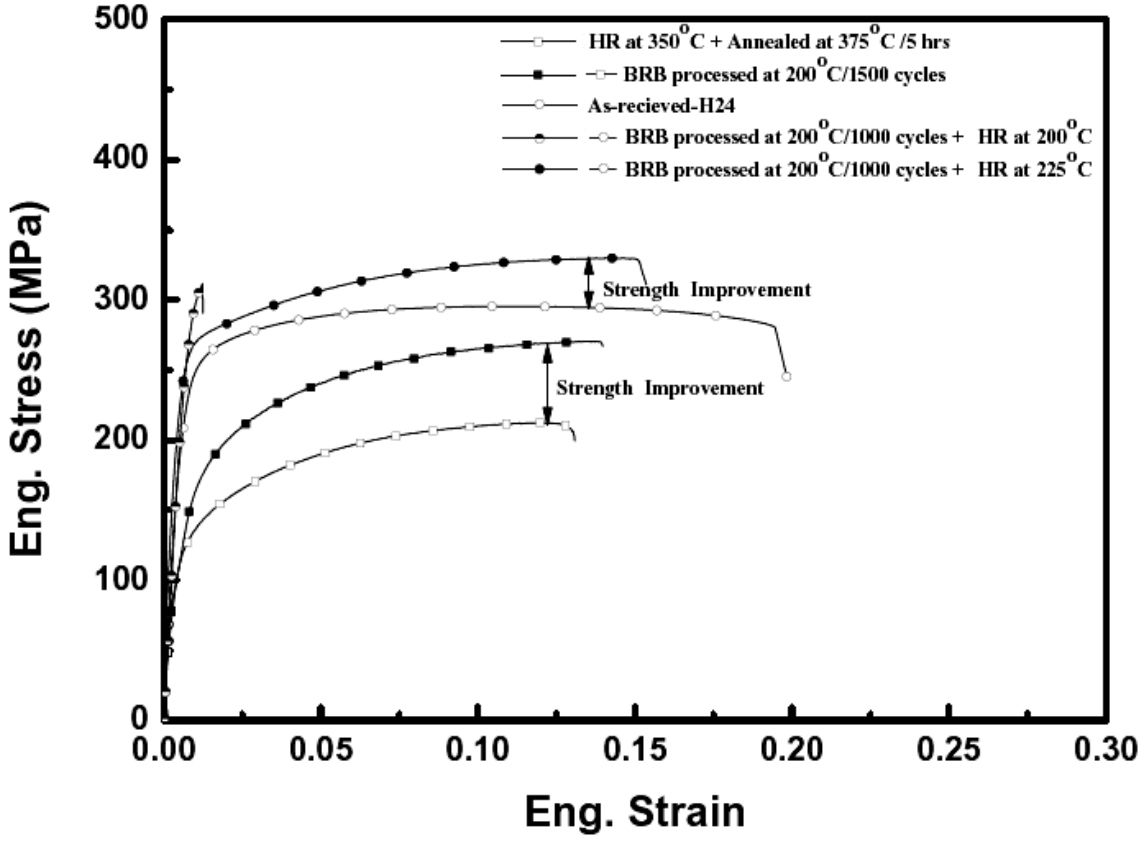

Figure 5.10 Room-temperature tensile stress–strain curves for as-received; BRB-processed and BRB-processed + warm rolled specimens.

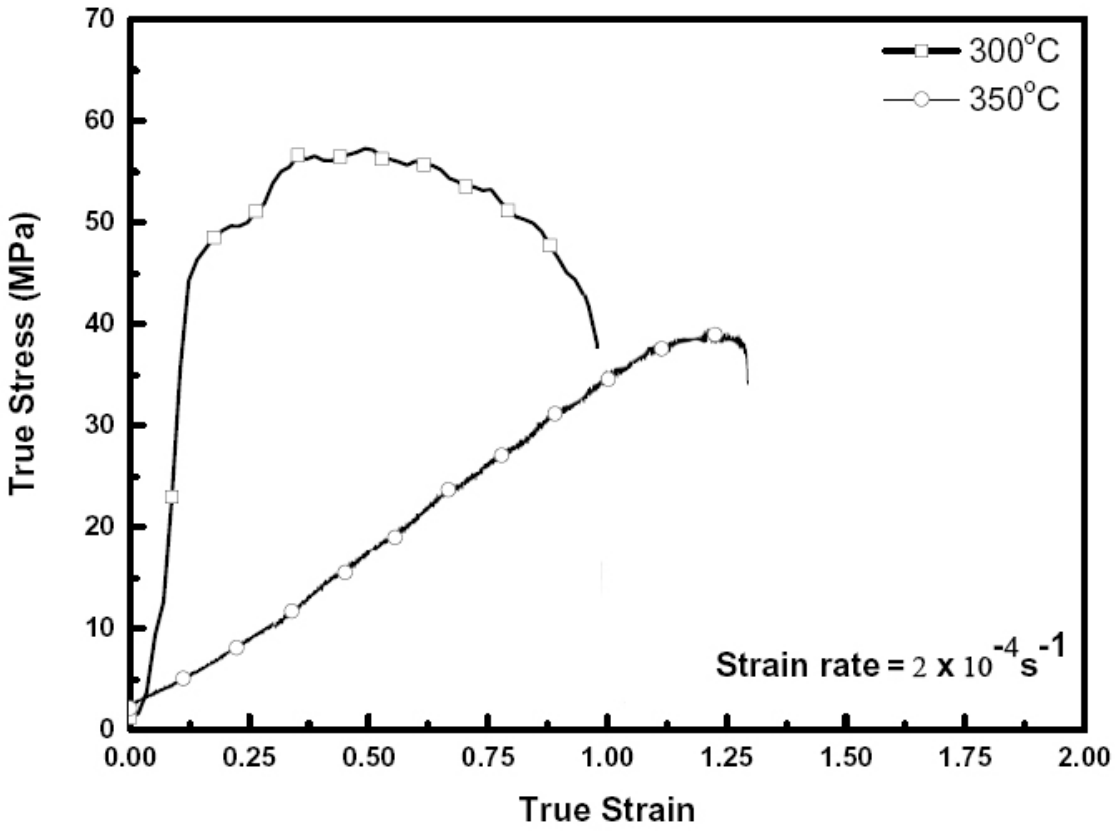

Figure 5.11 Elevated-temperature tensile stress-strain relationship of BRB processed and hot rolled AZ31 Mg alloy at selected test temperatures and strain rate.

5.5 References

[1] B.L. Mordike and T. Ebert: *Mater. Sci. Eng. A*, 2001, vol. 302, pp. 37–45.

[2] S. Schumann and H. Friedrich. *Mater. Sci. Forum* 419–422 (2003), p. 51.

[3] J. Goken, J. Bohlen, N. Hort, D. Letzig and K.U. Kainer. *Mater. Sci. Forum* 426–432 (2003), p. 153

[4] L. Riopelle, *JOM*, 48(1996), 44-46.

[5] S.H. Kim, B.S. You, C.D. Yim and Y.M. Seo, *Mater. Lett.* 59 (2005), pp. 3876–3880.

[6] A. Jager, P. Lukac, V. Gartnerova, J. Haloda and M. Dopita, *Mater. Sci. Eng. A* 432 (2006), pp. 20–25

[7] F.B. Kaiser, D. Letzig, K.U. Kainer, A. Sfyczynski and C. Hartig, *Adv. Eng. Mater.* 5 (12) (2003), pp. 891–896

[8] M.R. Barnett, M.D. Navea and C.J. Bettlesb, *Mater. Sci. Eng. A* 386 (2004), pp. 205–211.

[9] H.T. Jeong and T.K. Ha, *J. Mater. Process. Technol.* 187–188 (2007), pp. 559–561.

[10] F.B. Kaiser, D. Letzig, J. Bohlen, A. Styczynski, C. Hartig and K.U. Kainer, *Mater. Sci. Forum*
[11] D. Li, Q. Wang and W. Ding, *Mater. Sci. Forum* 546–549 (1) (2007), pp. 311–314.

[12] Q. Yang, A.K. Ghosh, *Acta Materialia*, 54 (2006), 5147-5158.

[13] E.A. Calnan, A.E.L Tate, *Institute of Metals -- Journal*, 79 (1951), p 455-464.

[14] T. Kusakabe, T. Hirasawa, *Nippon Kokon Kabushiki Kaisha -- Technical Report Overseas*, 7(1967), p 49-55.

[15] B.Takeaki, T. Minoru, T.Hideki *Sumitomo Light Metal Technical Reports*, 15(1974) p 31-40.

[16] T. Yoshiharu et al., *Technical Review - Mitsubishi Heavy Industries*, 22(1985), p 160-164.

[17] B. Mansoor, *Chapter. 1, PhD thesis*, University of Michigan, Ann Arbor, 2010.

[18] O. Duygulu and S. R. Agnew, *Magneisum Technology 2003*, p. 237-242.

CHAPTER 6

MICROSTRCTURE OF HIGH STRENGTH MAGNESIUM/ALUMINUM LAMINATED COMPOSITE PREPARED BY DEFORMATION PROCESSING

Abstract

A lightweight, high strength, laminated composite based on ZK60 Mg and A390 Al was produced by hot pressing and rolling. The mechanical properties of laminated composite were evaluated for a 17% volume fraction of A390 Al alloy. It was found that surface cleaning of layers and cold pressing of stack to seal interfaces prior to deformation processing was critical to achieve a strong bond between the sheets of hot rolled Mg and Al alloys. Increase in imparted strain and deformation temperatures resulted in extensive thinning and intermixing of laminate layers. Heat treatment of laminated composite at 350^{o}C under static conditions resulted in partial diffusion of constituent layers and development of high micro-hardness regions in the microstructure. Heat treatment under dynamic conditions at 450^{o}C resulted in reaction and complete dissolution constituent layers. A high micro-hardness core region with complex microstructure was created between ZK60 surface layers. Energy-dispersive X-ray spectroscopy identified 3 distinct intermetallics in the core region. Warm formability of hot rolled laminated composite sheet was demonstrated at 300^{o}C. Uniaxial tensile testing

showed that in heat treated condition the laminate was brittle and fractured without appreciable plastic deformation.

6.1 Introduction

There is great interest in Mg alloys and Mg based composites for potential use in aerospace, automotive and armor applications [1-6]. Magnesium alloys have a relatively low elastic modulus, *E,* compared to other metal alloys, which translates into a relatively high specific stiffness. In addition to that, the moderate strength of commercially available wrought magnesium alloy plate, coupled with relatively low density, translates into a specific strength that is roughly equal to aluminum armor alloys as shown in Fig. 1. Higher stiffness typically contributes to enhanced energy absorption upon ballistic impact [4], and there is a positive correlation between tensile strength and small arms ballistic performance in metal alloys [4]. Based on this information one may predict a possible benefit in wrought magnesium alloy armor applications. However, the specific strength of commercially available magnesium alloys is still not adequate for high performance armor applications. Therefore there is considerable interest in developing high strength Mg wrought alloys and Mg based composites for potential use in ballistic applications.

Recent advances in manufacturing technology have led to the development of magnesium based composites. Mg matrix composites have been manufactured by stir casting, power metallurgy and squeeze casting [6-15]. These composite have even greater potential to be used in high-performance aerospace and armor applications because of their high strength and wear resistance as compared to competitive engineering materials [15-22]. Despite of all these advantages, however, magnesium based composites normally exhibit limited ductility. It is therefore necessary to fabricate high strength magnesium-based

composites with adequate ductility and formability. This is the impetus for our initial investigations into the fabrication of high strength magnesium-based laminated composites with possible ballistic applications. Warm extruded ZK60 Mg which offers the best combination of strength and ductility among Mg wrought alloys was selected as the core material. The lamination was done by hot rolled aluminum-silicon alloy to possibility effect Mg solid solution and cause in-situ precipitation.

6.2 Experimental

6.2.1 Materials

The alloys used in this work were ZK60 Mg and A390 Al. The ZK60 Mg was received in 19mm thick extruded flat bar in T5 artificially aged condition. A390 Al alloy was received in the form of cast ingot. The nominal alloy composition range for both alloys is given in Table 1.

6.2.2 Stage-1 processing

Laminates of the two materials were prepared in stage-1 processing as shown in Fig. 1. A 38 mm x 38 mm square work-piece of 19 mm thickness was cut from ZK60 Mg flatbar; it was heated at 400^{o}C in a circular die for 30 mins and then pressed to make a 2 mm thick plate. An appropriate size strip was cut from hot-pressed plate and then hot rolled at 360^{o}C to get 0.5 mm sheet of ZK60 Mg alloy. Similarly for A390 Al alloy; a 25 mm x 25 mm square work-piece of 5 mm thickness was cut from ingot. It was heated at 420^{o}C inside a circular die for 30 mins and then hot pressed to make a 1 mm thick plate. The hot pressed A390 Al plate was then cut to appropriate size and hot rolled at 375^{o}C to get 0.15 mm thick foil. The hot rolled A390 Al is sometimes also referred to as Al-Si alloy in the text.

6.2.3 Stage-2 Processing

In stage-2 processing, surface cleaning of the laminate layers was done by cleaning with acetone, grinding with 1000 grid sand paper and abrading as shown in Fig. 2. After the cleaning operation alternate layers of ZK60 Mg and A390 Al alloy were arranged in a stack. The approximately 4.5 mm thick stack containing 7 ZK60 Mg and 6 A390 Allayers. The stack was then cold pressed to seal interfaces and remove any air between the layers. The stack was hot pressed at 400^{o}C in several steps to obtain a 2 mm thick sheet and a 0.4 mm thick foil of ZK60 Mg/ Al-Si laminated composite. In a separate set of experiments the 2 mm thick laminated composite sheet was pre-heated at 365 ^{o}C for 10 mins and then hot rolled to create a 0.5 mm thick foil.

6.2.4 Microstructure characterization

The microstructural examination of as-received, hot pressed, hot rolled and processed laminated composite was performed by using optical and scanning electron microscopy. Metallographic specimens were cold mounted in self-curing resin, fine ground and mechanically polished. ZK60 Mg alloys were etched with acetic-picral solution. The acetic-picral solution contains 4.2 g picric acid, 70 ml ethanol, 10 ml acetic acid and 10 ml distilled water. Al- 17% Si alloy were etched using Keller's Regent. XL30-FEG SEM was employed to observe the very fine microstructure at higher magnifications and EDAX analysis carried out at an operating voltage of 20-30 KV.

6.2.5 Heat treatment

Heat treatments were performed under static conditions and under applied load conditions on 2 mm thick laminated composite samples. The heat treatment under applied load was performed at 450^{o}C for 1 hr and the laminated composite was pressed from 2

mm to 0.5 mm. The heat treatments under static conditions were performed at 350 ^{o}C, 400 ^{o}C and 450^{o}C for different time durations with the goal to achieve in situ diffusion and intermetallic formation between adjacent laminate layers without compromising the integrity of the laminate.

6.2.7 Mechanical testing

Vickers hardness was measured with an indentation load of 300 g to determine hardness of at different processing stages for both alloys. The loading time was 15 seconds. The hardness value for the samples at every stages of deformation was obtained by averaging at least 10 measurements to achieve statistical reliability.

Room-temperature mechanical behavior of hot rolled ZK60 Mg, A390 Al and laminated composite was determined by tension tests. The tensile samples had 15 mm long x 3 mm wide gauge sections. The surfaces of tensile specimens were polished prior to testing. Tests were conducted using a computer-controlled 5505 Instron machine. A 12.7 mm gauge length extensometer, attached to the gauge length, was used to measure the tensile strain. Specimens were tested at a constant crosshead speed of 0.5 mm/min.

Biaxial forming tests were performed on hot rolled laminated composite by clamping a 0.4 mm thick sheet disc in a heated 12.5 mm dia circular die, and by blowing gas pressure from one side of the sheet to form hemispherical dome to evaluate biaxial formability. Tests were carried out at 300^{o}C. Though these tests gave a quick evaluation of the dome height the tests do not represent comparable conditions as uniaxial tensile tests. After forming the dome heights and forming limit strain at pole were measured by calipers.

6.3 Results

6.3.1 Microstructure evolution

(a) Stage-1 Processing

The microstructure of hot rolled ZK60 Mg with an average grain size of 8-10 μm is shown in Fig. 3. The structure is bimodal and has some 30-50 μm coarse grains; that are reminiscent of extrusion structure. The hot rolling operation was done at 360^{o}C with a true strain of ε = 1.4 (associated with thickness reduction). Fine grains are generated near the grain boundary of coarse grains which may indicate some degree of dynamic recrystallization during rolling [23].

The microstructural features of as-received A390 Al are shown in Fig. 4. The A390 Al is a hypereutectic Al-Si alloy and contains about ~17 wt.% Si. Its microstructure consists of small silicon (gray colored) particles oriented angularly in eutectic and large unrefined primary Si particles in matrix of aluminum solid solution. The needle like lamellar structure is 70-150 μm long along the major axis and 4-10 μm long along the minor axis respectively. Several distinct morphologies of coarse unrefined Si particles are present in the structure. In Fig. 5 optical micrograph shows the overall microstructure of 0.05 mm thick, hot rolled A390 Al foil. The hot rolling operation was done at 425^{o}C with a true strain of ε = 1.9 (associated with thickness reduction). Hot rolling results in break down of coarse Si particles and distributes them randomly in the structure. The average size of Si particles is approximately 10 μm, but no needle like lamellar structure is observed in hot rolled condition. Some large unrefined primary Si particles of average size 16-20 μm are also present in Al matrix. Over all it was important to sub-divide and distribute Si particles in Al foil. This may lead to the formation of $MgSi_2$ in the laminated composite and improve mechanical properties of composite.

Vickers data for stage-1 processing are presented in Table 2 and 3. In the hot rolled condition the micro-hardness of ZK60 Mg is 76 which is significantly higher than as-received condition hardness of 62. However, for A390 Al alloy hot rolled condition micro-hardness of 64 is lower than as-cast condition micro-hardness of 73.

(b) Stage-2 Processing

In Fig. 6 microstructure of 2.0 mm thick ZK60/Al-Si laminated composite is shown after pressing at 400 ^{o}C with true strain of $\varepsilon = 0.8$. In (a) distinct layers of ZK60 Mg and Al-Si alloy are indicated by arrows. It must be noted that the Al-Si alloy layers have relatively uniform size and they did not thin extensively at this stage. In (b) optical micrograph shows a void and defect free interface between adjacent laminate layers. The average grain size ZK60 Mg layer is ~5 μm at this stage. The average thickness of each ZK60 Mg and Al-Si alloy layer is approximately 120 μm and 40 μm respectively. The inter-layer interface region is free of cracks or voids. Also no reaction products are seen under optical microscopy. In Fig. 7 Microstructure of 0.4 mm laminate after pressing at 400 ^{o}C with true strain of $\varepsilon = 2.5$. In (a) distinct layers of ZK60 Mg and Al-17%Si alloy are indicated by the arrows. Average grain size of ZK60 Mg is 5μm. Note that the layer to the right has sheared after thinning close to the coarse ZK60 Mg grain (indicated by circle). In (b) the Al-Si foil layers are wavy and intermixed and they show thinning around coarse silicon particles and coarse primary grains in the adjacent ZK60 Mg layers. Necking of Al-Si layers is indicated by arrows. The hardness data for laminated composite in different conditions is given in Table 4. After stage-2 processing the hardness for ZK60 Mg and Al-Si alloy layers is 75 and 69 respectively. While the hardness for interface region between the two materials is 84.

(c) Hot rolled laminate

Fig. 8 shows microstructure of 0.5 mm thick laminate after hot rolling at 365 ^{o}C with strain of ε = 1.4. In (a) distinct layers of ZK60 Mg and Al-Si alloy are indicated by the arrows. Average grain size of ZK60 Mg is ~3 μm. In (b) the layers of Al-17% Si show uniform thinning in most places, except around Si particles. The layers show bending around coarse primary grains of adjacent ZK60 Mg layers, but no intermixing of Al-Si layers is observed as was observed in hot pressed alloy. In hot rolled condition the hardness of laminated composite shows significant increase. The hardness of ZK60 Mg layers (3.7 μm) is 100 and the interface region hardness is even higher.

(d) Heat treatment

Under static conditions the high temperature heat treatment resulted in extensive reaction between constituent layers and the material became very brittle. The low temperature condition of 350^{o}C showed some better results. Fig. 9 shows the microstructure of ZK60 Mg / Al-17% Si laminated composite heat treated at 350^{o}C for 6 hrs. The (darker contrast) ZK60 layers have partially diffused in to the (lighter contrast) Al-17%Si alloy. (b) There is also some evidence suggesting formation of Mg-Si intermetallic in the vicinity of Si particles. Not much change in ZK60 layer hardness was observed while two regions of high hardness are identified. Some voids are also near interface region between different material layers.

Fig. 10 shows the microstructure of laminated composite after heat treatment at 450 ^{o}C for 1 hr under an applied load. The laminate was hot pressed to ~ 0.4 mm thickness at 450 ^{o}C with a true strain of ε = 1.6. After heat treatment, no individual Al-Si or ZK60 Mg layers are visible in the microstructure. A reacted region between surface ZK60 layers is also identified. The interface between ZK60 Mg surface layer and reacted

region shows some fine Mg grains. High magnification SEM pictures show several regions with distinct microstructure and appearance in the reacted core.

Fig. 11 shows the reacted core region microstructure. In Fig. 11 (a) & (b) regions of distant structure and micro-hardness are identified in the reacted core. EDXS analysis on these selected regions done at 15 kV identified presence of different intermetallics. In (b) higher magnification shows unique microstructure corresponding to highlighted region in (a) that was observed in the reacted region. Some Zr particles were also present in the microstructure (indicated by arrows). The hardness of laminate after heat treatment under static and dynamic conditionally showed similar trends. Heat treatment under applied load resulted in some increase in the hardness of the ZK60 surface layers, while inside the reaction area, two distinct regions with high micro-hardness of 268 and 154 respectively were identified as previously shown in Fig. 11.

6.3.2 Mechanical properties

The room-temperature mechanical property data are presented in Table 5. Uniaxial testing indicates that the laminated composite showed reasonable mechanical properties in hot rolled condition. Biaxial forming also showed encouraging results. The hot pressed 0.4 mm thick laminated composite was biaxially formed under gas pressure in a die at 360^{o}C. Dome height of 5.2 mm was achieved under a pressure of 350 psi in under 2mins. A forming limit strain of ε_{limit} = 0.32 was calculated for the hemispherical dome. However, in the heat treated and high hardness condition the material became very brittle and fractured without much plastic deformation. This indicates that the void formation during heat treatment adversely affect the mechanical properties. Additionally, the

discontinuous precipitation and reaction between Si particles and ZK60 matrix leads forms brittle interface between layers.

6.4 Discussion

In general, the plastic instabilities caused by different flow properties of constituent materials make the harder phase to neck and finally rupture during the co-deformation of dissimilar metals [23]. ZK60 Mg layers preserved their coherency in most of the regions during the laminate processing while Al-Si layers necked down, become wavy and then finally sheared. Similar results have been observed in accumulative roll bonding of Mg alloys and composites [24] and [25]. Grain refinement was observed in Mg layers after stage-2 processing and hot rolling. This noticeable refining effect on Mg layers can be attributed to the severe plastic strain imparted during deformation and rolling. After heat treatment several intermetallic compound were identified as composted of Mg-Al-Si, Mg-Zr-Si and Mg-Al in the reacted region, but their exact composition is not known at this time. The formation mechanism of the intermetallic compound in reacted region is similar to diffusion bonding which includes plastic deformation, diffusion followed by bonding [26,29]. Furthermore, straining during heat treatment accelerated the diffusion processes. Several researches have found that high strain during rolling could accelerate the diffusion between different layers of the multi-layered composite and enhance the formation of intermetallic compounds [30,31]. Accelerated diffusion kinetics during high temperature heat treatment with high strain causes intermetallic compounds to grow rapidly in core region. The individual layers disappeared and the core region become very brittle and then fractured easily during tensile testing.

Normally, the tensile strength of the multi-layered composite is decided by the flow stresses of both constituents according to the rule of mixture [32-34]. Especially, in the hot rolled composite, necking and rupture will occur in hard region because of the instabilities originating from the differences in mechanical properties of constituent layers. Thus, the tensile properties depend on the flow properties of the constituent phases and work hardening rate of soft phase, which supports the load to resist more deformation around the neck [35]. In summary, encouraging results were obtained with respect to bonding between constituent materials layers and development of high micro-hardness in reacted core. However, the choice of A390 Al is not suitable for controlled in-situ precipitation of high-hardness Mg-Si intermetallic particles. The reaction between Si-particles and Mg matrix was severe even for the 17% volume fraction of Al-Si alloy and an entire intermetallic core region was created. A choice of an Al alloy with homogeneously distributed fine Si particles (< 1 μm) may be ideal for laminating Mg alloys. Nevertheless, achievement of high microhardness in core region indicates that by optimizing the selection of Al alloy, one may be able to create high strength Mg/Al laminated composite with adequate ductility by influencing Mg solid solution and intermetallic formation.

6.5 Conclusions

(1) Laminate composite fabrication by deformation processing is demonstrated using hot rolled ZK60 Mg and A390 Al foils. A crack and void free composite is fabricated with layer thicknesses of 120 μm and 40 μm for ZK60 Mg and 17 volume % Al-Si alloy respectively.

(2) It is shown that surface cleaning and abrading of individual layers prior to stacking and cold pressing of stack to seal interfaces is critical for achieving strong bond between successive layers.

(3) The layer interface between ZK60 Mg and Al-Si alloy is unstable under large deformation strains due to different flow properties. This instability is manifested as waviness during hot pressing and hot rolling operations. The Al-Si alloy laminate layers intermix and even in some cases encase the ZK60 Mg layers.

(4) Heat treatment under applied load creates a reacted core region in the laminate and the individual ZK60 Mg and A390 Al layers disappear. The reaction area has two distinct regions of high micro-hardness.

(5) It is shown that hot rolling operation can be used to create a thin sheet from the laminate. The Biaxial forming of hot rolled laminated composite demonstrates its warm forming capability. It may also suggest possibility of superplastic forming.

(6) Mechanical testing of heat treated laminated composite did not yield use-able data as the brittle interfaces lead to premature failure without much plastic deformation. The % volume fraction of Al alloy and distribution and size of Si particles must be adjusted to achieve high strength and adequate ductility in the laminated composite.

Table 6.1 Nominal composition range of alloys used in (wt. %).

ZK60 Mg (wt. %)					
Zn	**Zr**		**Impurities**		**Mg**
4.8-6.2	0.45		< 0.3		Bal.
A390 Al (wt. %)					
Si	**Cu**	**Mg**	**Mn**	**Fe**	**Al**
15-17	4-5%	0.45 to 0.65	0.1 max.	1.3 max.	Bal.

Table 6.2 Vickers microhardness of ZK60 Mg during stage-1 processing.

Condition	**HV**	**g.s(μm)**	**region**
As-received	62	13	fine grains
	61	100-300	coarse grains
Hot Pressed	54	35	finer grains
Hot Rolled	76	5	finer grains

Table 6.3 Vickers microhardness of A390 Al during stage-1 processing.

Condition	**HV**	**Thickness (mm)**	**region**
As-received	73	50	Al matrix
Hot Pressed	56	2	Al matrix
Hot Rolled	64	0.15	Al matrix

Table 6.4 Vickers microhardness of laminated composite at different stages.

Condition	Temperature (^{o}C)	HV	Laminate thickness (mm)	Region
Hot Pressed	400	74	0.4	ZK60 layer
		69		Al-Si layer
		85		Interface
Heat treatment under applied load	450	75	0.5	ZK60 layer
		154		Reacted region-1
		268		Reacted region-2
Heat treatment under static conditions	350	85	1.0	ZK60 layer
		142		Reacted region-1
		269		Reacted region-2
Hot Rolled	375	100	0.5	ZK60 layer
		105		Interface

Table 6.5 Mechanical properties of hot rolled alloys and laminated composite.

Materials	Thickness (mm)	Y.S (MPa)	T.S (MPa)	e_f(%)
Hot rolled ZK60 (RD)	0.5	180	250	20
Hot rolled A390 Al (RD)	1.5	190	215	5
Hot rolled Laminated composite (RD)	0.5	215	260	11

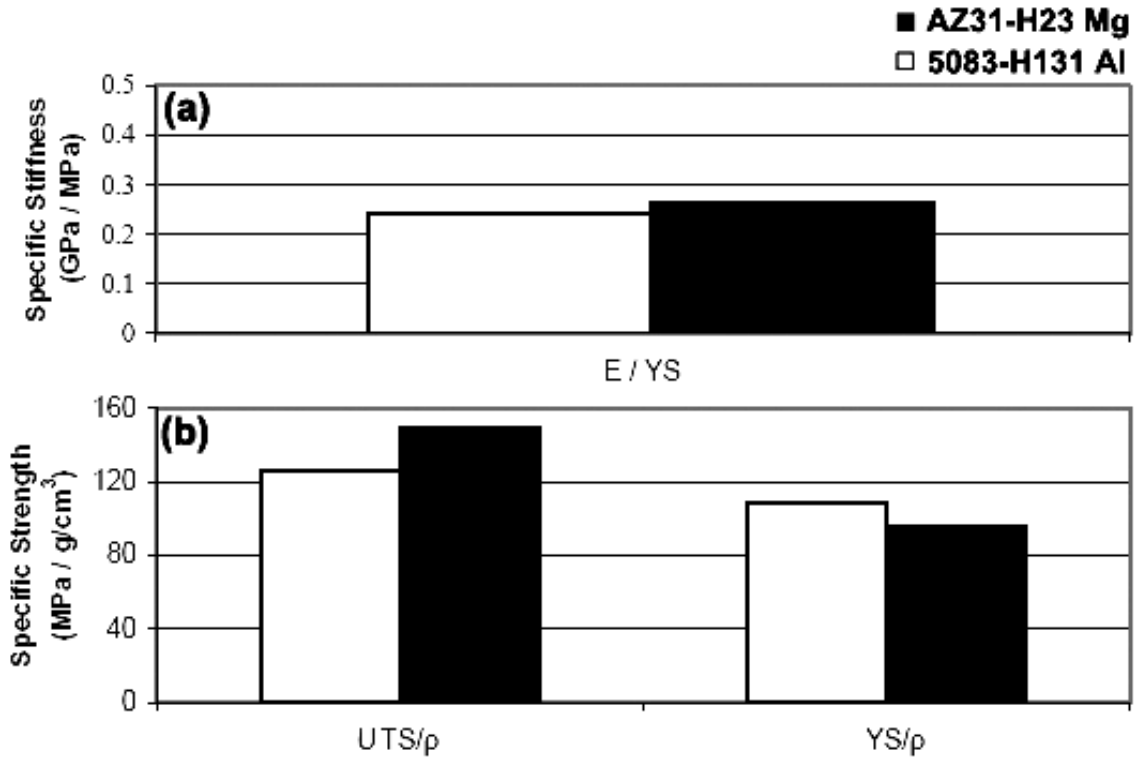

Figure 6.1 Specific stiffness and strength of commercial Mg alloy plate versus Al alloy armor plate.

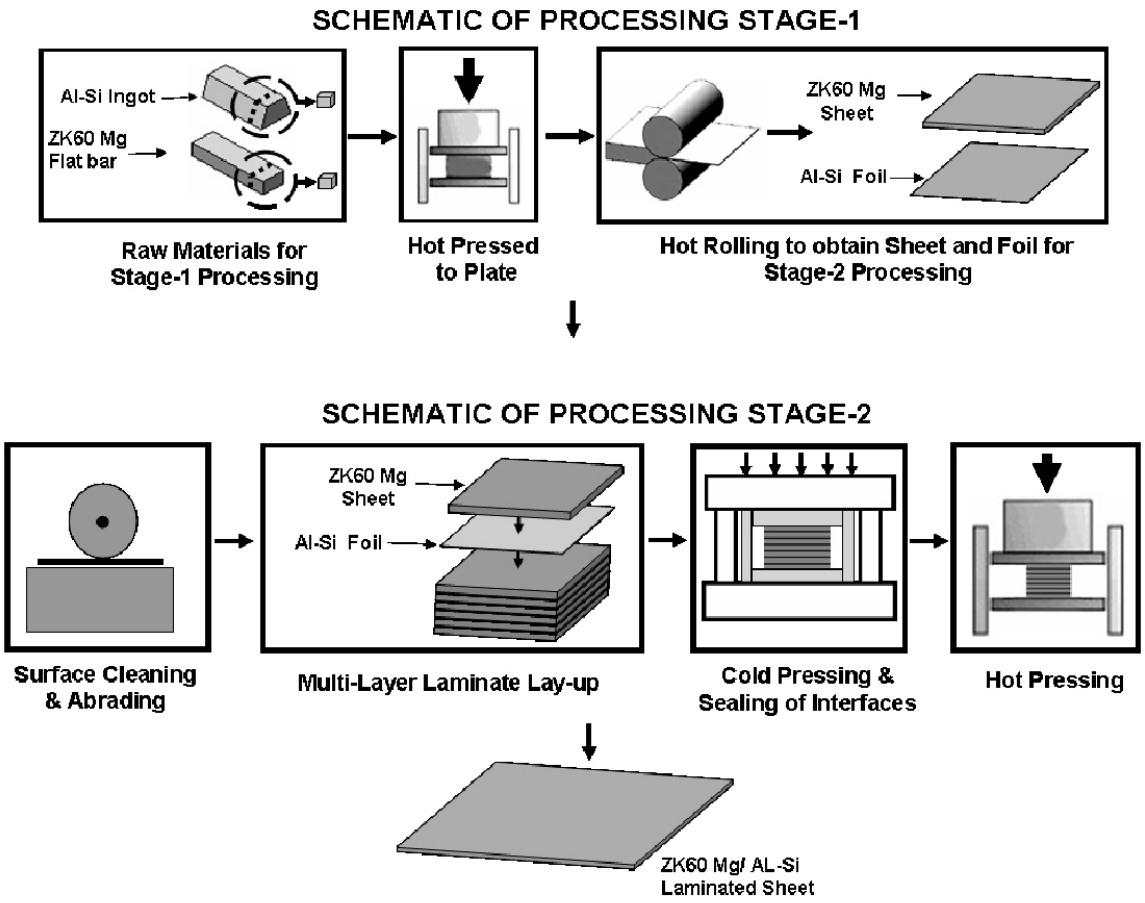

Figure 6.2 Schematic illustration of the various steps involved in the fabrication of Al-Si alloy foil laminated ZK60 Mg composite.

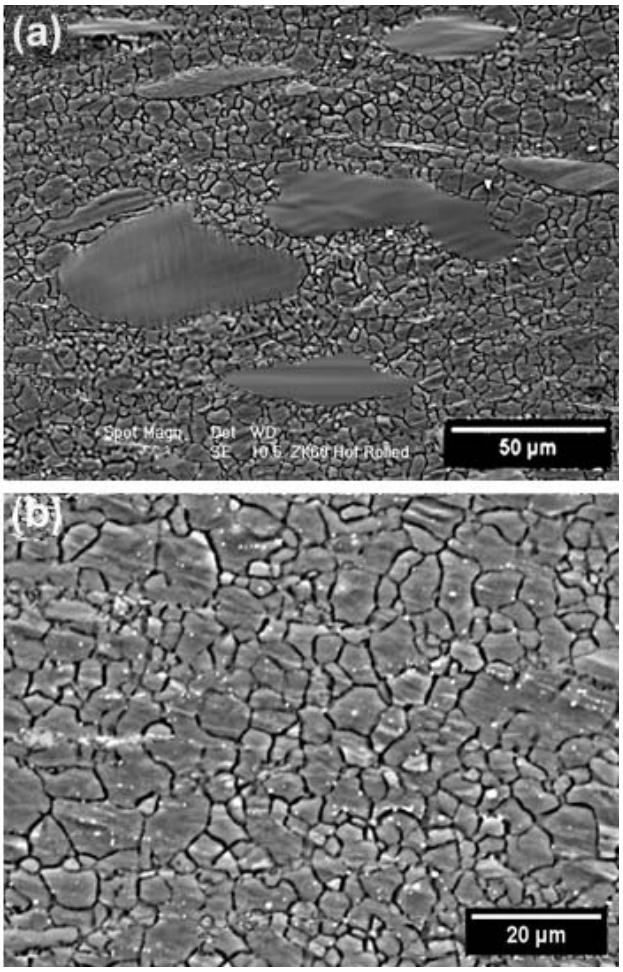

Figure 6.3 Microstructure of 0.5mm thick ZK60 Mg sheet, hot rolled at 365^{o}C with true strain of $\varepsilon = 1.4$ (thickness reduction). (a) The average grain size is 8-10 µm; the structure is not uniform and has some coarse grains that are reminiscent of extrusion structure. (b) Fine grains are generated near the grain boundary of coarse grains.

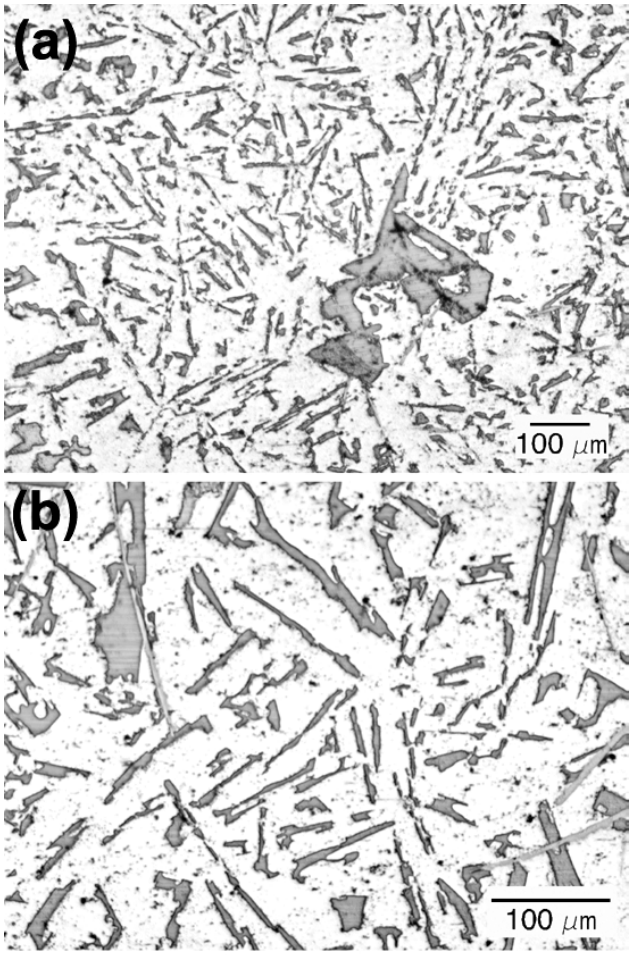

Figure 6.4 Microstructure of A390 Al. It consists of small, angularly oriented needle like silicon particles in eutectic and large unrefined primary particles in matrix of aluminum solid solution. The needle like lamellar structure is 70-150 μm long along major axis and 4-10 μm long along minor axis. Several distinct morphologies of unrefined Si particles are observed.

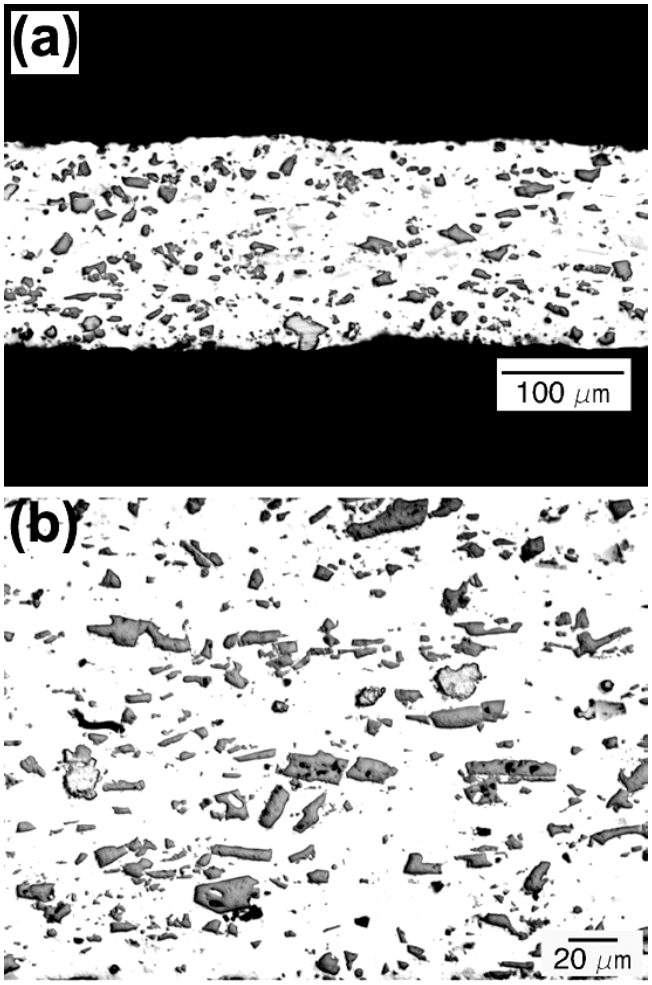

Figure 6.5 (a) The overall microstructure of 0.05mm thick, hot rolled A390 Al foil. The hot rolling operation was done at 425^{o}C with true strain of ε = 1.9 (associated with thickness reduction). In (b), good Si particles distribution is observed. These particles are about 10 μm in size. Some large unrefined primary Si particles of average size 16-20 μm are also present in Al matrix.

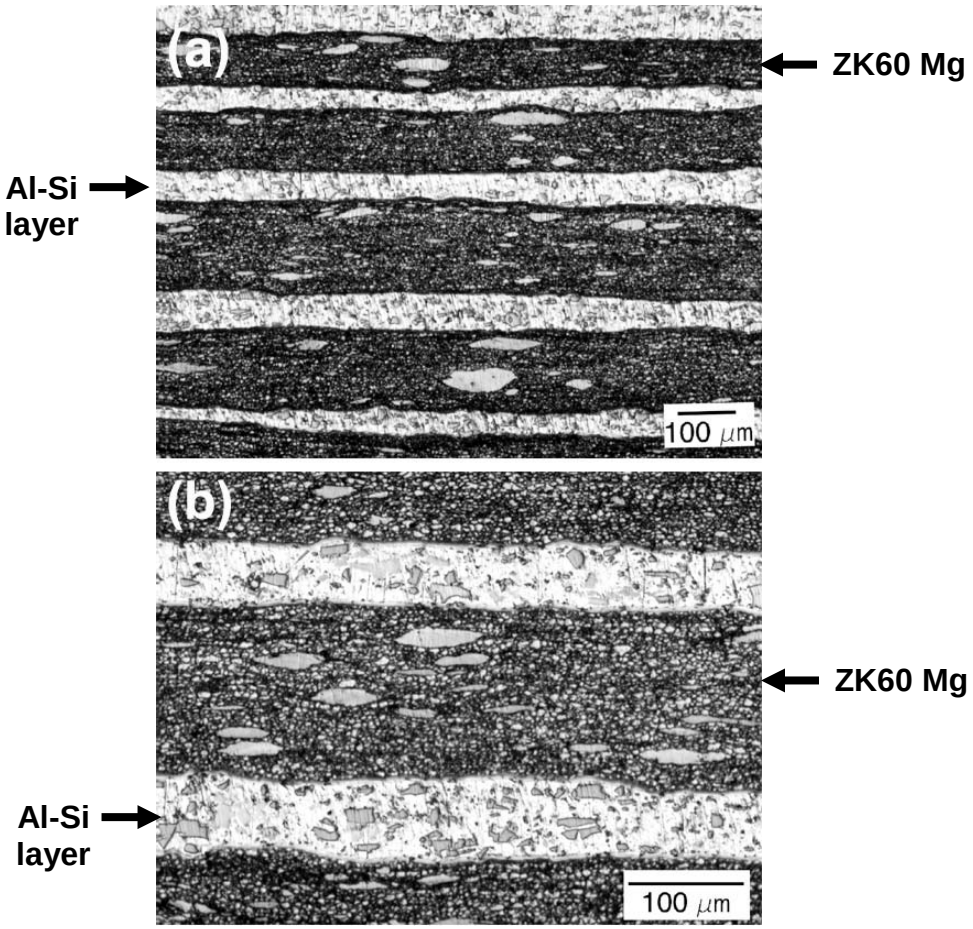

Figure 6.6 Microstructure of 2.0 mm thick ZK60/Al-Si laminated composite after pressing at 400 ^{o}C with true strain of $\varepsilon = 0.8$. In (a) distinct layers of ZK60 Mg and Al-Si alloy are indicated by arrows. It must be noted that the Al-Si alloy layers have relatively uniform size and did not thin extensively at this stage. In (b) a void and defect free interface between laminate layers is observed. The average grain size for of ZK60 layers is ~5 μm at this stage.

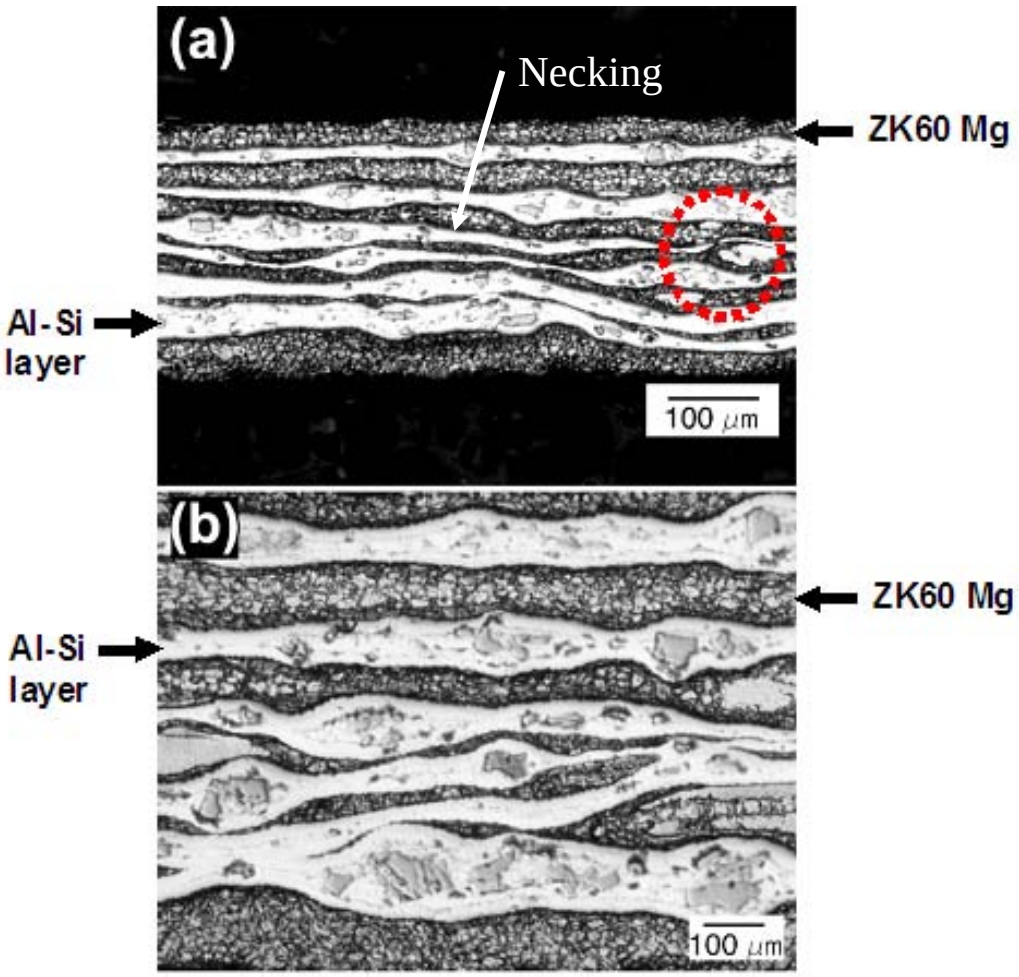

Figure 6.7 Microstructure of 0.4 mm laminate after pressing at 400 ^{o}C with true strain of $\varepsilon = 2.5$. In (a) distinct layers of ZK60 Mg and Al-Si alloy are indicated by the arrows. Average grain size of ZK60 Mg is 5μm. Note that the layer to the right has sheared after thinning close to the coarse ZK60 Mg grain (indicated by circle). In (b) the Al-Si foil layers are wavy and intermixed and they show thinning around coarse silicon particles and coarse primary grains in the adjacent ZK60 Mg layers. Necking in Al-Si layers is indicated by arrows.

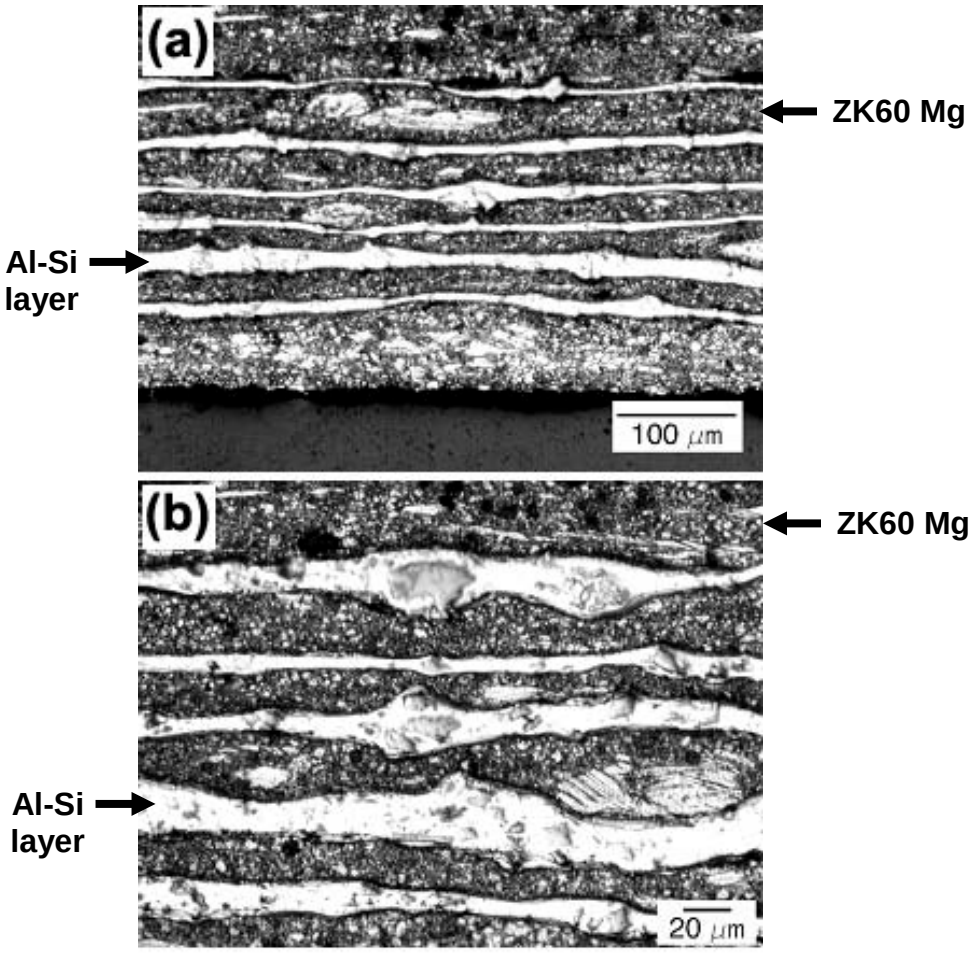

Figure 6.8 Microstructure of 0.5 mm thick laminate after hot rolling at 365 ^{o}C with strain of ε = 1.4. In (a) distinct layers of ZK60 Mg and Al-Si alloy are indicated by the arrows. Average grain size of ZK60 Mg is ~3 μm. In (b) the layers of Al-17% Si show uniform thinning in most places, except around Si particles. The layers show bending around coarse primary grains of adjacent ZK60 Mg layers, but no intermixing of Al-Si layers is observed as was observed in hot pressed alloy.

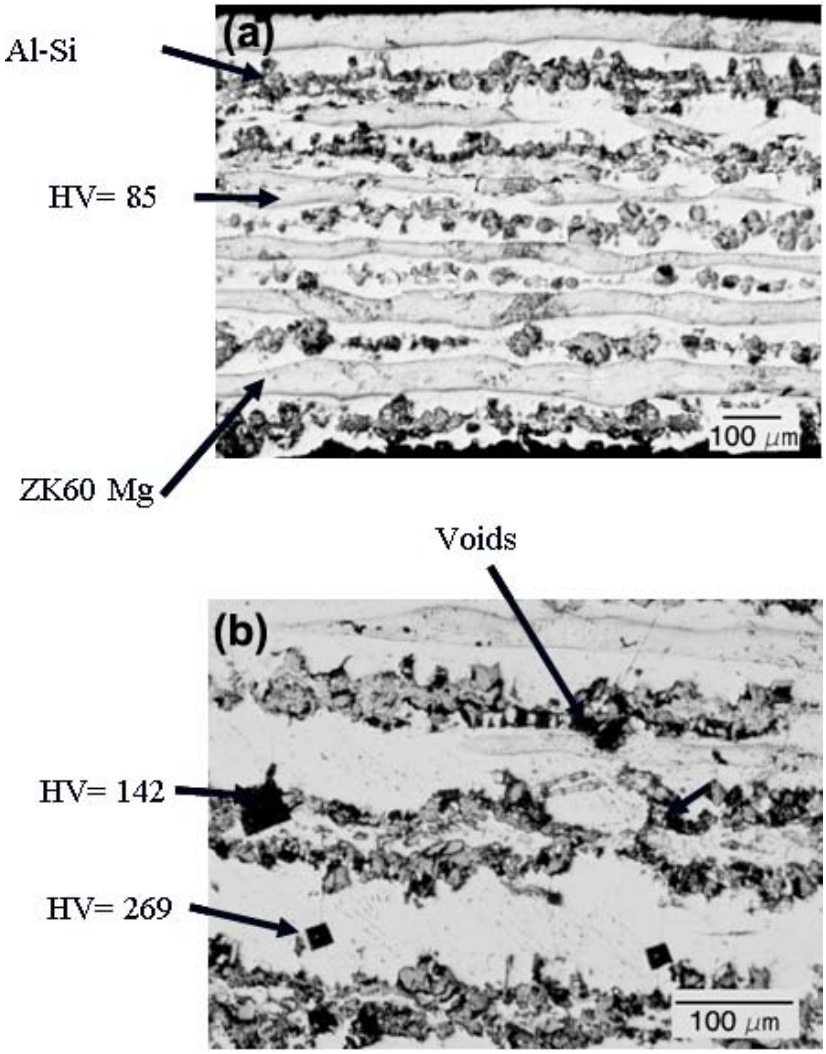

Figure 6.9 (a) Microstructure of ZK60 Mg / Al- Si laminated composite heat treated at 350^{o}C for 6 hrs. The (darker contrast) ZK60 layers have partially diffused in to the (lighter contrast) Al-Si alloy. (b) There is also some evidence suggesting formation of Mg-Si intermetallic in the vicinity of Si particles. Not much change in ZK60 layer hardness was observed while two regions of high hardness are identified. Some voids are also near interface region between different material layers.

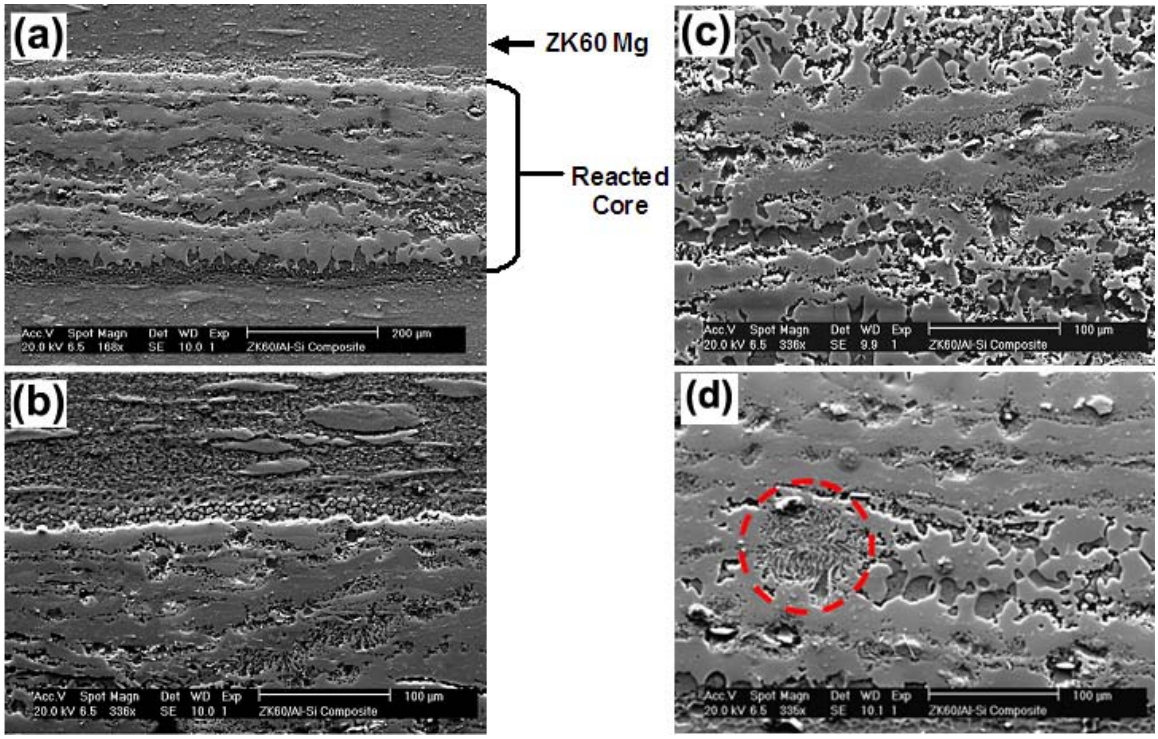

Figure 6.10 Microstructure of laminated composite after heat treatment at 450 ^{o}C for 1 hr under an applied load. The laminate was hot pressed to ~ 0.4 mm thickness at 450 ^{o}C with a true strain of $\varepsilon = 1.6$. In (a) the over all microstructure is shown, and no individual Al-Si or ZK60 Mg layers are visible after heat treatment. A reacted region between surface ZK60 layers is also identified. (b) Shows the interface between ZK60 Mg surface layer and reacted region. Fine Mg grains are observed near the interface. In (c & d) high magnification SEM pictures show several regions with distinct microstructure and appearance in the reacted core.

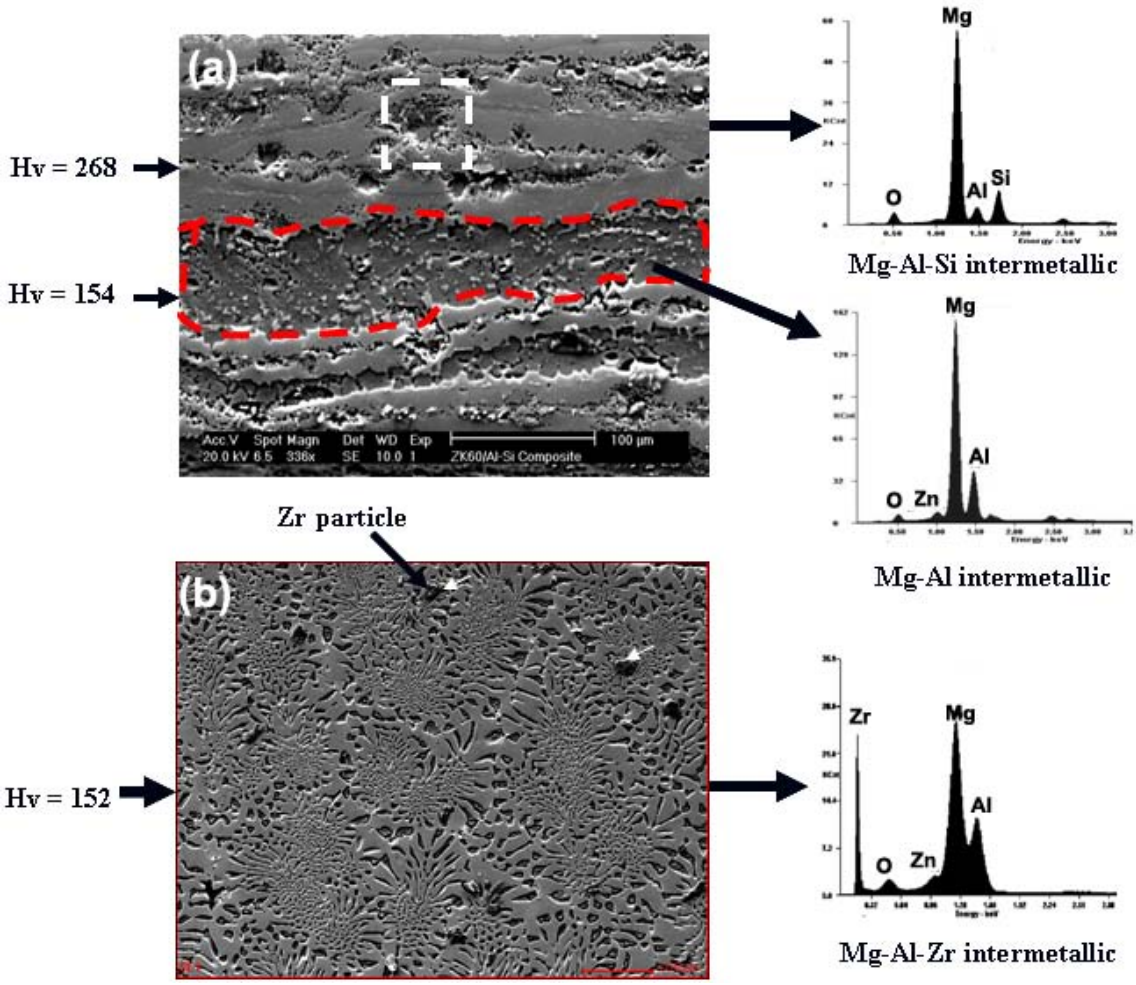

Figure 6.11 (a) & (b) represent regions of distant structure and micro-hardness in the reacted region. EDXS analysis on these selected regions done at 15 kV identified presence of different intermetallics. In (b) higher magnification shows unique microstructure corresponding to highlighted region in (a) that was observed in the reacted region. Some Zr particles were also present in the microstructure (indicated by arrows).

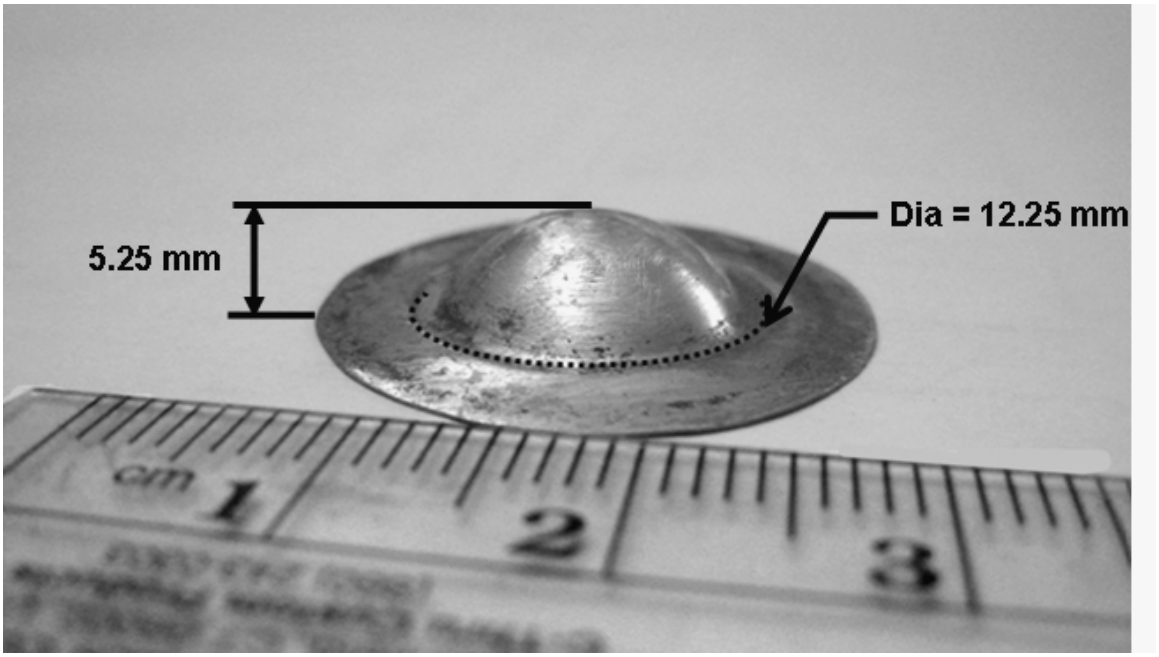

Figure 6.12 Dome height of 5.25 mm is achieved for laminated composite at pressure of 350 psi. A forming limit strain of $\varepsilon = 0.32$ was measured at the dome apex.

6.6 References

[1] A.A. Luo, *JOM*, 54 (2002), p. 42-48.

[2] B.L. Mordike and T. Ebert, *Materials Science Engineering A*, 302 (2001), p. 37-45.

[3] E. Doege and K. Droder, *Journal of Materials Processing Technology*, 115 (2001), p.14-19.

[4] T.L. Jones, S.M. Burkins, A.W. Gooiam, *Magnesium Technology*, p 81-84, 2008.

[5] B. Li, S. Joshi, K. Azevedo, and T.G. Langdon, 517(2009), P. 24-29

[6] L. Zhen, D.L. Zou, C.Y. Xu and W.Z. Shao, *Materials Science Engineering A*, 527(2010), p. 5728-5733.

[5] K. U. Kainer, Mater. Sci. Eng. A 135 (1991) 243.

[6] A. Luo, *Metall. Mater. Trans. A*, 26A (1995) 2445.

[7] T. Wada, T. Shinkawa, Y. Kojima, *J. Japan Inst. Light Metals*. 45 (1995) 510.

[9] M. Y. Zheng, and C. K. YAO, *Materials Science Engineering A* 318 (2001) 50.

[10] S. Ryu, J. Kaneko and M. Suganuma. *J. Jpn. Inst. Met.* 61 (1997), p. 1160

[11] R. Oakley, R.F. Cochrane and R. Stevens. *Key Eng. Mater.* 104–107 (1995), p. 387.

[12] D.J. Towle and C.M. Friend. *Mater. Sci. Eng.* A135 (1991), p. 153.

[13] N. Llorca, A. Bloyce and T.M. Yue. *Mater. Sci. Eng.* A135 (1991), p. 247.

[14] S.-W. Lim, T. Imai, Y. Nishida and T. Cho. *Scr. Metall. Mater.* 32 (1995), p. 1713.

[15] M. Mabuchi and K. Higashi. *Philos. Mag., A* 74 (1996), p. 887.

[16] T.G. Nieh, A.J. Schwartz and J. Wadsworth. *Mater. Sci. Eng., A* A208 (1996), p. 30.

[17] T. Imai, S.-W. Lim, D. Jiang and Y. Nishida. *Scr. Metall. Mater.* 36 (1997), p. 611.

[18] A.-B. Ma, T. Imura, M. Takagi, Y. Nishida, J.-H. Jiang, T. Imai, S.-W. Lim and J.-Q. Jiang. *Mat. Sci. Forum* 304–306 (1999), p. 279.

[19] A.-B. Ma, J.-Q. Jiang, J.-H. Jiang, Y.-S. Sun, Y. Nishida, T. Imai, P.-S. Chen, T. Imura and M. Takagi. *Mat. Sci. Forum* 304–306 (1999), p. 285.

[20] T. Imai, S.-W. Lim, D. Jiang, Y. Nishida and T. Imura. *Mat. Sci. Forum* 304–306 (1999), p. 315.

[21]. M. Mabuchi, K. Kubota and K. Higashi. *Mater. Sci. Technol.* 12 (1996), p. 35.

[22] U. Draugelates, A. Schram and C.-C. Kendenburg. In: B.L. Mordike and K.U. Kainer, Editors, *Magnesium Alloys and Their Applications*, Werkstoff-Informationsgesellschaft, Frankfurt (1998), p. 381.

[23] D.L. Yin, K.F. Zhang,W.B. Han, *Materials Science Engineering A* 392(2005), P. 320-325.

[24] G.H. Min, J.M. Lee, S.B. Kang and H.W. Kim, *Mater. Lett.* 60 (2006), pp. 3255–3259.

[25] M.T. Pérez-Prado, J.A. Del Valle and O.A. Ruano, *Scr. Mater.* 51 (2004), pp. 1093–1097.

[26] M.Y. Zhan, Y.Y. Li, W.P. Chen and W.D. Chen, *J. Mater. Sci.* 42 (2007), pp. 9256–9261.

[27] S.B. Yi, I. Schestakow and S. Zaefferer, *Mater. Sci. Eng. A* 516 (2009), pp. 58–64.

[28] Y. Takahashi, H. Inoue and K. Nishiguchi, *Acta Mater.* 41 (1993), pp. 3077–3084.

[29] N. Orhan, M. Aksoy and M. Eroglu, *Mater. Sci. Eng. A* 271 (1999), pp. 58–468.

[30] R.G. Zhang and V.L. Acoff, *Mater. Sci. Eng. A* 463 (2007), pp. 67–73.

[31] R.J. Hebert and J.H. Perepezko, *Scr. Mater.* 50 (2004), pp. 807–812.

[32] F.H. Kavarana, K.S. Ravichandran , S.S. Sahay, *Scr. Mater.* 42 (2000), pp. 947–954.

[33] K.S. Ravichandran, S.S. Sahay , J.G. Byrne, *Scr. Mater.* 35 (1996), pp. 1135–1140.

[34] S.L. Lehoczky, *J. Appl. Phys.* 49 (1978), pp. 5479–5485.

[35] J.M. Lee, B.P. Lee and S.B. Kang, *Mater. Sci. Eng. A* 406 (2005), pp. 95–101.

CHAPTER 7

SUMMARY AND RECOMMENDATIONS FOR FUTURE WORK

7.1 Summary

Grain refinement, control of precipitation and texture modification by thermomechanical processing provide a viable approach to produce high strength and high ductility Mg alloys. It also improves warm formability of Mg alloys which is imperative for their wide-spread applications.

In biaxial corrugated pressing of Mg alloys, it was found that twinning occurs during early stages of deformation processing and contributes to grain subdivision, while slip, dynamic recovery and possibly dynamic recrystallization during hot rolling or flat pressing produces a uniform fine-grain structure. Strain-rate sensitivity (m-value) of fine grained Mg is more than the coarse grain counter-parts. In case of heat treatable Mg alloys, a low temperature aging treatment of ultra-fine grained alloy further improves mechanical properties. Over-all at room-temperature the enhanced strength levels are believed to be influenced by sub-micron grain size and precipitates found in this alloy; while fracture ductility is believed to be strongly influenced by deformation texture.

In friction stir processing of Mg alloys to partial depth; it was found that composite microstructures can be created. The friction stir processed Mg alloys exhibit enhanced mechanical properties and can be hot pressed at warm-temperatures. It believed that strength and ductility of stir processed Mg alloys is highly influenced by the layered nature of microstructure, fine precipitates and textural gradient between core and surface regions.

Friction stir processing was also found to be beneficial in porosity reduction from thixomolded Mg alloys. Over-all friction stir processing parameters may be chosen to create highly formable Mg sheets.

Bending reverse bending process applied at warm temperatures is helpful in alleviating strong basal texture from hot rolled Mg sheets. Under proper processing conditions grain structure may also be refined by this approach. BRB-processed sheets maybe rolled with large thickness reductions at warm temperatures.

In deformation processing of Mg/Al laminated composite. It was established that a strong bond can be achieved between Mg and Al layers. This process offers unique in-situ precipitation potential if laminate layer chemistry is properly chosen. It was established that under dynamic conditions heat treatment of laminated composites leads to the formation of a reacted core region with very high micro-hardness.

7.2 Recommendations for future work

(1) Biaxial corrugated pressing and flattening may be employed in rolling mills using fluted and flat rolls to produce bulk quantities of ultra-fine grain Mg sheets suitable

for warm forming. However, this is not a trivial problem and must be fully investigated to establish the efficacy of such a rolling scheme. The corrugated rolling in combination with conventional flat rolling may also be applied to other metallic alloys e.g. Cu, Al or even Ti to refine grain size and improve mechanical properties.

(2) In ZK60 Mg in addition to grain size and precipitation hardening, texture had a strong influence on room-temperature mechanical properties. A modeling approach maybe necessary to fully understand the effect of texture in combination with other strengthening processes. Secondly, the effect of β precipitates on strength and ductility of ultra-fine grained Mg must be investigated by transmission electron microscopy to fully understand the orientation and morphology effect of these precipitate particles.

(3) Friction stir processing to partial depths creates composite microstructure with soft core and hard surface regions. The FSP processing is an exciting addition to severe plastic deformation techniques and its effect on other heat treatable magnesium alloys such as AZ91 and ZE41 should be explored to understand the role of precipitates on the grain refinement and strengthening of materials.

(4) Bending reverse bending is an ideal setup that can be readily applied in the process chain in most manufacturing systems. Additionally the roller tempering technology can be easily converted into heated bending reverse bending setups. In present work, we studied the fundamental effect of bending reverse bending on Mg. A more detailed and carefully designed study directed at establishing the effect of strain-rate

and applied tension may be useful to fully understand the effectiveness of this process for microstructure and texture modification.

(5) The deformation processing of laminated Mg composites offers several advantages, and can easily be applied at larger scale by using an approach similar to accumulative roll bonding. Secondly, a variety of Al alloys may be studied in combination with Mg matrix. In addition to that, stronger materials such as high strength TRIP steels can also be bonded to Mg, a rule of mixture type study may be employed to study the effectiveness of such a composite in achieving high strength and ductility.

(6) It will be very interesting to see the effect of friction stir processing on Mg/Al laminated composites. The combination of diffusion bonded laminated composites and friction stir processing may offer unique in-situ alloying which maybe investigated.